

**DESIGN, SUSPENSION AND OPTICAL CHARACTERIZATION OF  
THE BEAM SPLITTER AND OUTPUT MODE CLEANER FOR THE  
AEI 10 M PROTOTYPE**

Von der Fakultät für Mathematik und Physik  
der Gottfried Wilhelm Leibniz Universität Hannover

zur Erlangung des Grades

**Doktor der Naturwissenschaften**

Dr. rer. nat.

Genehmigte Dissertation von

**M.Sc. Philip Koch**

**2022**

Referent: Professor Karsten Danzmann  
Korreferent: Professor Kenneth A. Strain  
Korreferent: Professor Joshua R. Smith

Tag der Promotion: 12.07.2022

## Abstract

Gravitational wave detectors are highly sensitive instruments to measure gravitational waves. To increase their observation time and decrease maintenance and upgrade periods, newly developed improvements need to be tested thoroughly. The AEI 10 m prototype is a testing facility for potential upgrades to gravitational wave detectors, providing an extremely low noise environment.

The sub-SQL interferometer at the AEI 10 m prototype is a Fabry-Perot Michelson interferometer. Once set up, it will measure differential length changes between its interferometer arms limited by the standard quantum limit (SQL). This will allow techniques to surpass the SQL in gravitational wave detectors to be tested.

This thesis presents the design and implementation of various subsystems for the sub-SQL interferometer at the AEI 10 m prototype.

Aluminum gallium arsenide (AlGaAs) test mass mirror coatings promise reduced coating Brownian noise. Nonetheless, it remained to be shown that the thickness uniformity and damage threshold of AlGaAs coatings fulfill the requirements of gravitational wave detectors. Here, the thickness uniformity RMS was measured to be  $0.41 \pm 0.05$  nm, and the lower limit for the laser-induced damage threshold of the mirrors was measured to be  $64 \pm 5$  MW/cm<sup>2</sup>.

A scatter measurement device is set up to characterize optics for the AEI 10 m prototype. It provides bidirectional reflection distribution function measurements of high-quality optics. It can measure optics with a total integrated scattering of below 0.01 ppm.

The beam splitter of the sub-SQL interferometer and its triple-suspension were designed. The optical requirements of the beam splitter are defined and discussed. Its shape and a split coating are designed to reduce the power in arising ghost beams. The beam splitter's triple suspension was built, and its resulting performance was evaluated, fulfilling the set requirements.

An output mode cleaner for the sub-SQL interferometer was designed and built, including its double suspension. The design focuses on reducing optical losses while fulfilling the mode filter requirements. Its losses were measured to be  $0.1 \pm 0.4$  % while fulfilling the required mode filter performance based on an output beam profile of aLIGO.

Keywords: gravitational wave detector, AEI 10 m prototype, optical coating thickness uniformity, scattered light, seismic isolation, low-loss optical resonators, laser mode cleaner



# Contents

<b>Abstract</b>	<b>i</b>
<b>List of abbreviations</b>	<b>vii</b>
<b>1 Introduction of the AEI 10 m Prototype</b>	<b>1</b>
1.1 Gravitational wave detectors . . . . .	2
1.1.1 Gravitational waves . . . . .	2
1.1.2 A Michelson interferometer as gravitational wave detector . . . . .	3
1.2 Noise . . . . .	4
1.2.1 Quantum noise and the SQL . . . . .	6
1.2.2 Seismic noise . . . . .	8
1.2.3 Laser noise . . . . .	9
1.2.4 Thermal noise . . . . .	10
1.2.5 Residual gas noise . . . . .	11
1.2.6 Electronic noise . . . . .	11
1.3 The AEI 10 m prototype . . . . .	12
1.3.1 The vacuum system . . . . .	14
1.3.2 Seismic isolation . . . . .	14
1.3.3 The laser system . . . . .	15
1.3.4 The sub-SQL interferometer . . . . .	17
1.4 Outline . . . . .	19
<b>2 Thickness uniformity and damage threshold measurements of crystalline GaAs/AlGaAs coatings</b>	<b>21</b>
2.1 Thickness uniformity measurements of dielectric coatings . . . . .	22

2.1.1	Importance of thickness uniformity in gravitational wave detectors . . . . .	22
2.1.2	Working principle of dielectric coatings . . . . .	23
2.1.3	Working principle of an MBE chamber . . . . .	25
2.1.4	Converting reflectivity into thickness uniformity . . . . .	26
2.1.5	Measurement set-up . . . . .	29
2.2	Thickness uniformity results for a crystalline, high reflective GaAs/AlGaAs coating . . . . .	30
2.2.1	Sample parameters . . . . .	30
2.2.2	Compensation of the rear surface reflection . . . . .	32
2.2.3	Thickness uniformity results . . . . .	36
2.3	Damage threshold test for a crystalline, high reflective GaAs/AlGaAs coating . . . . .	38
2.3.1	Damage threshold test set-up . . . . .	39
2.3.2	Damage threshold results . . . . .	40
<b>3</b>	<b>Scatterometer</b>	<b>41</b>
3.1	Optical scattering . . . . .	42
3.1.1	Rayleigh scattering . . . . .	42
3.1.2	Mie scattering . . . . .	43
3.1.3	Fourier scattering . . . . .	43
3.1.4	The BRDF . . . . .	43
3.2	Measuring the BRDF . . . . .	44
3.2.1	Measurement principle . . . . .	44
3.2.2	Scatterometer set-up . . . . .	47
3.2.3	Calibration of the scatterometer . . . . .	50
3.2.4	Scatterometer results for a set of high quality optics . . . . .	52
<b>4</b>	<b>Beam splitter for the sub-SQL interferometer</b>	<b>54</b>
4.1	Beam splitter design . . . . .	55
4.1.1	Optical requirements . . . . .	55
4.1.2	Shape constraints . . . . .	62
4.2	Triple suspension design . . . . .	66

4.2.1	Suspensions as harmonic oscillators . . . . .	67
4.2.2	Degrees of freedom and cross coupling . . . . .	68
4.2.3	Suspension simulations and parameters . . . . .	70
4.2.4	Active damping and control . . . . .	71
4.2.5	Suspension design . . . . .	73
4.2.6	Measured resonance frequencies . . . . .	79
4.2.7	Evaluation of the expected performance . . . . .	80
<b>5</b>	<b>An output mode cleaner for the sub-SQL interferometer</b>	<b>85</b>
5.1	Mode filtering . . . . .	86
5.1.1	Gaussian beam . . . . .	86
5.1.2	Modes inside a cavity . . . . .	89
5.1.3	Mode cleaner . . . . .	93
5.2	Designing the OMC . . . . .	95
5.2.1	Requirements for the OMC . . . . .	95
5.2.2	Choosing FSR and RoC . . . . .	96
5.2.3	Choosing a finesse . . . . .	98
5.2.4	Choosing the AoI . . . . .	99
5.2.5	The optical layout . . . . .	101
5.3	Requirements and testing of the optical components . . . . .	104
5.3.1	Input and output mirror . . . . .	104
5.3.2	Curved mirrors . . . . .	107
5.3.3	Non-cavity components . . . . .	109
5.3.4	Pairing of components . . . . .	113
5.4	Assembly of the OMC . . . . .	113
5.4.1	Assembling the curved mirrors . . . . .	114
5.4.2	Assembling the OMC cavity . . . . .	116
5.5	OMC suspension design . . . . .	118
5.5.1	Two-stage suspension design . . . . .	119
5.6	Final OMC performance . . . . .	122
5.6.1	Measured cavity parameters . . . . .	122
5.6.2	Estimated mode filter performance . . . . .	124
5.6.3	Loss measurement . . . . .	125

<b>6 Summary and outlook</b>	<b>129</b>
<b>A Suspension blade springs</b>	<b>132</b>
A.1 Pre-bend vs flat . . . . .	132
A.2 Maraging steel vs. stainless spring steel . . . . .	133
A.3 BS suspension blade springs . . . . .	134
A.4 OMC suspension blade springs . . . . .	139
<b>B Low-loss OMC step-by-step</b>	<b>145</b>
B.1 Designing the OMC . . . . .	145
B.1.1 Cavity shape . . . . .	146
B.1.2 Quantifying the mode filter requirements . . . . .	146
B.1.3 Defining the finesse . . . . .	147
B.1.4 Defining an angle of incidence . . . . .	147
B.2 Requirements for optical components . . . . .	148
B.3 Optic characterization and preparation . . . . .	154
B.4 Assembly . . . . .	156
B.5 OMC suspension . . . . .	156
<b>Bibliography</b>	<b>158</b>
<b>Publication list</b>	<b>166</b>
<b>Collaboration publications</b>	<b>167</b>
<b>Acknowledgments</b>	<b>179</b>
<b>Curriculum vitae</b>	<b>180</b>

## List of abbreviations

<b>aLIGO</b>	advanced laser interferometer gravitational wave observatory
<b>AOM</b>	acusto-optic modulator
<b>AR</b>	anti-reflective
<b>ASD</b>	amplitude spectral density
<b>BD</b>	beam dump
<b>BRDF</b>	bidirectional reflection distribution function
<b>BS</b>	beam splitter
<b>CCD</b>	charged-coupled device
<b>CM</b>	center of mass
<b>CMS</b>	Crystalline Mirror Solutions
<b>cts</b>	counts
<b>DFB</b>	distributed feedback
<b>DOF</b>	degree of freedom
<b>EOM</b>	electro-optic modulator
<b>ETM</b>	end test mass
<b>FSR</b>	free spectral range
<b>FWHM</b>	full-width half maximum
<b>GaAs/AlGaAs</b>	gallium-arsenide / aluminum-gallium-arsenide
<b>GR</b>	General Theory of Relativity
<b>HG</b>	Hermite-Gaussian
<b>HO</b>	harmonic oscillator
<b>HOM</b>	higher-order mode
<b>HoQI</b>	homodyne quadrature interferometer
<b>HR</b>	high reflective
<b>HRXRD</b>	high-resolution x-ray diffraction measurement
<b>IBS</b>	ion-beam sputtering
<b>ISS</b>	intensity stabilization system
<b>IT</b>	input telescope
<b>ITM</b>	input test mass
<b>KAGRA</b>	Kamioka gravitational wave detector
<b>LED</b>	light-emitting diode
<b>LIDT</b>	laser-induced damage threshold
<b>LIGO</b>	Laser Interferometer Gravitational-Wave Observatory
<b>LPD</b>	linear power density
<b>LSC</b>	LIGO scientific collaboration

<b>MBE</b>	molecular beam epitaxy
<b>MI</b>	Michelson interferometer
<b>Nd:Yag</b>	neodymium-doped yttrium aluminum garnet
<b>NPRO</b>	non-planar ring oscillator
<b>OMC</b>	output mode cleaner
<b>OPL</b>	optical path length
<b>OT</b>	output telescope
<b>PBS</b>	polarizing beam splitter
<b>PD</b>	photodiode
<b>PDH</b>	Pound-Drever-Hall
<b>PMC</b>	pre-mode cleaner
<b>POM</b>	polyoxymethylene
<b>ppm</b>	parts per million
<b>PV</b>	peak to valley
<b>PZT</b>	lead zirconate titanate
<b>QPD</b>	quadrant-photodiode
<b>RC</b>	reference cavity
<b>RMS</b>	root-mean-square
<b>SAS</b>	seismic attenuation systems
<b>SPI</b>	suspension platform interferometer
<b>SQL</b>	standard-quantum-limit
<b>TEM</b>	transverse electromagnetic mode
<b>TF</b>	transfer function
<b>TIS</b>	total integrated scattering
<b>TMS</b>	transverse mode spacing
<b>UHV</b>	ultra-high vacuum

# Chapter 1

## Introduction of the AEI 10 m Prototype

---

The AEI 10 m prototype is a testing facility for new and improved gravitational wave detection techniques. Its main experiment is a sub-standard-quantum-limit (SQL) Fabry-Perot-Michelson interferometer, which is currently under construction. In this chapter, a short overview of a Michelson interferometer (MI) as gravitational wave detector will be given to motivate the set-up of the sub-SQL interferometer. As the suppression of various classical noise sources is required to measure at and below the SQL, an overview of some of the dominating noise sources is presented. Alongside the basic set-up of the AEI 10 m prototype, its subsystems and their corresponding tasks to suppress different classical noise sources are explained. This includes the vacuum system, the seismic pre-isolation and the laser system with its power and frequency stabilization. The role of the research presented in this thesis will be highlighted alongside the introduction to the AEI 10 m prototype. An outline will provide a brief summary of the upcoming chapters.

## 1.1 Gravitational wave detectors

In its purpose as a testbed for new and improved detection techniques for gravitational wave detectors, the sub-SQL interferometer of the AEI 10 m prototype will be compared to the large-scale detectors throughout this thesis. Though the sub-SQL interferometer is not designed to measure gravitational waves, the requirements of many subsystems are similar to the large-scale detectors. Further, several of the results in this thesis can be evaluated in hindsight to their performance inside a gravitational wave detector.

Gravitational wave detectors are large-scale MIs, required to measure length changes below  $10^{-18}$  m, the thousandth of a proton diameter [Abb+16b]. At the time of writing, there are five functional, interferometric gravitational wave detectors taking part in joined measurements. The two largest detectors are located in the United States of America and are called advanced laser interferometer gravitational wave observatories (aLIGO) [J A+15]. Another gravitational wave detector is the Virgo detector located in Italy [Ace+14]. GEO600 is a gravitational wave detector located in Germany [Wil+02], and the Kamioka gravitational wave detector (KAGRA) is a gravitational wave detector in Japan [Aku+20].

A short overview of gravitational waves and their interaction with a MI is presented in this section to motivate the design of a gravitational wave detector and thus the set-up and design of the sub-SQL interferometer.

### 1.1.1 Gravitational waves

Gravitational waves are changes in the curvature of spacetime caused by the acceleration of masses. In 1916 Albert Einstein published the General Theory of Relativity (GR) and predicted Gravitational waves as a solution to the Einstein field equations [Ein16]. According to the GR, each accelerated mass changes the curvature of spacetime, creating a gravitational wave (see figure 1.2). The gravitational waves propagate as transverse waves similar to electromagnetic waves. A gravitational wave travels with the speed of light and carries information of its origin encoded in its duration, amplitude, frequency and phase. By implication, when measured, these parameters can be used to gather information, such as the mass and distance of the accelerated masses.

Even after their prediction by the GR, gravitational waves were believed to either not exist or to be immeasurable due to their small effects. The first indirect measurements of gravitational waves were made in 1974. By observing a binary pulsar system, a discrepancy from the expected period evolution was discovered [HT75]. The shortened periods of each circulation could be explained by an energy loss equal to the energy of the expected gravitational wave, calculated for the binary system.

The first direct measurement was done in 2015 by the two aLIGO detectors. The detectors measured a passing gravitational wave by measuring the distortion of spacetime along the 4 km arms of the L-shaped detectors. The event, causing the distortion of spacetime in the form of gravitational waves, was the merging process of two black holes. The two black holes had a mass of 36 solar masses ( $M_{\odot}$ ) and 29  $M_{\odot}$  at a luminosity distance of 410 Mpc [Abb+16a]. While orbiting each other at a decreasing distance, the black holes accelerated and emitted gravitational waves. After traveling for 1.3 billion years, the gravitational waves caused the differential arm length of the detectors to change by  $10^{-18}$  m. This arm length change was measured as a signal, lasting for 0.2 s within the measurement frequency band of the detectors. The shape of the signal could be used to determine the mass of the merging black holes, as well as their distance and rough sky localization.

### 1.1.2 A Michelson interferometer as gravitational wave detector

To measure length changes as small as  $10^{-18}$  m, a specially designed and improved Michelson interferometer (MI) is required. Up to date, the only direct measurements of gravitational waves were made using an MI-like set-up. The MI was first developed by Albert A. Michelson in the late 19th century to measure length changes of about  $10^{-7}$  m. With the invention of the laser, the sensitivity improved drastically. In 1988, one of the first gravitational wave detector prototypes in Garching was able to measure length changes of just below  $10^{-17}$  m above 400 Hz [Sho+88]. Today, the aLIGO detectors are capable of measuring length changes of below  $10^{-19}$  m in a frequency band ranging from 30 Hz to 3 kHz [Bui+20].

A MI measures the relative length change of its interferometer arms. As shown in figure 1.1, a laser MI consists of a laser that is split into two beam paths by a

beam splitter. Each beam path represents one arm of the interferometer with a respective length of  $L_x$  and  $L_y$ . At the end of each arm, the light is reflected back by a mirror. The laser beams are recombined at the beam splitter and interfere with each other. This results in a part of the laser beam recombining towards the input beam and another recombining towards the output of the MI. They will be called input and output port. The amplitude of the laser beams in both ports depends on the phase difference between the laser light in both arms. Suppose one arm changes its length relative to the second arm, their phase difference, and thus the amplitude and power of the laser beam in the input and output port changes. This power change can be observed on a photodiode (PD).

In most cases, an incoming gravitational wave changes the relative arm length of the MI by compressing the spacetime in one arm while stretching it in the other. In figure 1.2 the distortion of spacetime and its influence on a MI can be seen. A gravitational wave traveling in the  $z$ -direction distorts the arms in the  $x$  ( $L_x$ ) and  $y$  ( $L_y$ ) directions. This effect can be seen for four different time marks ( $t_1$ - $t_4$ ), each differing by a quarter of the gravitational wave's period. For a gravitational wave traveling along the  $z$ -axis, this effect is maximal. If the orientation of the gravitational wave towards the MI changes, the induced relative arm length change will be reduced. For specific orientations, both arms are distorted by the same amount in the same direction, and no signal can be measured.

The sensitivity of a gravitational wave detector directly depends on its arm length. As the gravitational wave compresses and stretches the space along the interferometer arms, the absolute length change of the arm scales with its length. The arm length, as seen by the laser beam traveling inside the arms, can be increased by either folding the arm (used in GEO600) or using a Fabry-Perot-interferometer inside the arms (used in aLIGO). Both methods increase the travel distance of the light along the interferometer arm.

## 1.2 Noise

To be able to measure length changes below  $10^{-18}$  m, gravitational wave detectors need to be provided with complex subsystems, reducing noise arising from a variety of sources. Today, gravitational detectors are even partially limited by quantum

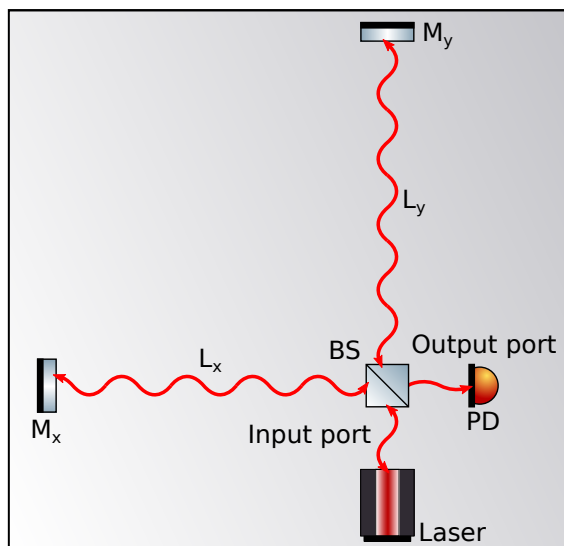


Figure 1.1: Schematic set-up of a laser MI. Laser beams are visualized as the amplitude of their electromagnetic fields. A laser beam is split into two arms with a respective length of  $L_x$  and  $L_y$ . The laser beam is reflected back at the end of each arm by the mirrors  $M_x$  and  $M_y$  and recombined at the beam splitter (BS). There, it splits into the input and output port. The laser power of the beam at the output port is measured with a photodiode (PD). Its amplitude is dependent on the phase difference of the laser beams in both arms.

noise, described by the stochastic distribution of photons inside a laser beam [CM04]. The major part of different noise sources is as relevant for a prototype system as for the large-scale detectors. Most of them are slightly less stringent due to the lower design sensitivity. Others, such as the noise of the PDs, can be compared to the requirements set for gravitational wave detectors.

In this thesis, the term noise is used to describe any unwanted gravitational wave detector output, potentially covering the signal of gravitational waves. In different areas of physics and engineering, the term noise carries different meanings and definitions. Often it is related to a pure statistical background. Here, noise is defined as the output of the gravitational wave detector in the absence of a gravitational wave. This measured noise will be called total noise and is composed of different noise contributors. If all dominant and near dominant noise sources, as well as their coupling mechanisms into the detector output, are known, their projected sum equals the measured total noise.

To compare the various frequency-dependent noise sources, their projected

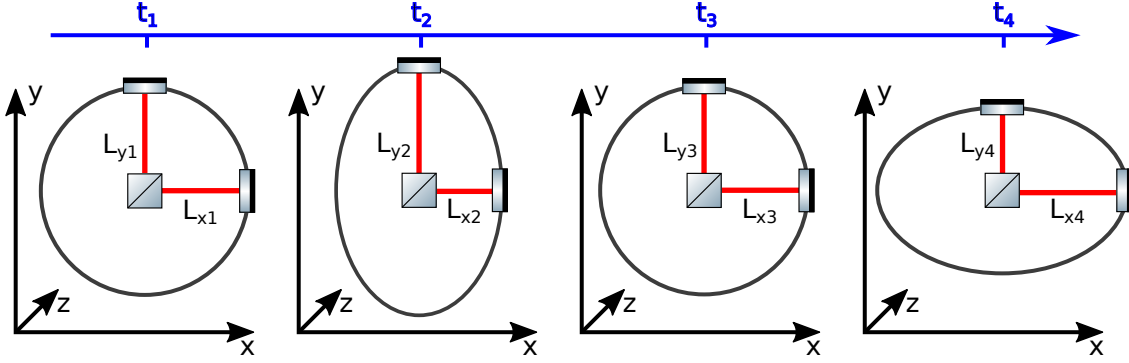


Figure 1.2: Gravitational waves traveling in  $z$  direction distort spacetime in  $x$  and  $y$  direction orthogonally to their propagation. Their distorting effect on a MI at four different times ( $t_1$ - $t_4$ ) is shown. Each time differs by a quarter of the period of the gravitational wave.

amplitude spectral density (ASD) is used. The ASD of each potential noise source is either measured or simulated at the source. Transfer functions are used to project the noise to the output of the detector. E.g. for seismic noise, the ground displacement couples to the test mass displacement via the various seismic isolation systems. This results in a differential arm length change and hence a change of laser power at the output of the interferometer. As the detector output is a photodiode signal, the unit of its ASD is  $V/\sqrt{Hz}$ . This signal is usually converted to the corresponding arm length change in  $m/\sqrt{Hz}$  or to strain/ $\sqrt{Hz}$  for comparability of the different gravitational wave detectors. Strain is the distortion per unit length resulting in the unit  $m/m$ .

This section will present an overview of some of the most dominating noise sources for gravitational wave detectors. All these noise sources need to be addressed as well with the sub-SQL interferometer.

### 1.2.1 Quantum noise and the SQL

Quantum noise is one of the noise sources dominating the noise spectrum of gravitational wave detectors over a major part of their detection band. The quantum noise inside a gravitational wave detector is composed of two different parts, both originating from the same mechanism. This mechanism is the random distribution of photons inside a laser beam, leading to phase and amplitude fluctuations. The

## CHAPTER 1. INTRODUCTION OF THE AEI 10 M PROTOTYPE

phase fluctuations couple into the output of the detector by relative phase changes of the recombining beams and are called shot noise. The amplitude fluctuations apply a varying radiation pressure force on the suspended mirrors, leading to length changes of the interferometer arms. They are called quantum radiation pressure noise.

In a Fabry-Perot-MI set-up, the quantum radiation pressure noise for a given wavelength  $\lambda$  is dependent on the finesse ( $F$ ) of the arm cavities, which is a measure of their round-trip loss, the mass of the suspended mirrors ( $M$ ) and the input power at the beam splitter ( $P_{BS}$ ). It has a  $1/f^2$  frequency dependence and thus dominates quantum noise at low frequencies. The amplitude spectral density of the quantum radiation pressure noise ( $ASD_{QRPN}$ ) is the square root of the power spectral density ( $S_{QRPN}$ ), which is calculated in [Ace+20].  $ASD_{QRPN}$  is in units of  $\text{m}/\sqrt{\text{Hz}}$  and given by

$$ASD_{QRPN} = \sqrt{S_{QRPN}} = \frac{4F}{Mf^2} \cdot \sqrt{\frac{\hbar P_{BS} \cdot g(f)}{\pi^5 \lambda c}}, \quad (1.1)$$

where  $c$  is the speed of light and  $g(f)$  is the frequency response of the arm cavity. The function  $g(f) = [1 + (f/f_p)]^{-1}$  is flat until its pole frequency  $f_p$ . Usually, the pole frequency is well above the frequency band, where the quantum radiation pressure noise is dominating. The quantum radiation pressure noise can be seen as a white and thus frequency-independent noise of photon number fluctuations, hitting a suspended mirror with a corresponding force. The transfer function from a force applied to the lowest stage of the suspension to the movement of the suspended mass leads to a  $1/f^2$  dependent slope above the suspension resonances. Thus, quantum radiation pressure noise shows a slope of  $1/f^2$  in most considerations.

The shot noise in the same set-up depends on the finesse, the laser power at the beam splitter, and the frequency response of the arm cavity. It is a white noise until the interferometer's pole frequency and is the dominant contribution to quantum noise at higher frequencies. The amplitude spectral density  $ASD_{SN}$  in units of  $\text{m}/\sqrt{\text{Hz}}$  can be calculated as the square root of its power spectral density  $S_{SN}$  as given in [Ace+20].

$$ASD_{SN} = \sqrt{S_{SN}} = \frac{1}{F} \cdot \sqrt{\frac{\pi \hbar \lambda c}{P_{BS} \cdot g(f)}} \quad (1.2)$$

The standard quantum limit (SQL) is a term used for the minimal quantum noise a detector can nominally achieve at any given frequency [Heu18]. It is located at the crossover of the quantum radiation pressure noise and the shot noise. The quantum radiation pressure noise is proportional to  $\sqrt{P_{BS}}$  (see equation 1.1), while the shot noise is inversely proportional to  $\sqrt{P_{BS}}$  (see equation 1.2). This allows the crossover frequency to be shifted by changing  $P_{BS}$ . Up to date, there are several measurement schemes to even surpass the SQL, of which some are being implemented in current and future gravitational wave detectors. An overview and explanation of some of these methods can be found in [DK12].

Often it is differentiated between quantum and classical noise. While quantum noise is well described by quantum radiation pressure noise and shot noise, classical noise summarizes a variety of other noise sources. Some of them are presented in the following subsections.

### 1.2.2 Seismic noise

Seismic noise can be defined as the movement of the ground. The ground is by no means motionless. At different frequencies, environmental as well as anthropogenic effects excite seismic waves inside the ground traveling through its surface. At low frequencies around 0.1 Hz, for example, ocean waves actuate the ground surface creating the micro-seismic peaks. Around 1 Hz and above, anthropogenic noise sources such as moving people, cars and industry partly dominate the seismic noise.

Seismic noise is the dominant noise source at low frequencies, limiting the gravitational wave detector's measurement band at the lower end. Seismic noise directly changes the mirror position and thus the detector's arm length. The arm length change is detected at the output of the detector. To measure gravitational waves, seismic noise has to be suppressed by a factor of  $10^9$  to  $10^{10}$ . This is done using multistage suspensions, where each stage reduces the seismic actuating onto the mirrors by  $1/f^2$ . These multistage suspensions need to be installed for most core

optics of a gravitational wave detector. This thesis includes the design and set-up of a triple suspension for the main beam splitter of the sub-SQL interferometer (see chapter 4.2) and a double suspension for the output mode cleaner (see chapter 5.5).

Additional pre-isolation stages, including active damping, are used to reduce seismic at even lower frequencies. The suspensions can be directly mounted onto these pre-isolation stages. These stages can include passive stages, such as inverted pendulums and geometric anti-spring filters. Active damping refers to the measurement of seismic motion, which is fed back to position actuators to actively suppress the motion.

### 1.2.3 Laser noise

The laser is one of the core components of a gravitational wave detector. Its light is used to measure gravitational waves by tiny phase changes after traveling along two different arms (see chapter 1.1.2). There are two different noise sources related to the laser; the laser frequency noise and the laser amplitude noise.

In most calculations, the laser wavelength or frequency is given as a constant factor. In truth, the laser wavelength and thus frequency fluctuate, which is called laser frequency noise. The laser frequency noise originates, e.g., from length fluctuations of the laser resonator. The laser frequency noise changes the phase condition inside the detector arms as well as the resonance conditions and thus amplitude inside the arm cavities. If both detector arms have the exact same length and arm cavity properties, the resulting amplitude noise after the recombination of the beams cancels out. For this reason, the arm lengths of a gravitational wave detector are kept as similar as possible. Only a small offset of the "Schnupp asymmetry" is applied for control reasons [Wei02]. Further, a DC offset is applied, offsetting one arm by a part of a wavelength to increase the response of the gravitational wave detector to a differential arm length change. This and imperfections of the detector's arm length and arm cavity properties require active suppression of the laser frequency noise. The suppression of the laser frequency noise is usually implemented via a feedback loop measuring the laser frequency and stabilizing it using laser frequency actuators [Dre+83].

The laser amplitude noise is the fluctuating number of photons inside the laser

beam. It originates mostly from the varying pump power and spatial properties, as well as the properties of the laser crystal [Heu+06]. Similar to the quantum radiation pressure noise (see chapter 1.2.1), the laser amplitude noise leads to a force-noise onto the mirrors and thus causes the arm length to change. But unlike the quantum fluctuations leading to quantum radiation pressure noise, the amplitude fluctuations are split equally at the beam splitter. This leads to an equal arm length change in both arms and a canceled amplitude noise at the detector output. Any asymmetry in the arms, such as a difference in the mirror mass and cavity finesse or imperfection of the beam splitter's 50/50 splitting ratio, can offset this balance. The DC offset, as mentioned above, is kept as small as possible to reduce the imbalance of both arms. The asymmetries lead to the necessity of a power stabilization system. The power stabilization system is a feedback loop measuring the laser power and actuating at laser power actuators [Wil+08].

#### 1.2.4 Thermal noise

Thermal noise summarizes several thermal-based effects leading to a noise at the detector output. Here, the focus is on noise directly influencing the mirrors of the gravitational wave detector. These can be divided into temperature fluctuations changing the material properties of a mirror and the Brownian motion.

Thermo-elastic and thermo-refractive noise originates from the change of material properties at changing temperatures. Here, a mirror with a dielectric coating is considered. The dielectric coating consists of multiple layers with alternating refractive indices (see chapter 2.1.2). Depending on its thermal expansion coefficient, a material changes its size for varying temperatures. Thermal fluctuations lead to thickness fluctuations of the mirror and, thus, a length change of the arm of a gravitational wave detector. This noise source is called thermo-elastic noise and is dependent on the thickness of the expanding object. Another important optical property is the refractive index. As the refractive index changes with temperature, temperature fluctuations cause refractive index and thus reflectivity fluctuations of the individual mirrors. The reflectivity fluctuations lead to a varying laser amplitude and phase in each detector arm, causing the amplitude of the recombined beam to fluctuate. This is called thermo-refractive noise. Thermo-elastic noise of the coating

combined with thermo-refractive noise is often referred to as thermo-optic noise.

Coating Brownian noise is a limiting noise source for future gravitational wave detectors [Ste18]. The molecules inside the coating surface randomly fluctuate with increasing temperature, as described by the Brownian motion. These position fluctuations of the molecules lead to a position fluctuation of the mirror surface and thus an arm length change of the detector. A similar process can be observed in the mirror substrate and is called substrate Brownian noise. To reduce coating Brownian noise, coating materials with a lower noise can be used. One of the set goals for the sub-SQL interferometer, as well as partly for this thesis, is to investigate which of the stringent requirements of gravitational wave detectors can be fulfilled with crystalline aluminum gallium arsenide (AlGaAs) coatings.

Another Brownian noise is the thermal suspension noise. Here, fluctuating molecules inside the suspension wire lead to a fluctuating mirror position, which again leads to an arm length change of the detector. The different noise sources depending on Brownian motion can be reduced by cooling [Som12] or decreasing the mechanical loss of the respective components [Ste18].

### 1.2.5 Residual gas noise

All detectors are placed inside vacuum systems to reduce the influence of gas-molecule or density fluctuations on the gravitational wave detector. Gas density fluctuations cause the refractive index inside the detector arms to change. This changes the optical path length and is equivalent to an arm length change of the detector. To sufficiently reduce these fluctuations, an ultra-high vacuum (UHV) is required. Below a certain pressure threshold, gas damping noise dominates the noise caused by gas molecules. Gas damping noise originates from single gas molecules hitting the mirror, causing position fluctuations and an arm length change of the detector.

### 1.2.6 Electronic noise

Electronic actuators and sensors suffer from electronic noise caused by their individual electronic components. A high focus is on the dark noise of the photodiodes used to detect the output power of the gravitational wave detector. A fluctuation of

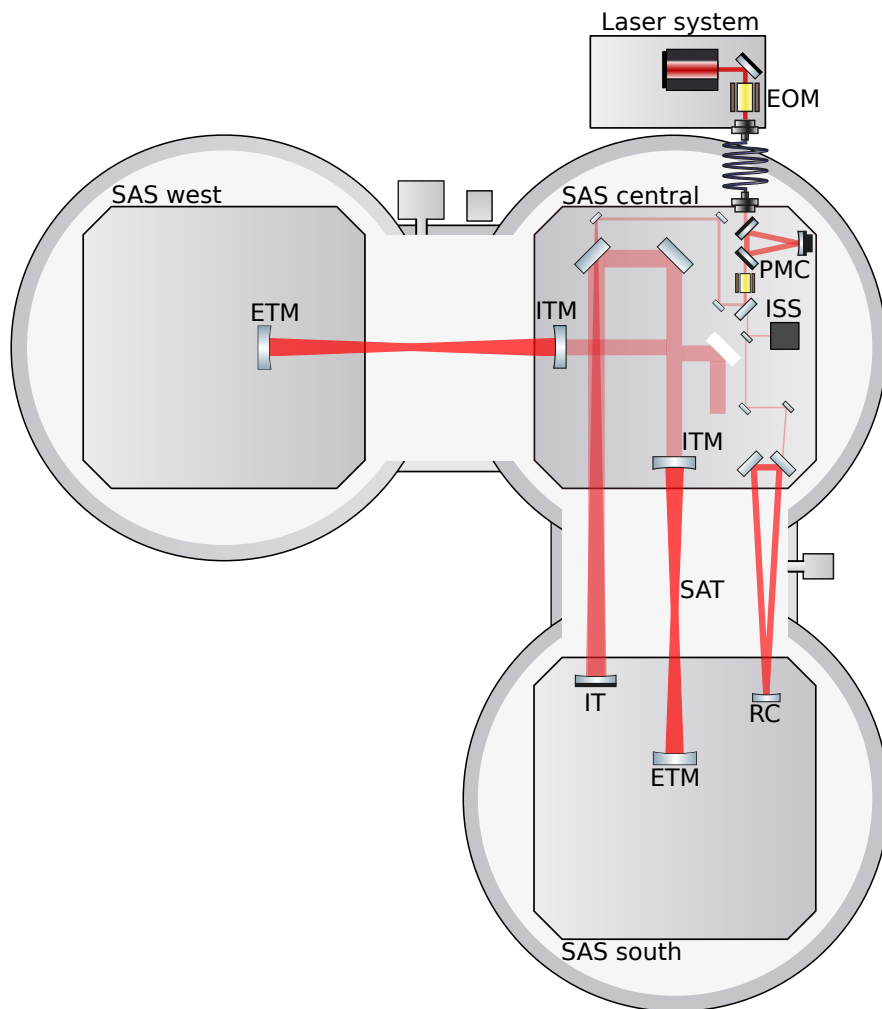
the sensed laser power directly converts to noise in the detection path. Usually, the dark noise is kept well below the shot-noise limit of the detector. The sensor noise of the seismic sensors attached to the suspensions is another electronic noise relevant for this thesis. As their signal is fed back to motion actuators, the noise of both the sensors and actuators might cause a motion of the suspended mass, changing the arm length.

### 1.3 The AEI 10 m prototype

The AEI 10 m prototype is a small-scale prototype of a gravitational wave detector. As can be seen in figure 1.3 the AEI 10 m prototype contains a MI with arm cavities inside a vacuum system. Starting at the upper right, a laser system produces a laser power of up to 35 W at a wavelength of 1064 nm. The laser beam is sent through an acousto-optic modulator (AOM) and an electro-optic modulator (EOM), serving as power and frequency actuators, respectively. A polarization-maintaining, large mode area, photonic crystal fibre [Kni+98] is used to steer the laser beam into the vacuum chamber. Inside the vacuum chamber, the laser mode is filtered by a pre-mode cleaner (PMC) and sent through another EOM to imprint phase modulation sidebands onto the laser beam. Afterwards, the beam path is split. One part leads to the intensity stabilization system (ISS) and to the frequency reference cavity (RC), serving as a power and frequency sensor (see 1.3.3). The main path leads towards the MI through an input telescope (IT). The beam splitter (BS), whose design is part of this thesis (see chapter 4), splits the laser beam towards the west and south arm. Each arm is roughly 11.7 m long and includes a Fabry-Perot cavity with an input test mass (ITM) and an end test mass (ETM). After recombining at the BS, the laser beam is sent through an output telescope (OT) into an output mode cleaner (OMC), whose design and assembly are presented in chapter 5. The laser beam is then detected by a photodiode (PD). All the listed components inside the vacuum system are placed onto one of three seismic attenuation systems (SAS). The three SAS are named after their corresponding position with *west*, *central* and *south*.

The main goal of the AEI 10 m prototype is to measure the SQL and apply techniques to surpass it. As a prototype, its purpose is not to measure gravitational

CHAPTER 1. INTRODUCTION OF THE AEI 10 M PROTOTYPE



Additionally, a small mass of the mirrors (test masses) will increase the SQL, as can be seen in chapter 1.2.1. This enables the AEI 10 m prototype to measure the SQL, being solely quantum noise limited from 20 Hz to 1 kHz. As current and future upgrades of the gravitational wave detectors are expected to be limited by quantum noise over a broad area of their measurement band, the AEI 10 m prototype will provide a testbed for techniques to surpass the quantum noise.

### 1.3.1 The vacuum system

To avoid air fluctuations and residual gas noise (see chapter 1.2.5), the interferometer is placed inside a vacuum system. It consists of three tanks connected by tubes. Each tank houses one of the three SAS tables (see section 1.3.2). A screw pump is used to prepare the vacuum system for operating the two turbopumps. Using the turbopumps, a pressure of below  $3 \cdot 10^{-7}$  mbar can be reached within a month. The total pressure is dominated by water molecules evaporating from a residual monolayer on all surfaces inside the vacuum system.

### 1.3.2 Seismic isolation

To sufficiently suppress seismic noise (see chapter 1.2.2), several active and passive attenuation stages had to be implemented. At low frequencies, the SAS provides passive damping combined with active feedback with signals coming from accelerometers and the suspension platform interferometer (SPI). At higher frequencies, the multistage suspensions of the mirrors passively attenuate seismic noise, using sensors to actively damp their internal resonances.

#### The seismic attenuation system

The SAS is a seismically isolated optical table specifically designed and built for the AEI 10 m Prototype [Wan+12]. Inverted pendulums provide passive isolation in the horizontal and geometric anti-spring filters in the vertical degrees of freedom. Accelerometers and geophones [Ber+06; Kir22] inside the optical table measure the inertial table motion. This motion is suppressed by coil-magnet actuators using a feedback loop. The DC position of the optical tables can be aligned using stepper motors connecting ground and SAS via blade springs.

### The suspended platform interferometer

The SPI is a set of heterodyne Mach-Zehnder interferometers measuring the differential motion in between the three SAS [Dah+10]. One of these Mach-Zehnder interferometers consists of one arm where a beam is sent from the central SAS to the south SAS and is reflected back to the central SAS. It recombines with the reference arm of the interferometer, which remains on the central SAS and is built on an ultra-low-expansion glass plate for high low-frequency stability. The resulting heterodyne signal is read out with a phasemeter and is fed back to the south SAS to keep the distance fixed. A second interferometer is implemented between the central and the west SAS. The SPI attenuates seismic noise at frequencies below 2 Hz by reducing the differential table motion.

### Multistage suspensions

Multistage suspensions are used to suppress seismic noise by an additional seven orders of magnitude. As explained on the beam splitter's triple suspension design in chapter 4.2, each suspension stage provides a frequency-dependent seismic noise reduction of  $1/f^2$  above their resonance frequency. This noise reduction can be stacked by attaching additional suspension stages to the first one. The multistage suspensions used for the MI of the AEI 10 m prototype are triple suspensions, suppressing seismic noise by  $1/f^6$  above the resonance frequencies in the horizontal degrees of freedom. The resonance frequencies vary between 0,7 Hz and 3.4 Hz in their motion along the respective interferometer arms for the different stages. Additionally, optics like the MI's beam splitter and optics of the reference cavity (see chapter 1.3.3) are suspended with triple suspensions. Different steering mirrors are suspended by single, double or triple suspensions, depending on their position and task. The OMC is suspended by a double suspension, whose design can be seen in section 5.5).

### 1.3.3 The laser system

The main laser system of the AEI 10 m prototype has an output power of 35 W at a wavelength of 1064 nm. It is the same design used in enhanced LIGO, which was upgraded during the aLIGO upgrade. A non-planar ring oscillator (NPRO) with a neodymium-doped yttrium aluminum garnet (Nd:YAG) crystal provides a laser

## CHAPTER 1. INTRODUCTION OF THE AEI 10 M PROTOTYPE

power of 2 W. The laser light is then amplified to 35 W by a four-head Nd:YAG amplifier [Fre+07]. The laser system provides a low power and frequency noise, which has to be suppressed further by a laser frequency stabilization system and a power stabilization system.

### **Laser frequency stabilization**

The laser frequency stabilization is a feedback loop using a length reference as a measure for the laser frequency. As the laser frequency is at about 282 THz, there is no sensor fast enough to measure the frequency directly. Instead, a frequency reference can be used, and the frequency difference between the reference and the laser can be measured. At the AEI 10 m prototype, a length reference in the form of an optical cavity is used. The Pound-Drever-Hall (PDH) locking scheme [Dre+83] is used to lock the laser frequency to the cavity length. Here, the laser frequency is controlled by temperature actuation at low frequencies, by lead zirconate titanate (PZT) actuators at mid-frequencies and an EOM at high frequencies. These three actuation stages are used to tune the laser frequency to be resonant inside the cavity. That way, the laser frequency noise can be reduced to the length noise of the cavity. To reduce the length noise of the reference cavity (RC), triple suspensions are used. The length noise requirements of the RC are similar to the length noise requirements of the MI arm cavities. As a result, the laser frequency noise is strongly reduced at frequencies above the suspension resonances.

### **Laser power stabilization**

The laser power is stabilized by utilizing the intensity stabilization system (ISS). The ISS consists of two PD arrays, each containing four PDs [JOW17]. Thus, a total laser power of 150 mW can be distributed amongst the four PDs of each array. One PD array measures the laser power to be fed back towards an AOM as a power actuator. The second PD array can be used as an out of loop sensor, providing a measurement of the resulting power noise. The ISS is designed to be shot noise limited, thus suppressing the laser power noise to the shot noise level at 150 mW of laser power.

### Mode cleaning

The intensity profile of a laser beam can be expressed by a superposition of Hermite-Gaussian (HG) modes. While the input laser beam mainly consists of the zeroth-order HG mode, some higher-order modes (HOM) with varying amplitude can be present. Further, HOMs can arise within the MI. They arise, e.g., from the laser system, mismatching lens systems or misaligned cavities. In the MI, HOMs can show different interference conditions during the recombination at the beam splitter. Thus, their coupling strength and amplitude towards the output signal of the MI can strongly vary and even surpass the zeroth-order HG mode. This needs to be avoided, as the zeroth-order HG is carrying the desired differential arm length signal of the MI.

HOMs can be filtered using specially designed filter cavities. The pre-mode cleaner (PMC) and the output mode cleaner (OMC) are such filter cavities designed to only fit the zeroth-order HG mode. While the zeroth order mode will be transmitted, the HOMs will be rejected and thus reflected by the cavity. A more detailed explanation of mode filter cavities and their design can be found in chapter 5.1. The design and set-up of the OMC for the sub-SQL interferometer is part of this thesis.

### 1.3.4 The sub-SQL interferometer

The sub-SQL interferometer is the main experiment of the AEI 10 m prototype. It is a gravitational wave detector-like MI, designed to operate with a displacement noise of below  $10^{-18}$  m/ $\sqrt{Hz}$  above 20 Hz. The sub-systems discussed in the previous section were all designed to suppress the noise in the sub-SQL interferometer.

The sub-SQL interferometer can be seen in figure 1.3. It starts behind the laser preparation belonging to the AEI 10 m prototype's infrastructure. An input telescope, consisting of a set of lenses and a curved mirror, mode-matches the laser beam to the arm cavities of the MI. It also changes the beam height, as the core optics are placed on a different height level compared to the other optical systems inside the AEI 10 m prototype. Behind the input telescope, the light is steered and aligned to the MI by two suspended steering mirrors. It is then split by a triple suspended beam splitter into the two interferometer arms. Each arm consists of an input mirror and an end mirror, forming the arm cavities. These core optics

## CHAPTER 1. INTRODUCTION OF THE AEI 10 M PROTOTYPE

are triple suspended and have a mass of 100 g. The majority of the laser power exits the cavities towards the beam splitter, where it is recombined and split into the input and output port. The laser beam of the output port is steered towards and sent through an output telescope. The output telescope consists of a curved mirror followed by a pair of lenses. It mode-matches the laser beam to the OMC, which cleans the beam profile and separates the phase modulation sidebands. The phase modulation sidebands are produced by the EOM after the PMC to control the cavities. Afterwards, the residual laser light is detected with a pair of photodiodes. This thesis will focus on the design and set-up of the triple suspended beam splitter and the OMC.

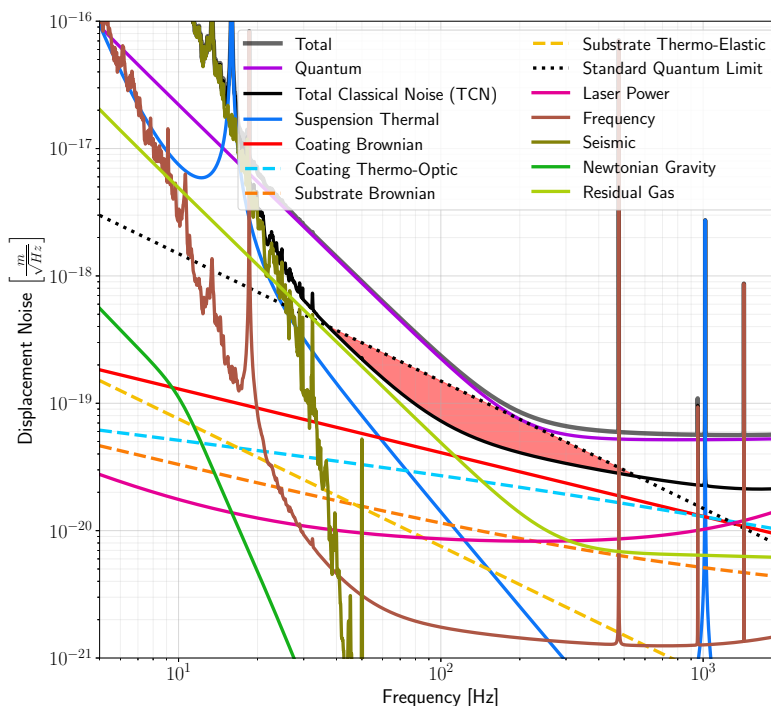


Figure 1.4: Design noise budget of the sub-SQL interferometer of the AEI 10 m prototype. Amplitude spectral density of classical and quantum noise is shown as displacement noise for the sub-SQL interferometer. The red area indicates where the classical noise is below the SQL. Simulation and graphic design made by M. Carlassara in GWINC.

## Design noise budget

The design noise budget for the sub-SQL interferometer of the AEI 10 m prototype is shown in figure 1.4. It compares the ASD of the different noise contributors listed in chapter 1.2. The noise sources are projected to the interferometer output signal and displayed as mirror displacement in units of  $\text{m}/\sqrt{\text{Hz}}$ . For frequencies between 40 Hz and 600 Hz, the combined classical noise (black line) is below the SQL belonging to the respective frequency. The quantum noise is shown for a laser input power of 5 W. The red area indicates where techniques to surpass the SQL could be implemented and evaluated, as the classical noise is below the SQL.

## 1.4 Outline

This thesis covers a range of topics, all directly related to the set-up of the sub-SQL interferometer.

In chapter 2, properties of AlGaAs coatings, as planned for the cavity mirrors of the sub-SQL interferometer, are investigated. In section 2.1, the importance of thickness uniformity of core optics in gravitational wave detectors will be discussed. An overview of the working principle of dielectric coatings is given to explain a method to accurately measure a coating's thickness uniformity. Further, crystalline coatings made from aluminum gallium arsenide (AlGaAs) are presented in section 2.2, and their thickness uniformity will be evaluated and compared to state of the art non-crystalline coatings. Additionally, a measurement of a lower limit for the laser-induced damage threshold of high reflective AlGaAs is implemented in section 2.3.

Chapter 3 shows the set-up of a scatter measurement device to measure the bidirectional reflection distribution function (BRDF). The BRDF can be used to evaluate the scatter behavior of optics and will be used for scattering measurements in the later chapters.

The beam splitter for the sub-SQL interferometer is presented in chapter 4. The first section 4.1 will provide an overview of the design of the beam splitter optic. This includes the consideration of ghost beams alongside the design of the coating and the shaping of the substrate. Section 4.2 includes the design and set-up of a triple suspension for the previously designed beam splitter. It highlights the stability

## CHAPTER 1. INTRODUCTION OF THE AEI 10 M PROTOTYPE

criteria and active control of the multistage suspension.

The chapter 5 provides an overview of the design and assembly of an OMC for the sub-SQL interferometer. Starting with a general overview of mode filter cavities in section 5.1, this is followed in section 5.2 by the design process for a low loss OMC. Section 5.3 provides scattering and reflectivity measurements of the acquired optical components for the OMC. The following assembly of specially paired optics is described in section 5.4. A two-stage suspension is designed for the OMC in section 5.5. The results of the low loss OMC are presented in section 5.6, including an evaluation of the mode filter performance and the total loss of the OMC.

## Chapter 2

# Thickness uniformity and damage threshold measurements of crystalline GaAs/AlGaAs coatings

---

This chapter describes a method to measure the thickness uniformity of dielectric coatings to an accuracy of below 0.05 nm root-mean-square (RMS). The results of a thickness uniformity measurement of a crystalline, high reflective Aluminum-Gallium-Arsenide (AlGaAs) coating are presented alongside the measurement method. Crystalline AlGaAs coatings will be used within the AEI 10 m prototype in the near future to decrease the coating thermal noise. Further, the chapter presents the results of a measurement, indicating a lower limit for the laser-induced damage threshold (LIDT) of AlGaAs coatings. These results also can be seen in the published paper "Thickness uniformity measurements and damage threshold tests of large-area GaAs/AlGaAs crystalline coatings for precision interferometry" [Koc+19].

## 2.1 Thickness uniformity measurements of dielectric coatings

The surface roughness and surface uniformity parameters are often used to describe the quality of an optical surface. Both describe the deviation between the actual and the design surface, normal to its optical surface. The difference between these two is their spatial wavelength distribution. The definition may change depending on the wavelength of the used electromagnetic wave, as well as the experimental set-up. The surface roughness is responsible for large-angle scattering [Sch+11]. Its spatial wavelength ranges from the laser wavelength up to one millimeter, resulting in scattering angles of well below 1 deg up to 90 deg. A measurement set-up for surface roughness is described in chapter 3. Surface uniformity causes small-angle scattering. Its spatial wavelength ranges from a millimeter to well above the size of the optical surface.

The surface uniformity of a mirror depends on both the surface uniformity of the substrate and the thickness uniformity of the coating. While the surface uniformity of the substrate is specified for the polishing process of the substrate, the thickness uniformity of the coating depends on the growing or deposition process inside a molecular beam epitaxy (MBE) chamber [Art02] or an ion-beam sputtering (IBS) chamber [SGR83].

In this section, the thickness uniformity of a GaAs/AlGaAs coating will be derived from a reflectivity measurement. For this purpose, it will be assumed that the growing process of the individual coating layers stays the same during the full coating run. This assumption is crucial for the measurement, as it drastically decreases the parameter space. It can be derived from the working principle of an MBE chamber (see 2.1.3), which was used to grow the coating.

### 2.1.1 Importance of thickness uniformity in gravitational wave detectors

Surface roughness and large-angle scattering lead to optical losses and stray light inside a gravitational wave detector. The surface uniformity and thus thickness uniformity of the coating leads to scattering into higher-order modes (HOM). The scattering angle of an incoming laser beam is dependent on the spatial wavelength of

## CHAPTER 2. THICKNESS UNIFORMITY AND DAMAGE THRESHOLD MEASUREMENTS OF CRYSTALLINE GAAS/ALGAAS COATINGS

the mirror surface [Har12]. The cavity mirrors of the inner Michelson interferometer of a gravitational wave detector are the optics with the most stringent requirements. If the light is scattered from one of these mirrors towards the opposite cavity mirror, it depends on the scatter angle and whether the light remains inside the cavity. Above a certain scatter angle, the light will exit the cavity by bypassing the mirror and is called stray light. Stray light is counted as a loss but can still reenter the cavity or detection path of the gravitational wave detector after being reflected off other components or the walls of the vacuum system, causing scatter noise [OFW12]. If the scattering angle is small enough for the light to remain inside the cavity, it will distort the Gaussian beam profile and thus imprint HOMs. These HOMs can couple into the gravitational wave detector output and cause increased shot noise on the photodiodes. They need to be filtered out by the output mode cleaner (OMC) at the end of the detection path.

For the Advanced LIGO (aLIGO) detectors, the required surface uniformity of the inner Michelson mirrors is set to below 0.3 nm RMS. The surface uniformity of the substrates was measured to 0.08-0.23 nm RMS [BYZ17; J A+15]. This results in a required thickness uniformity of the coatings of about 0.19-0.29 nm RMS. Surface errors, which can be compensated by aligning the mirrors in degrees of freedom, such as piston, pitch, yaw or a spherical offset, can be neglected in the determination of the thickness uniformity.

### 2.1.2 Working principle of dielectric coatings

Dielectric coatings are used to achieve high reflective (HR) coatings with "in theory" arbitrary reflectivity values for a defined wavelength. Gold or silver-coated optics reach reflectivities of around 95 % for wavelengths above 600 nm up to several micrometers [Tho22b]. Dielectric coatings provide higher reflectivities combined with lower losses and an accessible transmitted beam. They consist of two different materials with varying refractive indices, where one set of two alternating material layers is referred to as a bilayer. In between each of these two material layers, the boundary will reflect a portion of the incoming light. The amount of light reflected from each boundary can be calculated using the Fresnel equation. It depends on the difference in the refractive indices, the angle of incidence, and the wavelength

## CHAPTER 2. THICKNESS UNIFORMITY AND DAMAGE THRESHOLD MEASUREMENTS OF CRYSTALLINE GAAS/ALGAAS COATINGS

and polarization of the incoming light. The dielectric coating can have an arbitrary number of layers with alternating material and thus refractive indices (see figure 2.1). The reflection of each boundary interferes with the reflections from previous layers, combining them into a total reflection of the coating. In this way, reflectivities close to one and single parts per million (ppm) transmission can be achieved [Pra+18]. These coatings need to be designed for a specific wavelength at a specific angle of incidence.

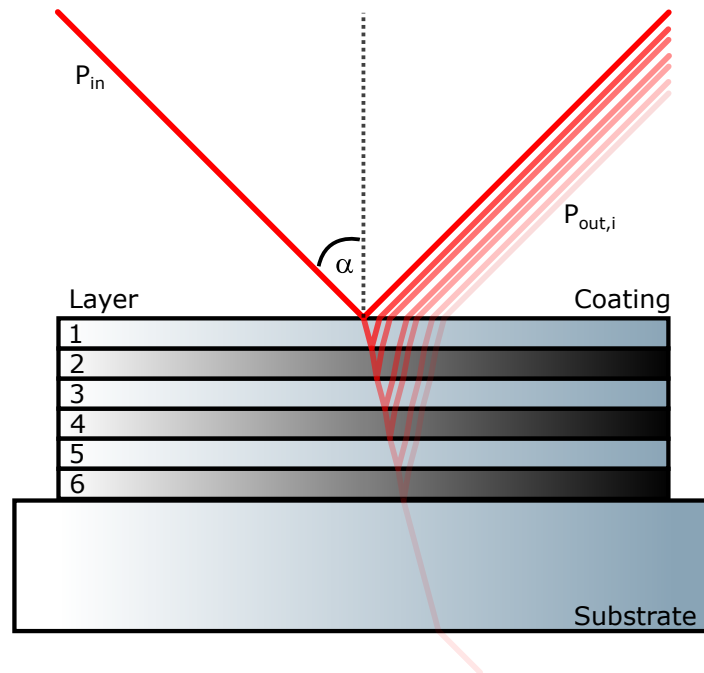


Figure 2.1: Schematic of a dielectric coating, reflecting an incident laser beam with power  $P_{in}$  at an angle of incidence  $\alpha$ . The reflected beams of each layer boundary  $i$  with their respective power  $P_{out,i}$  interfere constructively. The coating is not displayed up to scale as usually the thickness of each individual layer is much smaller than the diameter of the incoming laser beam. Secondary and further reflections are not shown.

One of the commonly used dielectric coating designs is the quarter-wave coating stack. High reflectivities with a minimal number of layers can be achieved when the reflection of each boundary constructively interferes with each other. This is the case when the phase of the reflected light from a boundary matches the phase of the light reflected at previous boundaries. Typically, the thickness of each layer equals an optical path length (OPL) of  $\lambda_0/4$ , where  $\lambda_0$  is the laser wavelength for which

## CHAPTER 2. THICKNESS UNIFORMITY AND DAMAGE THRESHOLD MEASUREMENTS OF CRYSTALLINE GAAS/ALGAAS COATINGS

the coating is designed. This results in a 180 deg round-trip phase change of the light. Additionally, a 180 deg phase shift occurs at each boundary where the laser beam is reflected from a material with a higher refractive index than the current material. The material of the first coating layer is often chosen as the material with the higher refractive index. This matches the phase of all following reflections to the reflection of the first boundary from the outside medium to the coating material. To fulfill the OPL of  $\lambda_0/4$ , the thickness of each layer needs to be adjusted when the angle of incidence differs from 0 deg. A schematic of a dielectric coating can be seen in figure 2.1.2.

In this chapter, we focus on crystalline dielectric coatings made from GaAs and AlGaAs. Fused silica ( $\text{SiO}_2$ ) and Tantalum ( $\text{Ta}_2\text{O}_5$ ) are often used as materials for dielectric coatings in the visible to near infra-red spectrum. They are deposited via ion-beam sputtering (IBS) on a substrate. Another approach, especially for infra-red light, are crystalline AlGaAs / GaAs coatings [Col+16]. They are grown on a GaAs wafer in an MBE chamber (see chapter 2.1.3). They usually consist of alternating layers of  $\text{Al}_{0.92}\text{Ga}_{0.08}\text{As}$  with a refractive index of 2.997 and GaAs with a refractive index of 3.480 measured by Crystalline Mirror Solutions (CMS). Crystalline coatings promise lower coating thermal noise (see chapter 1.2.4) compared to the  $\text{SiO}_2$  /  $\text{Ta}_2\text{O}_5$  coatings [Col+13].

### 2.1.3 Working principle of an MBE chamber

An MBE chamber allows controlled crystal growth on a lattice-matched crystalline substrate. Its basic components are a manipulator, carrying the substrate, and heated effusion cells. These components are placed inside an ultra-high vacuum (UHV) chamber to avoid contamination by residual gases and to increase the free path length of the molecules. A simplified set-up can be seen in figure 2.2. The effusion cells contain the various materials required to grow the desired crystal structures. The materials are heated to produce a molecular beam towards a substrate mounted on a heated manipulator. The manipulator can be rotated to allow a more uniform distribution of the growth process. Compounds like GaAs or AlGaAs can be grown by using multiple effusion cells simultaneously. Alternatively to the heated effusion cells, electron beams can be used to evaporate the growth materials and create the

## CHAPTER 2. THICKNESS UNIFORMITY AND DAMAGE THRESHOLD MEASUREMENTS OF CRYSTALLINE GAAS/ALGAAS COATINGS

molecular beams. The growth of a crystal requires a substrate with a matching atomic lattice and a chemical compatibility [HS96].

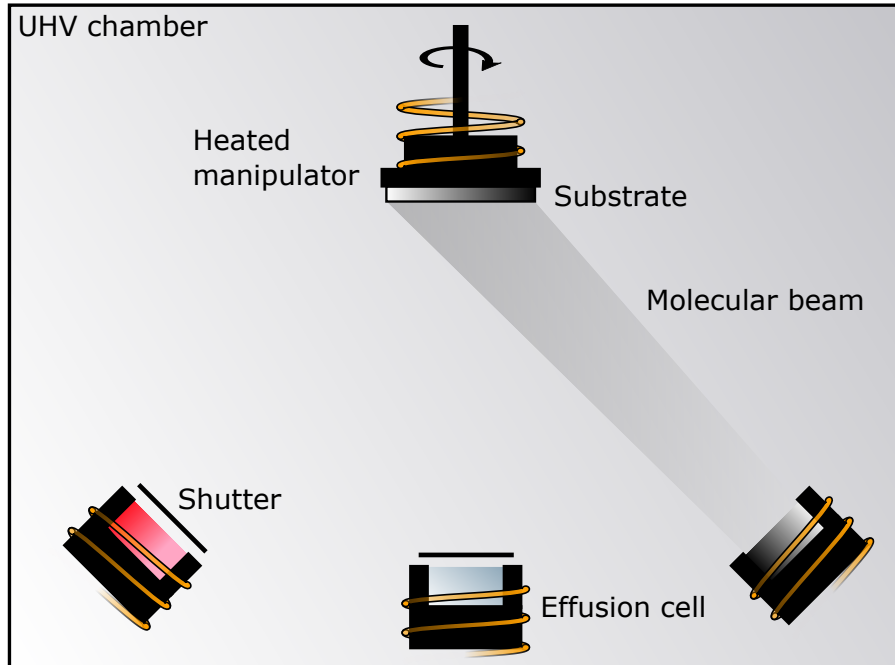


Figure 2.2: Simplified set-up of an MBE chamber. An UHV chamber containing effusion cells which can be heated to evaporate a material and create a molecular beam and a heated manipulator, carrying a substrate. The manipulator can be rotated to ensure a more uniform distribution of the growth material on the substrate.

The thickness of the coating layers is controlled by various growth parameters. To control the material ratio of a coating layer during the growth process, the evaporation rate can be tuned by the temperature of the effusion cells. Its rotation speed can be set to improve the thickness uniformity by constantly re-orientating the substrate relative to the molecular beam. The growth rate is mainly defined by the amplitude of the molecular beam and its distribution [HS96]. Depending on the growth rate, a growth time can be calculated to grow a crystal layer of the desired thickness onto the substrate.

### 2.1.4 Converting reflectivity into thickness uniformity

A reflectivity measurement of a quarter-wave coating stack can be converted into a thickness measurement, assuming a repetitive deposition of coating material in each layer. As described in chapter 2.1.2, the reflectivity of a quarter-wave

## CHAPTER 2. THICKNESS UNIFORMITY AND DAMAGE THRESHOLD MEASUREMENTS OF CRYSTALLINE GAAS/ALGAAS COATINGS

coating stack is dependent on the interference condition of the light reflected at each boundary. If one or more coating layers deviate from an OPL of  $\lambda_0/4$ , the constructive interference condition is not fully met, and the reflectivity of the coating is reduced. When a homogeneous thickness deviation of all layers can be assumed, it directly relates to a change in reflectivity of the full coating stack. In coating deposition procedures like IBS or MBE (see section 2.1.3), a homogeneous thickness deviation of the different layers can be assumed when the depositing parameters remain constant for all layers. E.g., the beam profile of the ion beam during IBS or the molecular beam during the MBE influences the material distribution and thus the thickness uniformity of each layer. If the beam profile remains constant over the full coating run, a repetitive deposition of coating material for each layer can be assumed.

The thickness uniformity of a coating can be calculated from its reflectivity map. As previously explained, the thickness of the coating stack can be measured by measuring its reflectivity. By measuring the local reflectivity at different positions of the coating, a thickness map can be drawn. The thickness map of the coating can be used to calculate the thickness uniformity. The spatial resolution of the reflectivity map directly converts into the spatial resolution of the thickness map. It limits the highest detectable spatial frequency, similar to the Nyquist frequency in signal theory [RC91].

The sensitivity of the conversion from reflectivity to the thickness of a coating can be changed by measuring at laser wavelengths and angles of incidence differing from its design value. Figures 2.3 and 2.4 show the simulated reflectivity of a quarter-wave coating stack designed for a specific laser wavelength  $\lambda_0$  of 1064 nm and an angle of incidence of 0 deg, as a function of the incoming laser wavelength and the angle of incidence. At and around the design parameters, a plateau with a relatively constant reflectivity can be seen. The wavelength is linearly dependent on the OPL and thus the thickness of the coating. The angle of incidence changes the OPL through each coating layer depending on its sinusoidal and the refractive index difference as described by Snell's law. Thus, the sensitivity of the conversion from reflectivity to thickness changes with the slope of the reflectivity function shown in figure 2.3 and 2.4. Combining a wavelength differing from the design wavelength and an angle of incidence differing from the design angle, a high sensitivity can be

## CHAPTER 2. THICKNESS UNIFORMITY AND DAMAGE THRESHOLD MEASUREMENTS OF CRYSTALLINE GAAS/ALGAAS COATINGS

obtained while using a commonly available wavelength of 1550 nm.

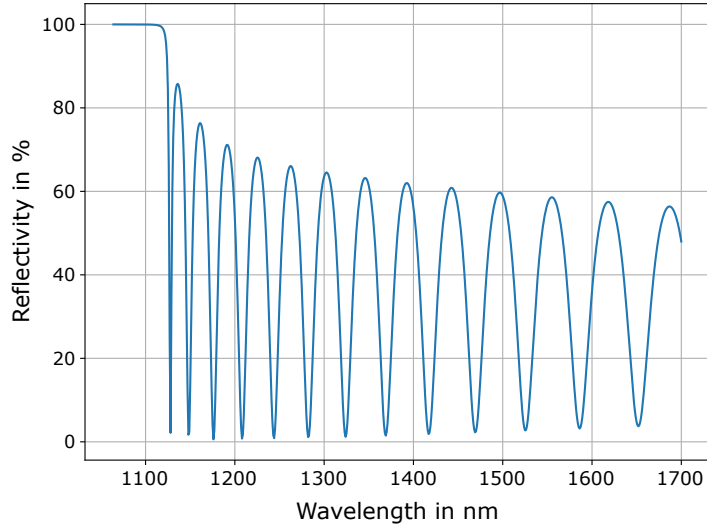


Figure 2.3: Reflectivity of a high reflective GaAs/AlGaAs quarter wave coating stack designed for a wavelength of 1064 nm and an angle of incidence of 0 deg in dependence of the incident wavelength. The simulation was made using the multidiel package for Matlab by S.J.Orfanidis. [Orf22]

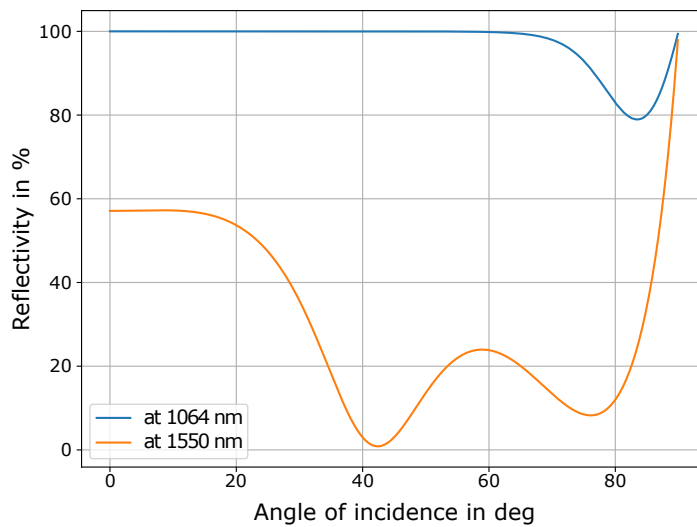


Figure 2.4: Reflectivity of a high reflective GaAs/AlGaAs quarter-wave coating stack designed for a wavelength of 1064 nm and an angle of incidence of 0 deg in dependence on the angle of incidence. The blue curve shows the reflectivity at a wavelength of 1064 nm. The orange curve shows the reflectivity at a wavelength of 1550 nm. The simulation was made using the multidiel package for Matlab [Orf22].

### 2.1.5 Measurement set-up

A reflectivity map can be measured using a laser, two photodiodes (PD) and a two-axis translation stage. Figure 2.5 shows the set-up used to measure the reflectivity maps. First, the laser is collimated by lens 1. A  $\lambda/2$  waveplate and a polarizing beam splitter (PBS) are used to adjust the laser power, as well as to ensure a linear polarization of the desired orientation. The reflection of the PBS is used as a power reference for the incoming laser beam. A second lens focuses the laser beam onto the sample. Both the transmitted and reflected beams can be measured directly on PDs, the latter via an additional third collimating lens. The sample is placed on a two-axis translation stage, moving it horizontally and vertically along the orientation of the reflecting surface.

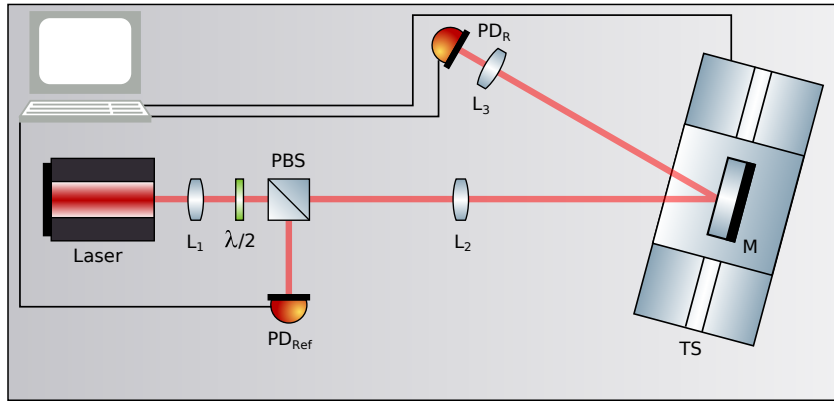


Figure 2.5: Set-up to measure reflectivity maps. A 1550 nm laser is collimated by a lens ( $L_1$ ). A  $\lambda/2$  retardation plate in combination with a PBS allows the power to be changed and provides a reference beam measured at the reference PD ( $PD_{Ref}$ ). A second lens ( $L_2$ ) focuses the laser beam onto the sample mirror (M). The reflected light is collimated at a third lens ( $L_3$ ) and measured by the reflection PD ( $PD_R$ ). The sample mirror is placed on a translation stage (TS) consisting of two linear stages and a rotation stage. One linear stage is orientated vertically, and the other is orientated alongside the rotatable horizontal axis.

For the measurements in chapter 2.2, two linear stages with a minimum step size of  $1 \mu\text{m}$  and a position-repeatability of  $20 \mu\text{m}$  were used. The system's linear stages were manufactured by ISEL and are mounted on a rotational stage allowing a rotation of the two linear stages. The linear stages allow mounting and scanning of optics up to a size of 50 cm in width and height. The laser is a temperature

## CHAPTER 2. THICKNESS UNIFORMITY AND DAMAGE THRESHOLD MEASUREMENTS OF CRYSTALLINE GAAS/ALGAAS COATINGS

stabilized, 10 mW distributed feedback (DFB) laser diode with a wavelength of 1550 nm. The reference and reflection PDs are Thorlabs 132C photodiode power sensors with a USB readout connected to a computer. A LabView software was used to control the translation stage while taking the data points from the PDs for the individual sample positions. The set-up was built within a bachelor project.

### 2.2 Thickness uniformity results for a crystalline, high reflective GaAs/AlGaAs coating

As discussed in chapter 2.1.1, a thickness uniformity below 0.3 nm RMS is required at large-scale gravitational wave detectors. Here, thickness uniformity results of an arm cavity end mirror style coating are shown and will be compared to X-ray diffraction measurements.

#### 2.2.1 Sample parameters

The sample under test is a highly reflective, crystalline coating, similar to arm cavity end mirror coatings of gravitational wave detectors. The coating sample is a dielectric quarter-wave coating stack consisting of GaAs and  $\text{Al}_{0.92}\text{Ga}_{0.08}$ . It was manufactured by CMS, which is now part of Thorlabs. It is designed for a wavelength of 1064 nm at an angle of incidence of 0 deg. A total of 71 alternating coating layers were grown onto a GaAs substrate and afterwards transferred to a 2 mm thick and 2 inch wide fused silica substrate. Of these 71 coating layers, 70 layers form 35 bilayers, fulfilling the quarter-wave stack condition with an OPL of  $\lambda_0/4$ . This results in a thickness of 76.43 nm for the GaAs layers and a thickness of 89.35 nm for the  $\text{Al}_{0.92}\text{Ga}_{0.08}$  layers. The 71st layer is another  $\lambda/4$  layer made from GaAs. The total thickness of the coating is  $6.15 \mu\text{m}$  at a diameter of 45 mm. It has a nominal transmission of 10 ppm at the design wavelength and angle of incidence.

The sample is one of four 45 mm sized cuttings from a 150 mm diameter coating stack. A total of seven coating stacks were grown simultaneously on 150 mm GaAs wafers. As shown in figure 2.6, are six orbital wafer positions and one center wafer position. After the growing process, lapping and wet chemical etching were used to remove the coating stack from the wafers [Col+16].

A first thickness analysis (see figure 2.7) was provided by CMS using x-ray and

CHAPTER 2. THICKNESS UNIFORMITY AND DAMAGE THRESHOLD MEASUREMENTS OF CRYSTALLINE GAAS/ALGAAS COATINGS

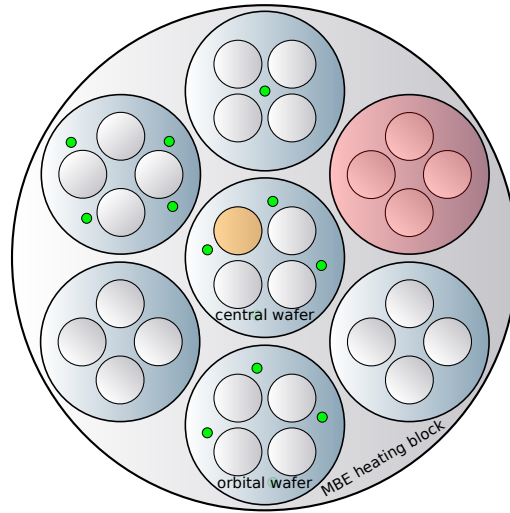


Figure 2.6: Arrangement of seven 150 mm diameter GaAs wafers on the MBE chamber's heating block. They are distinguished between six orbital wafers and one center wafer. Four 45 mm diameter coating stacks were extruded from each wafer. The sample position measured with a spectrophotometer is marked in red, sample positions measured with HRXRD are marked in green, and the sample for the thickness uniformity measurement is marked in orange.

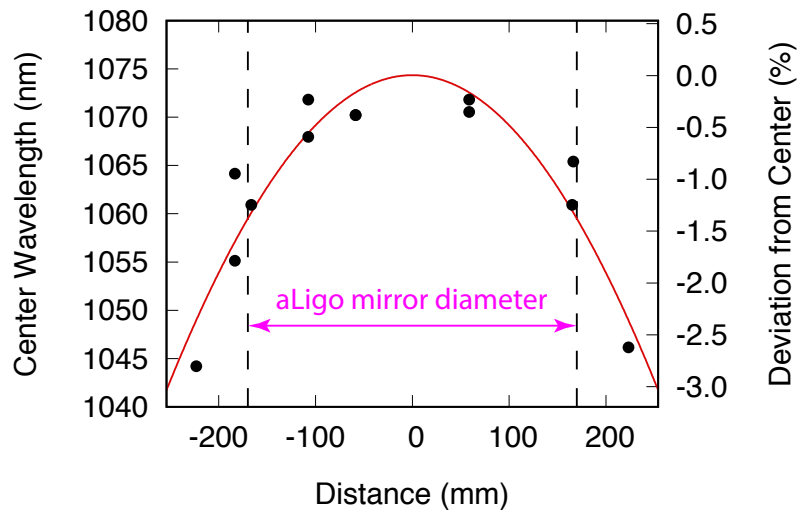


Figure 2.7: Evaluation of the HRXRD measurement. The thickness of the coating stack in units of the center wavelength in nm and the deviation from the thickness of the center position in % is plotted against the distance from the center of the MBE heating block [Koc+19]. The region indicated by "aLigo mirror diameter" is the inner region of the aLigo mirrors with the most stringent requirements for the surface uniformity.

## CHAPTER 2. THICKNESS UNIFORMITY AND DAMAGE THRESHOLD MEASUREMENTS OF CRYSTALLINE GAAS/ALGAAS COATINGS

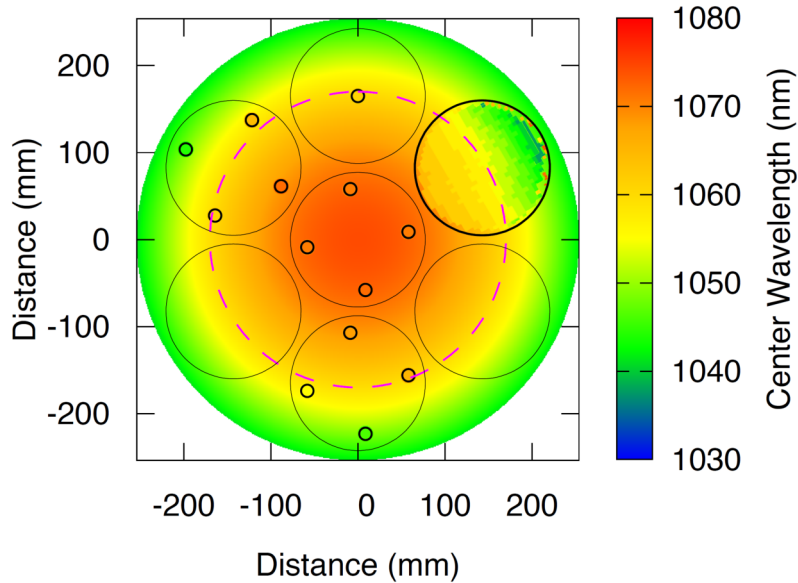


Figure 2.8: Evaluation of the HRXRD measurement as surface plot showing the plotted thickness deviation over the MBE heating block in units of the center wavelength. The upper right 150 mm meter wafer shows the results of a spectrophotometer measurement provided by CMS [Koc+19]

spectrophotometer measurements. Figure 2.6 shows the positions of the samples used for high-resolution x-ray diffraction measurements (HRXRD) in green and the sample measured with a spectrophotometer in red. The position of the 45 mm sample used in the following thickness uniformity measurement is marked in orange. A surface plot of the fitted thickness distribution, including the spectrophotometer measurement, is shown in figure 2.8.

### 2.2.2 Compensation of the rear surface reflection

A missing anti-reflective (AR) coating on the rear surface of a mirror can strongly influence the thickness uniformity described in chapter 2.1.4. For the thickness uniformity measurement, a 1550 nm laser was used. The GaAs/AlGaAs coating stack transmits a major part of the incoming light at this wavelength. This ensures that all coating layers contribute similarly to the total reflectivity. The test sample (see chapter 2.2.1) does not have an AR coating on its rear surface. Thus, the rear surface reflects a non-negligible portion of the light, interfering with the reflected

CHAPTER 2. THICKNESS UNIFORMITY AND DAMAGE THRESHOLD  
MEASUREMENTS OF CRYSTALLINE GAAS/ALGAAS COATINGS

light from the coating stack. This leads to the measurement being dependent on the thickness uniformity of the fused silica substrate. Figure 2.12 demonstrates the influence of a changed OPL through the substrate by applying a small rotation to the sample.

Two different methods have been used to reduce the influence of the rear reflection on the thickness uniformity measurement. The first method averages a set of two measurements with a phase shift of the rear reflection by 180 deg. The second uses index-matched bonding to a strongly scattering substrate to diffuse the rear reflection.

### Averaging of phase-shifted measurements

The phase of the rear reflection of a mirror can be tuned relative to the reflection of its coating with a negligible change in the coating's reflectivity. When rotating a mirror relative to the incoming laser beam, the interference conditions of the coating layers and the rear surface change (see chapter 2.1.4). As the thickness of the mirror substrate is much bigger than the thickness of the coating, the OPL change through the substrates far dominates the OPL change through the coating stack.

Averaging two measurements at a slightly different angle of incidence can compensate for the influence of the rear reflection on the total reflectivity of a mirror. This is the case if the OPL round trip length changes by  $\lambda/2$ . The OPL change of  $\lambda/2$  leads to a phase shift of 180 deg of the light reflected from the rear surface in between both measurements. It can be changed by rotating the sample mirror. To achieve an OPL change of  $\lambda/2$ , the required angle of incidence of the second measurement ( $\alpha_2$ ) can be calculated using trigonometric functions and Snell's law.

$$\alpha_2 = \arcsin \left[ \frac{n}{n_0} \cdot \sin \left[ \arccos \left[ \frac{t_s}{\lambda / (4 \cdot n) + t_s / (\cos(\arcsin(n_0/n \sin \alpha_1)))} \right] \right] \right], \quad (2.1)$$

where  $t_s$  is the thickness and  $n$  the refractive index of the substrate. The refractive index of the surrounding medium is given by  $n_0$ .  $\lambda$  is the laser wavelength, and  $\alpha_1$  is the angle of incidence of the first measurement.

Figure 2.9 shows the change of the measured reflectivity map for the two angles of incidence ( $\alpha_1$  and  $\alpha_2$ ), calculated according to equation 2.1. The averaged reflectivity

## CHAPTER 2. THICKNESS UNIFORMITY AND DAMAGE THRESHOLD MEASUREMENTS OF CRYSTALLINE GAAS/ALGAAS COATINGS

map can be seen in figure 2.10. Comparing both figures shows the impact of the non-uniform substrate thickness and the compensation potential of this method.

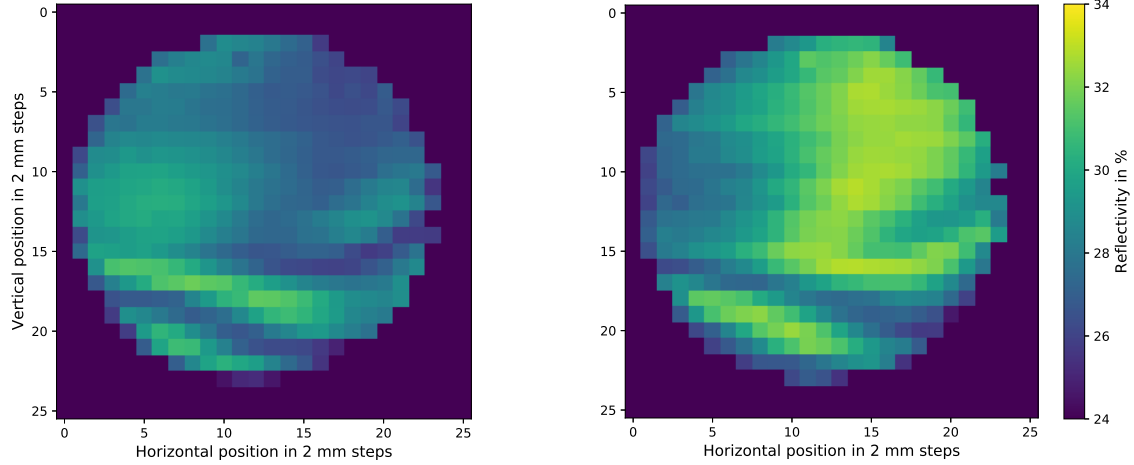


Figure 2.9: Reflectivity maps of the high reflective GaAs/AlGaAs coating stack presented in chapter 2.2.1. Both reflectivity maps were taken at an angle of incidence of around 20 deg, differing by 0.04 deg. This results in a phase shift of the light reflected at the rear surface of 180 deg, according to equation 2.1. The averaged reflectivity map can be seen in figure 2.10.

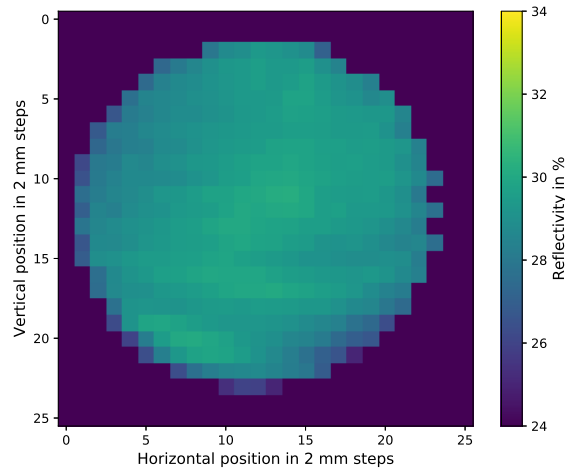


Figure 2.10: Averaged reflectivity map using the reflectivity maps shown in figure 2.9, showing the compensation of the rear reflection of the sample mirror.

## CHAPTER 2. THICKNESS UNIFORMITY AND DAMAGE THRESHOLD MEASUREMENTS OF CRYSTALLINE GAAS/ALGAAS COATINGS

### Index matched bonding

Bonding the sample to a low-reflecting substrate while matching their refractive indices reduces the power of the light reflected from the rear surface. As described by Snell's law, the reflectivity of a boundary is dependent on the refractive index difference of both media. The reflectivity of the boundary is zero if both refractive indices match.

A refractive index-matched fluid can be used as filling material in between two non-planar surfaces. To reduce the influence of the rear reflection of the mirror on the thickness uniformity measurement, a ground fused silica substrate was used. The sample was bonded to the ground substrate using glycerol (see figure 2.11). As the refractive indices of glycerol ( $n_{gl}$ ) and fused silica ( $n_{fs}$ ) are very close ( $\delta n = |n_{gl} - n_{fs}| = 0.02$ ), the reflectivity of the boundary in between both substrates is significantly reduced. The transmitted light was scattered at the rear of the ground substrate.

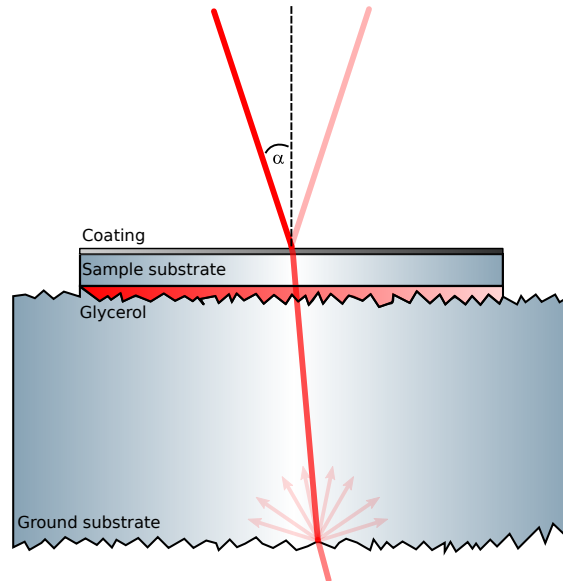


Figure 2.11: Laser beam reflected and transmitted by a mirror, bonded to a ground substrate using glycerol (red) as index matching fluid.

The results of the index-matched bonding can be seen in figure 2.12. Figure 2.12 shows the reflectivity of the sample as a function of the angle of incidence. As explained above, the angle of incidence-dependent reflectivity is dominated by the reflection from the rear surface. This results in an oscillation between constructive

## CHAPTER 2. THICKNESS UNIFORMITY AND DAMAGE THRESHOLD MEASUREMENTS OF CRYSTALLINE GAAS/ALGAAS COATINGS

and destructive interference. In blue, the reflectivity without index-matched bonding can be seen. The orange curve shows the reflectivity with index-matched bonding. A reduction of the oscillation's amplitude and thus the influence of the rear surface reflection of about a factor 20 can be seen.

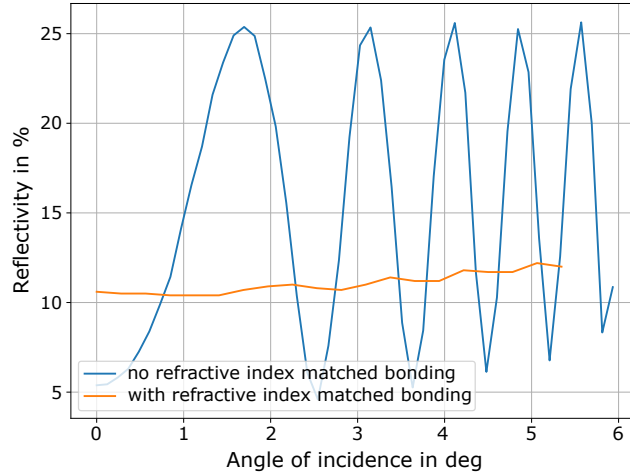


Figure 2.12: Reflectivity measurement of an GaAs/AlGaAs mirror designed for a wavelength of 1064 nm in dependence of the angle of incidence at a wavelength of 1550 nm. The blue curve shows a measurement without index matched bonding. The orange curve shows a measurement with index matched bonding.

### 2.2.3 Thickness uniformity results

The resulting thickness uniformity measurement of the HR GaAs/AlGaAs mirror (see chapter 2.2.1) can be seen in figure 2.13. The sensitivity of the measurement was enhanced (see chapter 2.1.4) by measuring at a wavelength of 1550 nm and an angle of incidence of 20 deg. To reduce the influence of the substrate's thickness uniformity, both techniques described in chapter 2.2.2 were used. The GaAs/AlGaAs mirror was attached to a ground substrate with a refractive index-matched fluid, and two phase-shifted measurements were taken for averaging. The laser beam's spot size on the mirror and the step size of the linear stages were adjusted to 1 mm.

The accuracy of the thickness uniformity measurement is  $\pm 0.05$  nm at a conversion factor of 1.41 nm/% from reflectivity to thickness uniformity. The accuracy was limited by the technical noise of the laser diode and the PDs. Measuring the reflected

CHAPTER 2. THICKNESS UNIFORMITY AND DAMAGE THRESHOLD MEASUREMENTS OF CRYSTALLINE GAAS/ALGAAS COATINGS

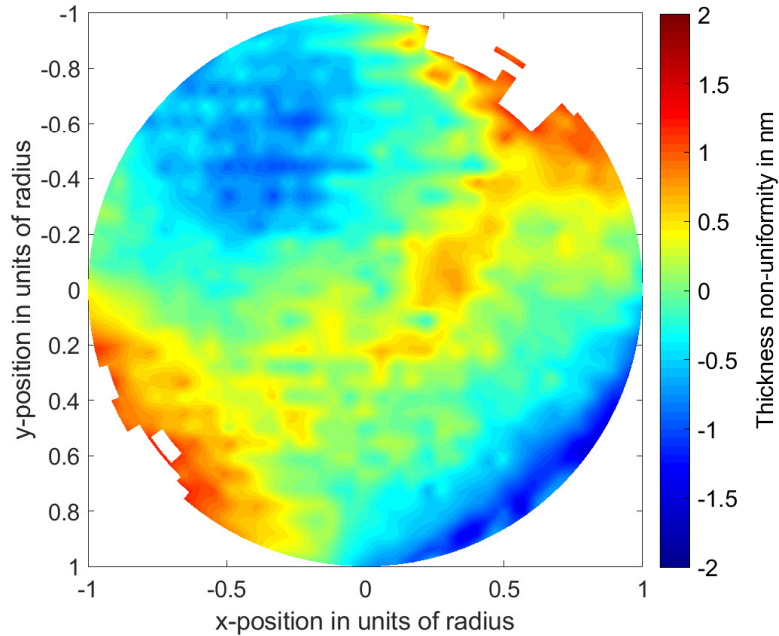


Figure 2.13: Thickness uniformity map of the GaAs/AlGaAs coating described in chapter 2.2.1. The x and y positions were transformed to radial coordinates to correct for the Zernike polynomials  $Z_0^0$ ,  $Z_1^{-1}$ ,  $Z_1^1$  and  $Z_2^0$ . Defects near the rim were omitted. The calculated thickness uniformity RMS value is  $0.41 \pm 0.05$  nm. This figure was also published in the corresponding paper [Koc+19]

power at a fixed mirror position, the combination of both noise sources could be measured to a standard deviation of  $\pm 0.03$  % reflectivity. This measurement was done at a constant mirror position over a similar duration as the thickness uniformity measurement.

To evaluate the thickness uniformity in terms of the coating's usage inside a gravitational wave detector or a cavity, certain Zernike polynomials can be corrected. Zernike polynomials can be used to describe radial surface plots and are often used in optical and imaging systems [LF11]. The Zernike polynomial  $Z_0^0$  describes the piston offset and can be compensated by a lateral adjustment of the mirror position inside a cavity.  $Z_1^{-1}$  and  $Z_1^1$  describe a horizontal or vertical gradient and can be corrected by pitching or yawing the mirror.  $Z_2^0$  describes the curvature of the coating adding up with the curvature of the mirror and can be compensated by mode-matching.

For the measured thickness uniformity (see figure 2.13), an RMS value of  $0.41 \pm 0.05$  nm can be calculated, including the removal of the following Zernike poly-

## CHAPTER 2. THICKNESS UNIFORMITY AND DAMAGE THRESHOLD MEASUREMENTS OF CRYSTALLINE GAAS/ALGAAS COATINGS

mials. A piston offset ( $Z_0^0$ ) of 13.3 nm was subtracted. A horizontal gradient ( $Z_1^1$ ) of 70 nrad and a vertical gradient ( $Z_1^{-1}$ ) of 57 nrad were corrected. The curvature ( $Z_2^0$ ) was corrected by  $0.024 \text{ km}^{-1}$ . The outer 2 mm and specific defects near the rim were omitted due to visible defects at the rim of the optic, which occurred during the bonding process.

The aLIGO detectors require a thickness uniformity of the end test masses between 0.19 nm and 0.29 nm RMS within the inner 160 mm diameter of the optic [BYZ17; J A+15]. The GaAs/AlGaAs coating was measured to 0.41 nm RMS within a diameter of 40 mm. The thickness uniformity comes close to the requirements for the measured area. The currently used IBS coatings at aVirgo were measured to have a thickness uniformity of 0.37 nm RMS [Pin+16]. The thickness uniformity of the aLIGO substrates reached an RMS value of 0.18 nm, while the surface uniformity of the mirror was measured to 0.69 nm RMS [J A+15]. This indicates a thickness uniformity of the coating of 0.67 nm RMS. Thus, it could be shown that within the measured sample size, GaAs/AlGaAs coatings can achieve a thickness uniformity comparable to state of the art IBS coatings.

### 2.3 Damage threshold test for a crystalline, high reflective GaAs/AlGaAs coating

In gravitational wave detectors and a variety of other laser-based set-ups, optical cavities are commonly used. Optical cavities lead to a power buildup, far surpassing the input laser power. For a combination of a high laser input power and cavities with a high power buildup, the material used for the optical components can reach its destruction threshold. This threshold is referred to as the laser-induced damage threshold (LIDT). In this section, the measurement of a lower limit for the LIDT of an HR GaAs/AlGaAs coating is described.

The LIDT of a coating or optic describes the power density or sometimes linear power density above which a coating or optic would be damaged. For continuous wave and long pulse lasers, the dominating damage mechanism is based on thermal effects. A coating or substrate is locally heated by the absorption of parts of the incoming light. The heating leads to mechanical stress building up due to the thermal expansion of the different materials. This can lead to delamination of

## CHAPTER 2. THICKNESS UNIFORMITY AND DAMAGE THRESHOLD MEASUREMENTS OF CRYSTALLINE GAAS/ALGAAS COATINGS

the coating from the optic or cracking of the coating [RJS09]. Above a certain material-dependent temperature, the coating or substrate melts and crystallizes or even evaporates [RJS09]. Another damage mechanism is the dielectric breakdown, where the laser beam induces a strong electric field in the dielectric coating material, causing electron avalanches. These locally heat the coating, damaging it in the process. This damage mechanism is usually not observed at CW or pulsed lasers with a pulse length greater than several nanoseconds [RF73].

### 2.3.1 Damage threshold test set-up

The measurement set-up for the damage threshold test can be seen in figure 2.14. A fiber amplified CW laser with a wavelength of 1064 nm is used. The laser beam is first widened and collimated to a beam radius of 5.5 mm by a pair of lenses. The third lens, with a focal length of 140 mm, focuses the beam down to a beam waist with a radius of  $9.2 \mu\text{m}$ . The lens set-up was previously tested with a knife-edge photodiode to confirm the waist size to an accuracy of  $\pm 0.2 \mu\text{m}$ . The sample mirror is placed onto a linear stage at the beam waist position. The linear stage slowly moves the optic along the beam axis to ensure that the mirror surface crosses the

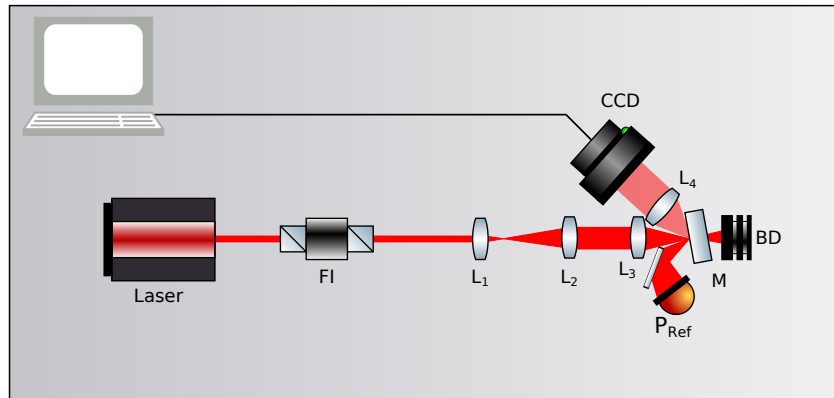


Figure 2.14: Damage threshold measurement set-up. A fiber amplified CW laser with a maximum output of 85 W is widened by  $L_1$  and collimated by  $L_2$  to a radius of 5.5 mm. A 140 mm focus length lens  $L_3$  focuses the laser beam down to a beam waist of  $9.2 \mu\text{m}$  radius. The sample mirror  $M$  is placed on a linear stage inside at the beam waist position. The reflected light is steered to a power meter ( $P_{ref}$ ), and the transmitted light is dumped at a beam dump (BD).  $L_4$  images the scattered light onto a CCD camera.

## CHAPTER 2. THICKNESS UNIFORMITY AND DAMAGE THRESHOLD MEASUREMENTS OF CRYSTALLINE GAAS/ALGAAS COATINGS

beam waist. The laser power is then increased after each time the mirror crosses the beam waist to a maximum of 85 W. An L250W power meter from Ophir is used in the reflected path to monitor the laser power. It has a power accuracy of  $\pm 3\%$ . An additional lens images the scattered light onto a charged-coupled device (CCD) camera to inspect changes and to confirm damage to the mirror surface.

### 2.3.2 Damage threshold results

A lower limit of the LIDT of an HR GaAs/AlGaAs coating could be measured to be  $64 \pm 5$  MW/cm<sup>2</sup>. The coating resisted the maximum power of 85 W of the laser at a spot size of 9.2  $\mu$ m. Assuming a Gaussian beam profile, equation 2.2 can be used to calculate the intensity at the beam waist with a radius  $\omega_0$  [Sel83].

$$I_0 = \frac{2 \cdot P_0}{\pi \cdot \omega_0^2}, \quad (2.2)$$

where  $I_0$  is the intensity at the waist position and  $P_0$  the laser power. To ensure no particles or defects on the coating surface were hit, the CCD camera was used to avoid high scatter points during the positioning of the optic.

An LIDT of  $64 \pm 5$  MW/cm<sup>2</sup> is well above the intensities of 17 kW/cm<sup>2</sup>, which are currently used in the aLiGO detectors [J A+15]. To compare the LIDT to commercially available dielectric coatings, the linear power density (LPD) will be used. The following equation to calculate the LPD is taken from the Thorlabs web page [Tho22a] and was used to calculate the LIDT of several Thorlabs optics.

$$LPD = \frac{P_0}{2\omega}, \quad (2.3)$$

where  $P_0$  is the laser power and  $\omega$  is the beam radius. The resulting lower limit of the LIDT of GaAs/AlGaAs coatings with an LPD of  $46.2 \pm 2.4$  kW/cm compares well to the measured LIDT of Thorlabs laser line mirrors for a wavelength of 1064 nm with an LPD of 20 kW/cm.

# Chapter 3

## Scatterometer

---

This chapter presents an optical scatter measurement device called the *scatterometer*. Optical scattering describes the reflection or transmission of light from an object in any direction, deviating from the nominal reflection and transmission. It is caused by, e.g., imperfections of the object's surfaces. In this thesis, optical scattering is referred to as scattering.

Scattering is an important parameter of optical components in gravitational wave detectors. It can generate noise in the output signal when scattered towards non or insufficiently seismically isolated components of the set-up. These partially reflect or scatter the light back into the interferometer, where it couples into the output path of the detector. Another important aspect of scattering is the optical loss in cavities. Here, the amplified light field can lose a non-negligible part of its power.

One way to characterize scattering is the bidirectional reflection distribution function (BRDF). The BRDF describes the light's power scattered towards different solid angles relative to the nominal reflection. Further, it can be used to calculate the total integrated scattering (TIS), describing the scatter losses of an optic.

The scatterometer measures the BRDF of a sample. This can be used to estimate the TIS and gain information on its surface quality. As scattering is similarly important to the sub-SQL interferometer as for a gravitational wave detector, the scatterometer is required to characterize optical components for the AEI 10 m prototype.

In the first section, this chapter gives an overview of different scatter calculation methods, including Rayleigh, Mie and Fourier scattering. Further, the BRDF is introduced as a method to quantify scattering. In the second section, a set-up to measure the BRDF of an optical surface is presented.

## 3.1 Optical scattering

In most applications, it is sufficient to know the direct reflection and transmittance of a laser beam, incident on an optical surface. Upon closer inspection, additional light is reflected or transmitted at different angles depending on imperfections of the optic's surface. These imperfections can be described as local impurities or spatial wavelength superposition of the surface. The light reflected from or transmitted through these imperfections leaves the intended beam path and is called scattering. Forward scattering is light being transmitted through the optic at a different angle and shape than the nominal transmitted light. Backward scattering is the light reflected at different angles than the nominal reflection. In this chapter, the focus lies on backscattered light, so the light scattered into the half-sphere pointing towards the incident beam. The TIS in this thesis relates to the reflected TIS.

To calculate the scatter distribution caused by surface imperfections, different approaches can be used, depending on the dimension of the imperfection. The wavelength of the incident light is compared to the size of the impurity or the spatial wavelengths of the non-perfectly flat surface. If the impurity size is much smaller than the light's wavelength, Rayleigh scattering is used to describe the scatter distribution. Mie scattering describes scattered light with an impurity size comparable to the wavelength. Fourier scattering is used to describe scattered light from a superposition of spatial waves on the optic surface, larger than the light's wavelength. The BRDF, as angle-dependent scatter measure, includes the superposition of Rayleigh, Mie and Fourier scattering.

### 3.1.1 Rayleigh scattering

Scattered light with a wavelength much larger than the scattering particle is called Rayleigh scattering. It is often depicted with the scattering of light from molecules and used for the study of gases [MLF01]. For most optical applications, it is of less interest than Mie or Fourier scattering, as the scattering amplitude is small compared to scattering of larger imperfections covered in 3.1.2 and 3.1.3. Nonetheless, a low level of Rayleigh scattering can be observed in substrates used in gravitational wave detectors.

### 3.1.2 Mie scattering

The scattering from a sphere with a similar size compared to the optical wavelength was first calculated by Gustav Mie [Pen57]. Mie scattering can be calculated by integrating a function of the total light field inside the sphere while setting some constraints on its properties [DG85]. These constraints include a real index of refraction and a homogeneous, non-magnetic sphere. The integration of the light field inside the sphere can be approximated using, e.g., the Rayleigh-Gans approximation [KFM63]. Mie scattering on optical surfaces can occur from point defects or contaminations [BR86; Gre07]. At high-quality optics, point scatterers often dominate the BRDF, likely originating from Mie scattering.

### 3.1.3 Fourier scattering

The Fourier scattering of optical surfaces is dominated by its micro-roughness. The micro-roughness is described by the superposition of spatial waves of the non-perfectly flat optical surface with wavelengths exceeding the wavelength of the incident light. Observing, e.g., the reflection from such a surface, its far-field power distribution can be described with the aid of the surface's Fourier transform. For optics dominated by Fourier scattering, the BRDF can be used to calculate the amplitude spectrum of the spatial waves of the optic's surface.

### 3.1.4 The BRDF

The BRDF describes the scattered laser power ( $P_s$ ) from an optical surface into a solid angle ( $\Omega$ ) as a function of the scattering angle ( $\Theta_s$ ). It is dependent on the input laser power ( $P_i$ ). The power distribution of scattered light is dependent on the amplitude of the spatial waves of an optical surface. Thus, scattering into any solid angle can be described as a function of the scattering angle. Here, the scattering angle is the angle in between the observed solid angle and the nominal reflection or transmission. The BRDF can be calculated with the following equation from [Sto90].

$$BRDF(\Theta_s) = \frac{P_s}{P_i \cdot \Omega \cdot \cos \Theta_s} \quad (3.1)$$

The reflected TIS (*RTIS*) for the half-sphere pointing toward the incoming laser beam can be calculated from the BRDF, assuming the scattering is independent of the rotation angle ( $\Phi_s$ ) of the optic around the beam axis [Mag+12]. The minimal and maximal scattering angle of the BRDF is defined by  $\Theta_{min}$  and  $\Theta_{max}$ .

$$RTIS = \int_0^{2\pi} \int_{\Theta_{min}}^{\Theta_{max}} BRDF \cos \Theta_s d\Theta_s d\Phi_s \quad (3.2)$$

## 3.2 Measuring the BRDF

This section will give a detailed overview of how a ppm-level scatter measurement can be achieved. Results of optical components with varying surface quality will be presented after introducing the experimental set-up and calibration of the measurement device. Section 3.2.1 introduces how the scattered light is measured and evaluated from a camera picture using a python script. The set-up is explained in section 3.2.2, including information about the individual components and devices. 3.2.3 presents two different calibration methods to calibrate the measurement device to output a BRDF in the units of  $Str^{-1}$ .

### 3.2.1 Measurement principle

As mentioned in 3.1.4, the BRDF is defined by the ratio of the scattered laser power at the scattering angle to a solid angle and the incident laser power. Thus, a measurement of the scattered laser power at a specific angle into a solid angle is required to calculate the BRDF. This information will be obtained by taking pictures at the corresponding scattering angles. The solid angle is then defined by the size of the lens, imaging the optical component onto the camera chip. The summed brightness of the individual pixels closely around the incident laser spot indicates the power of the scattered light. Figure 3.1 shows such a picture as a map of brightness values taken by the scatterometer camera. Only values within the

marked area are used for the BRDF calculations to minimize the influence of light scattered from the optic's edge or the mounting structure.

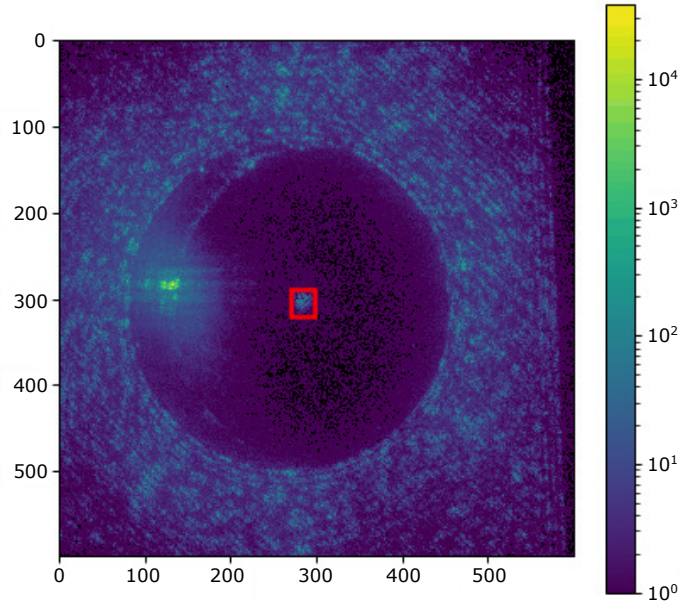


Figure 3.1: Map of brightness values measured at a scattering angle of 15 deg. The camera's pixel numbers are displayed on the x and y-axis, while the camera count per second is shown on the color bar. A 10 mW laser with a wavelength of 1064 nm was used for the measurement. The red rectangle indicates the area used for the calculation of the scattered light power.

The width ( $w$ ) of the red rectangle (see figure 3.1) reduces with the cosine of the scattering angle (see equation 3.3). This allows keeping track of the shrinking area of interest, thus minimizing the influence of scattering from the optic mount.

$$w = w_0 \cdot \cos \Theta_s, \quad (3.3)$$

where  $w_0$  is the predefined width of the rectangle, which can be set according to the laser spot size at  $\Theta_s = 0$ . The scattered power  $P_s$  can be calculated from a brightness map using

$$P_s = \sum_{a=h}^H \sum_{b=v}^V M_{ab} \cdot C \quad (3.4)$$

Here,  $M$  represents the brightness map with the coordinates  $a$  in horizontal and  $b$  in vertical direction.  $h$  is the minimum and  $H$  the maximum horizontal pixel number, while  $v$  is the minimum and  $V$  the maximum vertical pixel number. Thus,  $M_{hv}$  represents the upper left and  $M_{HV}$  the bottom right corner of the red rectangle shown in 3.1.  $C$  is a calibration factor converting camera counts at an exposure time of 1 s into light power in Watt. The determination of  $C$  can be found in 3.2.3.

The brightness map  $M_{ab}$  has a camera-dependent pixel-depth  $N$ , reaching from 0 to  $2^N-1$  counts [cts], where 0 cts means no light is hitting the pixel and  $2^N-1$  cts resembles a saturated pixel. Usually, the exposure time needs to be set to ensure that no brightness information is lost. Hence, no saturated pixels should be present within the region of interest. Without a correspondingly high pixel-depth, strongly scattering features would lead to data losses in the darker regions of a brightness map. To increase the information depth, several brightness maps with different exposure times can be taken for each scattering angle and normalized to an exposure time of 1 s using

$$norm(M_{ab\Theta_s t}) = M_{ab\Theta_s t} \cdot \frac{1}{t}, \quad (3.5)$$

where  $M_{ab\Theta_s t}$  is the brightness map  $M_{ab}$ , taken for a scattering angle  $\Theta_s$  and an exposure time  $t$ . The resulting brightness maps for each scattering angle can be combined, using the map with the maximum exposure time as the starting point. All saturated pixels are then replaced with pixels of a brightness map with a lower exposure time. This can be utilized successively until the minimum exposure time of the camera is reached. With this method, it is possible to use the full information depth at the maximum exposure time while not losing any scatter information due to saturation.

The error of this measurement method depends, alongside the calibration and the presence of external light sources, on pixel errors. There are two different pixel

type errors, which can influence the measured scattered power  $P_s$ . The first type is called hot pixel or stuck pixel, indicated by a bright pixel displaying a constant value. The second type is called a dead pixel, describing a pixel that always reads 0 cts. The amount of dead and hot pixels are defined in the pixel error class of the camera. The highest and thus worst error class stated in the ISO norm (ISO9241) limits the amount of dead and hot pixels to one out of 10000. As dead pixels only influence a BRDF measurement when they cover a significant area of the picture, they can be neglected in most cases. Nonetheless, a characterization of the used camera should be done to ensure a low, well-distributed number of dead pixels. On the other side, hot pixels can have a significant influence on the scatter measurement. In measurements of high-quality optics, the brightness value of even one hot pixel might exceed the summed brightness of all other pixels. This would lead to a measurement dominated by pixel errors. To reduce the influence of the hot pixels, a dark image can be subtracted from each brightness map, turning hot pixels into dead pixels. The dark image is taken by fully covering the camera while taking an image. In this case, all pixels are expected to show a brightness value of zero, and hot pixels, as well as their individual brightness, can be determined. As this can be dependent on the exposure time, an individual dark image should be taken and subtracted from each brightness map measured at the respective exposure time.

The composed brightness maps can be used to first determine the scattered power  $P_s$  for each scattering angle  $\Theta_s$  as in 3.4. Then the BRDF can be calculated using equation 3.1 and the experimental parameters, such as laser input power  $P_i$  and solid angle  $\Omega$ .

### 3.2.2 Scatterometer set-up

The set-up of the scatterometer is inspired by the scatterometer built at the California State University Fullerton [Mag+12]. It was build with the help of Jose I. Adorno, a summer student at that time [Ado19].

In figure 3.2 a schematic of the set-up can be seen. The scatterometer consists of a polarized laser beam collimated by a pair of lenses. An additional aperture reduces the amount of light scattered from the lenses into the camera at low scattering angles. The laser beam is then reflected by the sample, and the specular reflection

## CHAPTER 3. SCATTEROMETER

is dumped by a low scattering beam dump. All these components are mounted onto a rotation stage, rotating around the spot position of the laser beam on the sample. A stationary camera is used to observe the scattered light from different scattering angles. An imaging lens is used to image the sample onto the camera chip.

At low scattering angles, the beam dump and laser are blocking the camera, limiting the measurement range. Here, longer arms installed on the rotation stage can increase the measurement range towards low scattering angles. In the scatterometer set-up, an arm length of 50 cm was chosen, limiting scatter measurements of 1 inch optics to scattering angles above 4 deg. At high scattering angles, the laser spot on the sample, as seen by the mirror, reduces with the cosine (see equation 3.3). The measurement range there is limited by the shape of the optic mount, the alignment of the sample and the spatial resolution of the camera image. Often, scattering from the optic's edge can overlap with the laser spot, making it hard to measure optics above a scattering angle of 60 deg.

As an input laser, a polarized 10 mW laser pointer with a wavelength of 1064 nm is used. Depending on its orientation, measurements with both s and p-polarized light can be taken. The laser pointer is collimated to a spot size radius of 1 mm.

Figure 3.3 shows the CAD model of the scatterometer and its components. The camera is a Basler ace acA2040-55um. It provides  $2048 \times 1536$  pixels on a  $7.1 \text{ mm} \times 5.3 \text{ mm}$  camera chip. Its pixel depth is 12 bit at a maximum exposure time of 10 s. The imaging lens is a VIS-NIR-objective with a focal length of 50 mm and a diameter of 27 mm. It is placed at a distance of  $d = 60 \text{ cm}$  from the sample. The resulting solid angle is  $\Omega = 0.0064 \text{ Str}$ . To avoid environmental illumination disturbing the scatter measurements, a long pass filter glass is installed in front of the imaging lens, filtering wavelengths below 900 nm. To further reduce the influence of environmental light, a housing was installed around the scatterometer.

The measurement process is automated using a python script. As described in chapter 3.2.1, it takes images with different exposure times for each scattering angle. The measurement range and interval can be set from -90 deg to 90 deg with a step size of down to 0.01 deg. The script combines all images taken at one scattering angle to a brightness map in units of  $\text{cts s}^{-1}$ . A separate python script is used to calculate the BRDF from the array of brightness maps. Further, a GIF file can be created displaying the brightness images while drawing the BRDF function (see

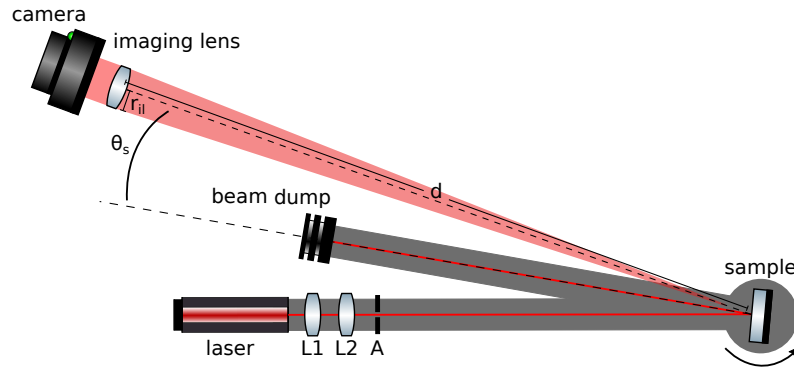


Figure 3.2: Experimental set-up of the scatterometer. A stationary camera measures the scattered light from a sample mirror on a rotation stage. The laser which is illuminating the optic is attached to the rotation stage. Additionally, two lenses (L1 and L2) can be used to change the spot size on the sample. An aperture A reduces the scattered light from the lenses and the optic mounts entering the camera.  $r_{il}$  is the radius of the imaging lens and  $d$  its distance from the sample. The rotation stage and the attached arms are shown in gray.

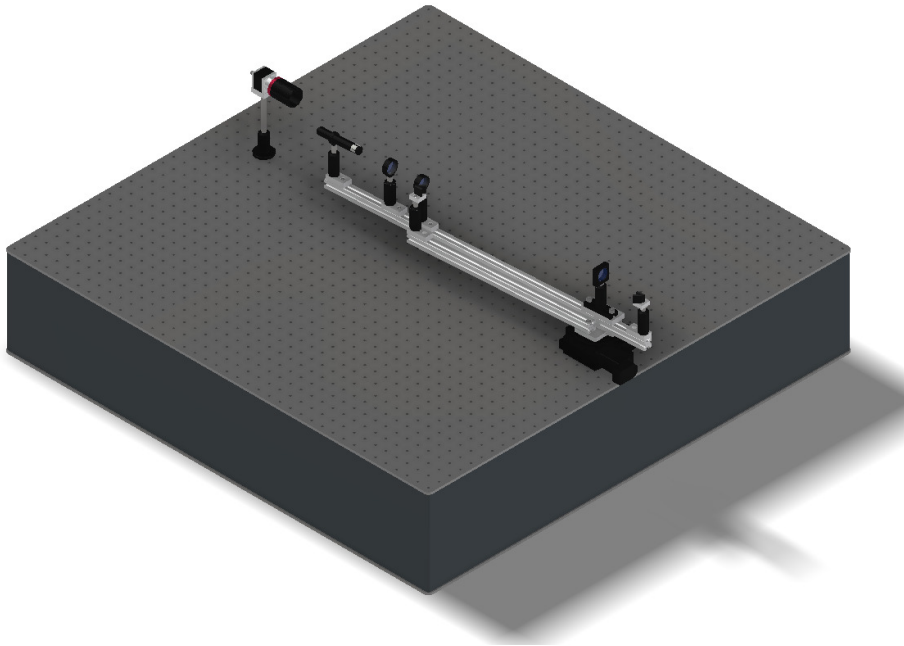


Figure 3.3: CAD model of the experimental set-up of the scatterometer. The stationary camera and the laser and lenses attached to the rotation arms can be seen on the upper left. The sample on the rotation stage and a beam dump for the transmitted light can be seen on the lower right.

figure 3.4) to identify the origin of features appearing during the measurement.

In figure 3.4, the measurement of a high-quality optic with high polishing

requirements can be seen. The TIS of the optic was measured to be below 0.1 ppm for a laser spot size radius of 1 mm. This shows the very high sensitivity of the scatterometer. Its measurement results are used further in chapter 5 to build a low loss cavity. Chapter 5 also includes further scatterometer measurements of optics with similar surface quality.

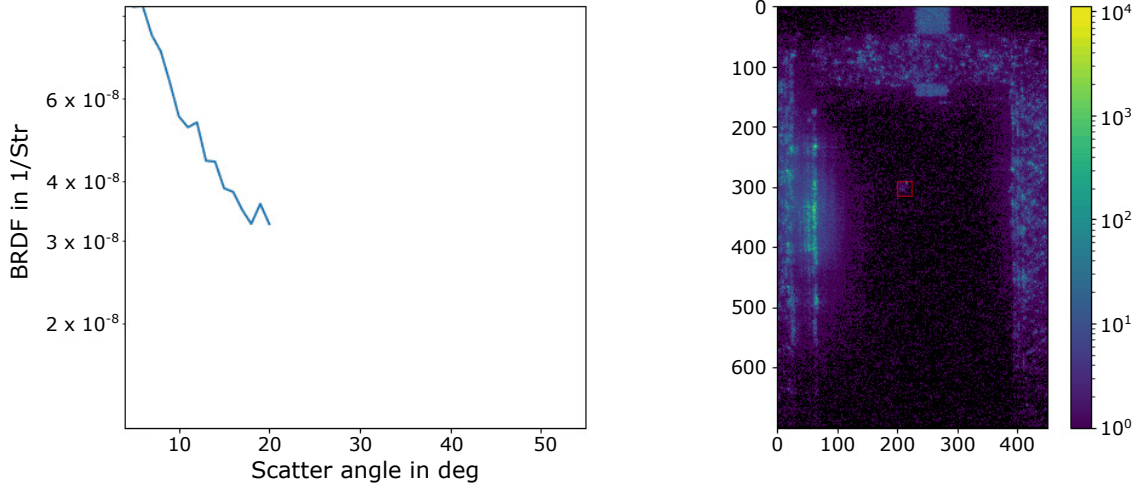


Figure 3.4: Image from a GIF file created from a scatterometer measurement. On the left, the BRDF is plotted, while on the right side, the brightness map of the currently plotted scattering angle is shown. The pixel coordinates of the brightness map are displayed on the x- and y-axis, while the pixel count per second is shown on the color bar.

### 3.2.3 Calibration of the scatterometer

This section will present two methods to calibrate the scatterometer. To determine the BRDF in units of  $\text{Str}^{-1}$ , the scattered power has to be calibrated to Watt. As described in 3.2.2, the brightness maps as returned by the measurement script are in units of counts per second ( $\text{cts s}^{-1}$ ). Using the equation 3.4 from chapter 3.2.1 the calibration factor  $C$  in units of  $\text{Wscts}^{-1}$  has to be measured. This can be achieved by using a calibrated sensor to measure the scattered power and comparing it to the scattered light seen by the camera. The second method requires a highly reflective Lambertian scatterer [Kop14] or a sample measured with an already well calibrated scatter measurement device. Each of these could be compared to the results obtained with the scatterometer and used for calibration.

## CHAPTER 3. SCATTEROMETER

For the first method, a photodiode power sensor S130C from Thorlabs was used. A long pass filter glass was installed in front of the power sensor to ensure that the measurement was purely dominated by light scattered from the sample. Further, a highly reflective sample with a rough surface was chosen to increase the amount of scattered light. After taking the brightness map, the camera and imaging lens were replaced by the S130C power meter within the same distance to the sample. The measured power was  $P_{PD} = 285 \pm 15 \text{ nW}$  on a circular sensor with a radius of  $r_{PD} = 5 \text{ mm}$ . This was compared to  $P_{CAM} = 2.998 \cdot 10^9 \text{ cts s}^{-1}$ , as the sum of all pixels of the brightness map. By applying the ratio of the solid angles of the power sensor and the imaging lens ( $r_{il} = 13.5 \text{ mm}$ ), the calibration factor  $C$  was calculated.

$$C = \frac{P_{PD}[W]}{P_{CAM}[cts \text{ s}^{-1}]} \cdot \frac{\Omega_{il}[Str]}{\Omega_{PD}[Str]} = 6.93 \cdot 10^{-16} [W \text{ s cts}^{-1}], \quad (3.6)$$

with

$$\Omega_{il} = \frac{\pi r_{il}^2}{d^2} \quad (3.7)$$

and

$$\Omega_{PD} = \frac{\pi r_{PD}^2}{d^2}, \quad (3.8)$$

where  $d$  is the distance of the power sensor and imaging lens from the sample as seen in figure 3.2.

For the second method, a sample with a known scatter performance could be measured to find the calibration factor needed to fit the scatterometer measurement to the known BRDF. It is also possible to measure a high reflective Lambertian scatterer. A Lambertian scatterer is known to have a constant BRDF. As the sample would be highly reflective, the TIS of the reflected light would equal one. The calibration factor  $C$  could be determined by

$$C = \frac{1}{TIS_{SC}}, \quad (3.9)$$

where  $TIS_{SC}$  is the total, integrated scattering determined from the BRDF of the Lambertian scatterer measured with the scatterometer.

Due to the lag of a well-known sample, the first described calibration method was chosen. The total measurement error of the scatterometer is dominated by the calibration. Here, the largest known error is the measurement uncertainty of the power meter with  $\pm 5\%$ .

### 3.2.4 Scatterometer results for a set of high quality optics

In figure 3.5, the BRDF of a set of high-quality optics can be seen. All optics were polished down to a micro-roughness RMS of below 0.5 nm. Afterwards, they were coated with a high reflective coating for an angle of incidence of 12.5 deg to be used in the OMC of the sub-SQL interferometer (see chapter 5). Their TIS is below 0.1 ppm at scattering angles ranging from 4 deg to 55 deg. The measurement range was limited by scattering from the optic's mount above 55 deg. For comparison, an additional BRDF was taken at a non-directly illuminated part of optic #2. This BRDF can be seen as a total noise approximation for this set of measurements. Varying optic sizes, shapes and mounts can influence the noise floor. The measurement shows that the scatterometer is well suitable for BRDF measurements of optics with a TIS down to 0.01 ppm.

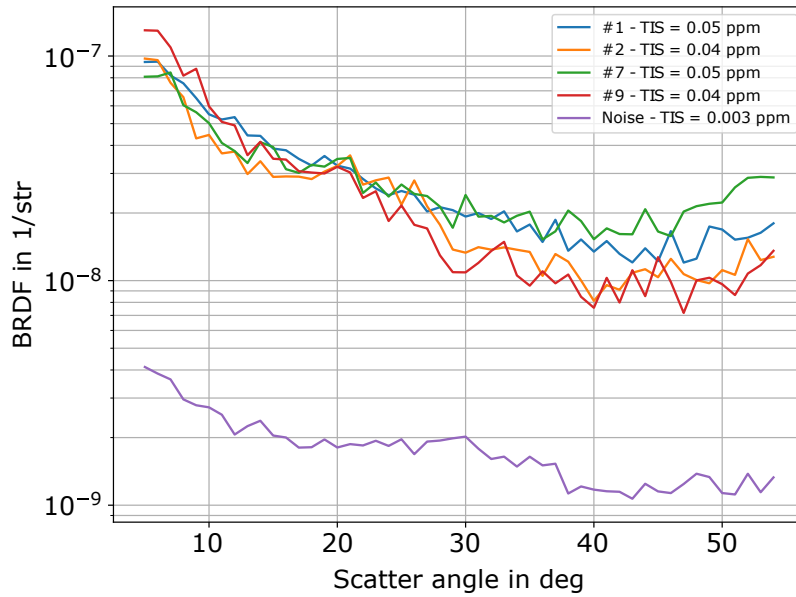


Figure 3.5: BRDF measurement of a set of high quality optics for the OMC of the sub-SQL interferometer. The legend shows the sample number and the corresponding calculated TIS. To demonstrate the sensitivity of the scatterometer, the four lowest scattering optics were selected.

## Chapter 4

# Beam splitter for the sub-SQL interferometer

---

In this chapter, the design of the beam splitter (BS) for the sub-SQL interferometer of the AEI 10 m prototype is presented alongside its triple suspension design. In section 4.1, the design requirements and choices for the BS optic are presented. They include the choice of the material, the required surface polishing, the coating and the final shape design. A split coating design was tested, yielding promising results for smaller BS designs in interferometric set-ups. The design of a triple suspension for the sub-SQL interferometer's BS and its design choices are discussed in section 4.2.

## 4.1 Beam splitter design

The beam splitter is one of the core optics of a Fabry-Perot Michelson interferometer. Most of its requirements are lower compared to the input and end test masses [Aku+21]. Nonetheless, there are some specific requirements for the coating and the shape which need to be taken into account. The design steps and requirements for the beam splitter optic are discussed in this section.

### 4.1.1 Optical requirements

The beam splitter optic consists of a polished substrate, a front, and a rear coating. Each of these has different requirements defined by its individual purpose. The substrate material forms the main body and shape of the beam splitter and influences the absorption of laser light passing through the optic. Polishing the substrate reduces the RMS of the surface roughness, which reduces the amount of scattered light, as described in chapter 3.1.4. A perfect 50/50 splitting ratio for the front coating prevents classical radiation pressure noise from causing differential arm length motion. Further, an anti-reflective (AR) coating reduces the laser power in unwanted reflections from the rear surface.

#### Substrate material

The BS substrate for the sub-SQL interferometer of the AEI 10 m prototype is made from Suprasil 311, which is high-grade fused silica ( $\text{SiO}_2$ ). It was produced by Heraeus and provides a low absorption and a high homogeneity of the refractive index [Her22]. Fused silica is a commonly used material for high-quality mirror substrates at wavelengths ranging from near-ultraviolet to near-infrared radiation.

The low absorption is essential to avoid local heating of the substrate, which in turn causes unequal expansion and thus creates thermal lenses. For most applications, the curvature of the arising thermal lens is small and can be neglected as long as the substrate material has a low absorption coefficient for the used laser wavelength.

To determine the required material properties for the SQL interferometer, a comparison with the GEO 600 detector [Wil+02] was made. The thermal lens forming in the beam splitter substrate of the GEO 600 detector has a focal length of about 1 km at a laser power of 20 kW [Wit09]. The GEO 600 beam splitter is made

## CHAPTER 4. BEAM SPLITTER FOR THE SUB-SQL INTERFEROMETER

from Suprasil 311SV. As the AEI 10 m prototype uses less than 10 W of laser power transmitting through the beam splitter substrate, the absorption performance of Suprasil 311 is sufficient for the about 5 cm thick beam splitter substrate.

### Polishing

As described in chapter 3.1.4, the power of the scattered light is directly dependent on the micro-roughness of the surface of an optical component. Thus, the pre-polishing of the substrate surface is essential for low scattering.

One surface quality parameter is the surface flatness. It describes the peak to valley (PV) deviation of the substrate surface from a flat surface. It is defined in units of the wavelength used for the flatness measurement [Edm22]. The requirements for the surface flatness were set to  $\lambda/20$  for the inner area (see the green area in figure 4.1) and  $\lambda/5$  for the outer area (red area in figure 4.1) of the front and rear surface at a wavelength of 632.8 nm.

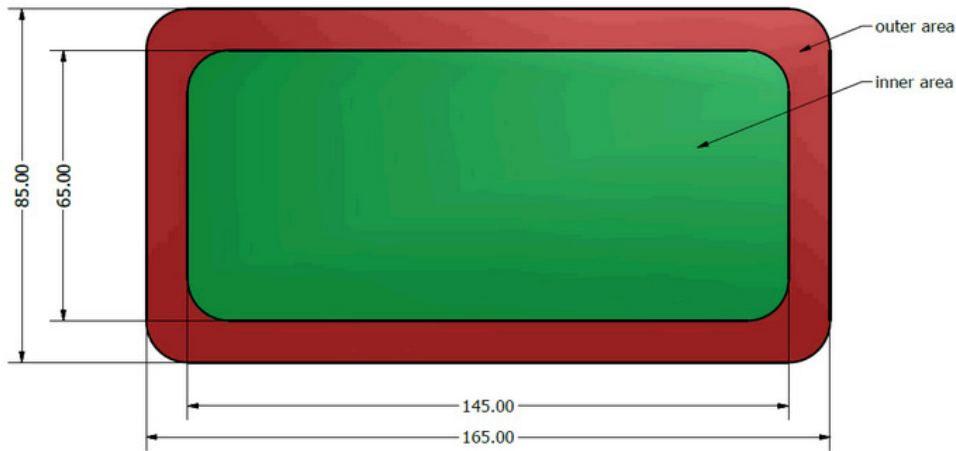


Figure 4.1: Front view of the AEI 10 m prototype beam splitter showing the different areas for polishing requirements. Green shows the inner area with a required surface flatness of  $\lambda/20$  and red the outer area with a surface flatness requirement of  $\lambda/5$ .

Another important surface quality parameter is the scratch-dig value. It describes the maximum amount and size of scratches and digs allowed on the substrate after the polishing process. The scratch-dig value is a military performance standard [Edm22] consisting of the two numbers X-Y.

## CHAPTER 4. BEAM SPLITTER FOR THE SUB-SQL INTERFEROMETER

The X value is directly related to the scratches and is called the scratch number. It describes the brightness of a scratch observed with a dark field microscope. It has a standardized illumination and consists of the defined values 80, 60, 40, 20, 10 and 5. The length of all scratches with the defined scratch number may not exceed a quarter of the optic's diameter. Further, the sum of the product of all scratch numbers smaller than X multiplied by their total number and divided by the optic's diameter has to be below or equal to X/2 if a scratch of the size X is present on the optic. If no scratch of the size X is present, the sum has to be below or equal to X.

The Y value is also called the dig number. It describes the maximum diameter of digs allowed on the optic in units of 10  $\mu\text{m}$ . The diameter of a non-symmetric dig is the average of a dig's width and height. The total number of maximum-sized digs (N) is a twentieth of the optic's diameter in units of mm. The total sum of the diameter of all digs above a size of 2.5  $\mu\text{m}$  may not exceed two times the product of Y and N.

Feature	Substrate 1	Substrate 2	Unit
Lenght	16.48	16.48	cm
Height	8.50	8.50	cm
Thickness	4.88	4.88	cm
Wedge	0.997	1.016	deg
Round edge radius	1.01	1.01	cm
Bevels	0.40-0.45	0.58-0.68	mm
Clear aperture	65 $\times$ 145	65 $\times$ 145	mm <sup>2</sup>
Surface flatness green	$\leq \lambda/20$	$\leq \lambda/20$	PV
Surface flatness red	$\leq \lambda/5$	$\leq \lambda/5$	PV
Surface quality	$\leq 10-5$	$\leq 10-5$	scratch-dig

Table 4.1: Table showing the dimensions and surface quality parameter after the polishing process measured by Coastline Optics.

The scratch-dig value for the AEI 10 m prototype beam splitter was defined as 10-5. The final dimensions of the beam splitter substrates and the achieved polishing parameters can be seen in table 4.1.1.

**50/50 coating**

The 50/50 coating is the core part of the beam splitter. It is the position within the interferometer where the laser beams for the two arms are separated and later combined. The accuracy of the coating's splitting ratio determines the power ratio between the two arm cavities.

As the light inside the cavities is causing radiation pressure on the suspended mirrors, a varying laser power leads to a varying position of the suspended mirrors. This is changing the cavity length. Hence, the laser power variation couples into the differential readout of the interferometer. This effect is called radiation pressure noise. If the laser power change is common in both arms, the cavity length change will be the same for both arm cavities. Thus, the radiation pressure noise will be suppressed.

The power inside the interferometer arms is defined by the finesse of their cavities and the power of the laser beam entering the cavity. The finesse difference of the arm cavities is assumed to be small. Thus, it is important to have an exact 50-50 splitting ratio for the reflected and transmitted beam. To compensate for the wedge angle of 1 deg while maintaining a 90 deg angle in between the two arms, the angle of incidence onto the beam splitter is 44.6 deg. Figure 4.2 shows the measured

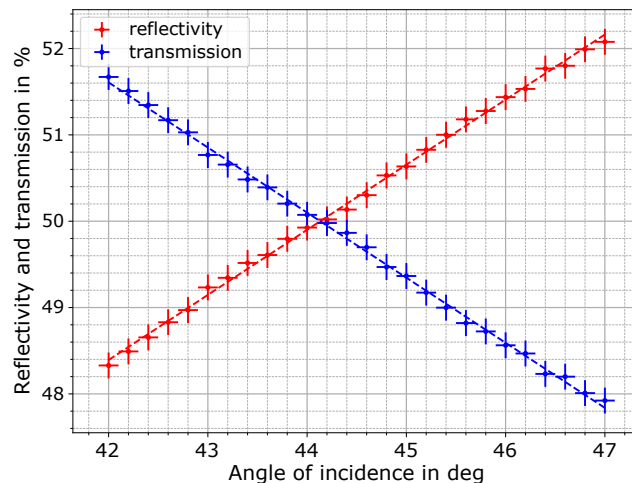


Figure 4.2: Reflectivity and transmission measurement of the 50/50 coating of the AEI 10 m prototype beam splitter. The 50-50-crossing could be calculated to 44.45 deg.

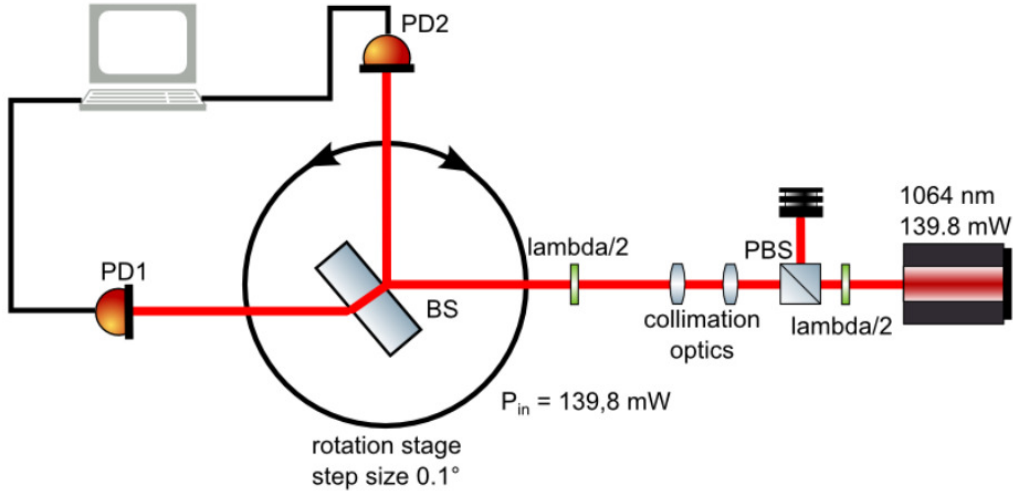


Figure 4.3: Measurement set-up for the splitting ratio measurement of the beam splitter. To minimize the error of the photodiodes PD1 and PD2, two consecutive measurements with swapped photodiodes have been taken.

reflectivity and transmission of the beam splitter.

As can be seen in figure 4.2, the reflectivity and transmission have a linear dependence on the angle of incidence and cross 50% at a certain angle. This angle was specified to  $44.6 \pm 0.5$  deg. The requirement of  $\pm 0.5$  deg is set by space constraints on the south and west table. This is due to an angle differing from 44.6 deg, leading to a slight change of the 90 deg angle in between the two arms and thus requiring the end test mass suspensions to be pushed towards the edge of the optical tables.

The measurement set-up shown in figure 4.3 was used to measure the transmission and reflectivity shown in figure 4.2. A 1064 nm NPRO laser provides 140 mW of input power. The laser beam is s-polarized and collimated by two lenses. The beam splitter is placed on a rotation stage and horizontally rotated around the laser spot on the front coating. The transmission and reflection are measured with photodiode power sensors from Thorlabs. To reduce the calibration error of the photodiodes (up to 5 %), two consecutive measurements with swapped photodiodes were made. The measured transmission ( $T$ ) and reflectivity ( $R$ ) could be calculated using

$$T = \frac{\frac{T_1+T_2}{2}}{\frac{T_1+T_2}{2} + \frac{R_1+R_2}{2}} \quad (4.1)$$

and

$$R = \frac{\frac{R_1+R_2}{2}}{\frac{T_1+T_2}{2} + \frac{R_1+R_2}{2}}, \quad (4.2)$$

where  $R_1$  is the reflectivity measured with PD1,  $R_2$  is the reflectivity measured with PD2,  $T_1$  is the transmission measured with PD1 and  $T_2$  is the transmission measured with PD2. The remaining error of the measurement was 1% due to fluctuating laser power. The 50-50-crossing angle of the beam splitter coating was calculated to be 44.45 deg. Adapting the sub-SQL interferometers layout to the crossing requires one of the arm cavity mirrors to be shifted by 26 mm. This is well within the expectations.

### AR coating

According to the Fresnel equations, each boundary in between two media with different refractive indices reflects a portion of an incident light field. The amount is dependent on the polarization and the angle of incidence of the light field, as well as the refractive indices of both media. The boundary between fused silica and air or vacuum usually reflects about 4% of an incident light field with a wavelength of 1064 nm at normal incidence. To reduce the amount of light reflected at boundaries where no reflection is desired, an anti-reflective coating is applied.

An AR coating for a specific wavelength is usually composed of two different layers forming three optical boundaries, including the substrate. Each of them reflects a part of the incident light field. The thickness of the two layers is designed to destructively interfere the three reflected light fields at a certain angle of incidence. The amplitude of each reflected light field is defined by the Fresnel equation for the corresponding optical boundary and angle of incidence. The phase relation between the different reflected light fields is defined by the thickness and thus the optical path length through the coating layers.

## CHAPTER 4. BEAM SPLITTER FOR THE SUB-SQL INTERFEROMETER

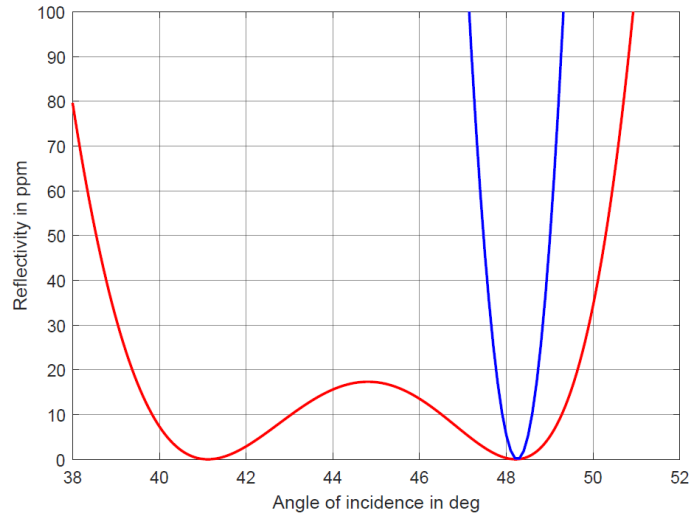


Figure 4.4: Reflectivity as a function of the angle of incidence for the beam splitter’s six layer AR coating design (red). In blue, a two layer AR coating is shown, optimized for only one of the required angles of incidence.

To design an AR coating with a minimal reflectivity at more than one angle of incidence, more than two coating layers are required. Though a two-layer AR coating is preferred in many single wavelength applications, it only provides a ppm-level reflection minimum for a single angle of incidence (see figure 4.4). Due to the different angles of incidence which are required for the beam splitter (see section 4.1.2), the design of a six-layer AR coating is required. The design of the six-layer AR coating was done using the multidiel code [Orf22] for Matlab. The resulting reflectivity as a function of the angle of incidence can be seen in figure 4.4 in comparison with a two-layer AR coating.

The reflectivity of AR coatings strongly depends on the accurate thickness of the individual layers. Thus, small thickness offsets occurring during the manufacturing process will lead to increased reflectivities compared to the design. Due to the increased number of layers, the six-layer AR coating is more susceptible to thickness offsets arising during the deposition of each layer. To test the six-layer AR coating, a batch of small optics was ordered from the coating manufacturer Laseroptik GmbH. After confirming the performance of the six-layer AR coating, the beam splitter was coated. Figure 4.5 shows the reflectivity of the test samples’ AR coating as a function of the angle of incidence.

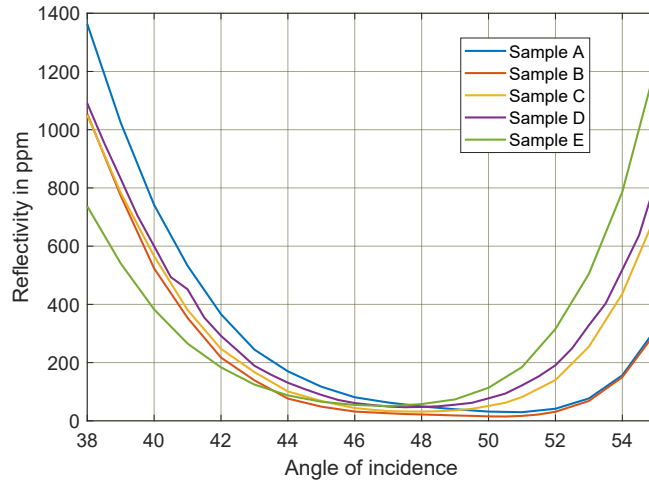


Figure 4.5: Measured reflectivity of the test samples' AR coating, as a function of the angle of incidence.

As most coating manufacturers are unwilling to promise reflectivities of below 0.1 % for AR coatings, a best-effort order had to be placed. In comparison with the previous reflectivity tests on the sample mirrors, the AR coating of the beam splitter turned out to be worse, as can be seen in the split coating measurements in section 4.1.2. In the sub-SQL interferometer, the reflections of the AR coating of the beam splitter will be constantly measured and used as references. As described in the following subsection, the beam splitter design foresees that only beams, which have been reflected at least twice from an AR coating, may be uncontrolled. Thus, the combined reflectivity of the two reflections from the six-layer AR coating is well below the 0.1 ppm-level.

### 4.1.2 Shape constraints

The shape and design of the beam splitter substrate require considerations about the size and weight constraints of the experiment and about beam paths of reflections from the AR coating. As explained in section 1.3, the sub-SQL interferometer is built on seismic attenuation systems. These are constrained to a maximum payload, requiring reducing the mass of individual components where possible. Hence, during the beam splitter's shape design, its mass is considered an important parameter.

The main reason for the beam splitter's size exceeding the size of the other

## CHAPTER 4. BEAM SPLITTER FOR THE SUB-SQL INTERFEROMETER

core optics is the problem arising from internal reflections. The beam splitter is transmitting 50 % of the incident laser power while being hit under an angle of incidence differing from 0 deg. This leads to the possibility of reflections from the rear surface overlapping and thus interfering with the beam paths towards the interferometer arms. As the laser beam is partially reflected from the rear surface, it is directed back through the optic towards the frontal 50-50 coating. At the front coating, it is split, leading to one beam path outside the beam splitter and one within. The arising internal reflections, apart from the main beam path, are called ghost beams and can cause problems whenever exiting the substrate. It needs to be ensured that all exiting beams with power above a defined threshold need to be steered towards a beam dump or PD without clipping at any optic.

A common approach to the separation of the exiting ghost beams from the main beam path is to increase the substrate's thickness and implement a wedge angle. By increasing the substrate's thickness at a typical angle of incidence of around 45 deg, the exiting ghost beam can be fully separated from the main beam. Dependent on the incident beam's spot size on the beam splitter, the required thickness to separate both beams can become relatively large, increasing the mass of the substrate significantly. To enhance the beam separation, a wedge angle can be applied to the rear surface. The wedge angle is the angle between the front and rear surface. The wedge angle needs to be designed in a way to prevent the ghost beams from clipping at other optics while being able to be picked off at some point in the experiment with a beam dump or PD.

For the beam splitter substrate of the sub-SQL interferometer of the AEI 10 m prototype, a wedge angle of 1 deg at a central thickness of 4.88 mm was chosen. The required width to avoid clipping at the substrate's edges is about 165 mm. With a height of 85 mm, a total mass of 1.5 kg could be achieved. This design prevents beam overlap within three times the beam radius of the incident beam and twice the beam radius for exiting ghost beams after reflecting from the AR coating.

As a threshold for the tracking of ghost beams, a double reflection from an AR coating was set. Each reflection at an AR coating reduces the laser power to around 100 ppm (see section 4.1.1). After being reflected twice from such an AR coating, the power is reduced to around 0.01 ppm of its original power and can be dumped using an enclosure around the beam splitter optic.

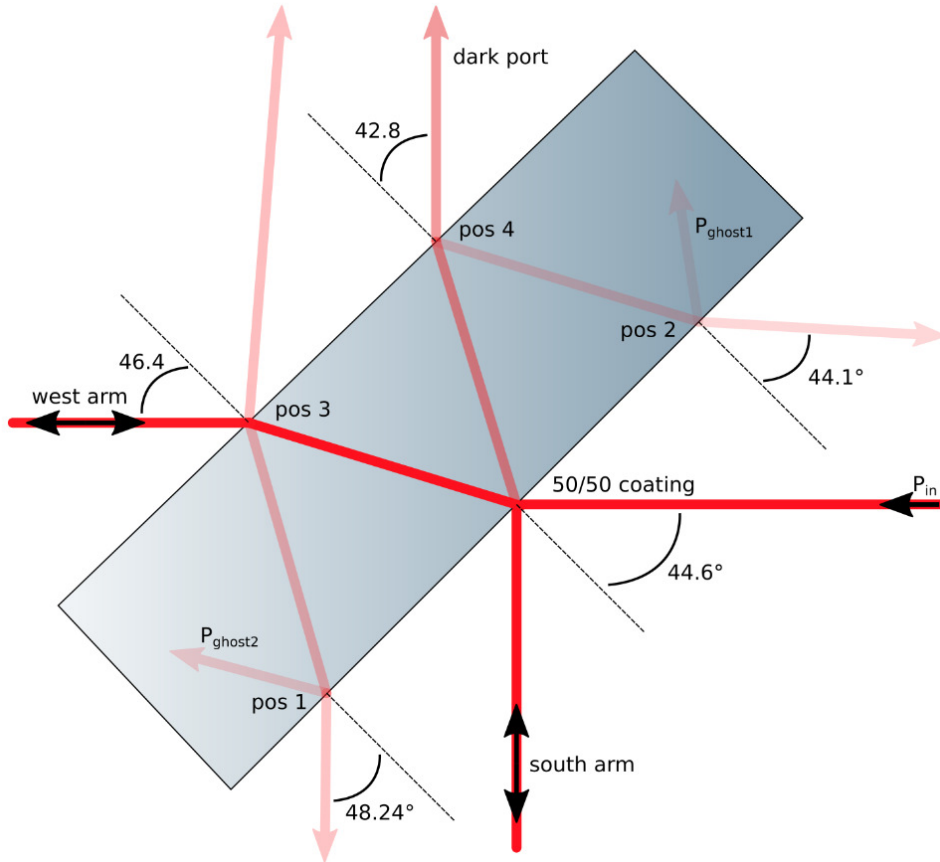


Figure 4.6: Beam path of main beam and ghost beams through the sub-SQL interferometer’s beam splitter.

To reduce the width required for the beam splitter, a split coating design was used at the front surface. The deposition of a split front coating, consisting of the 50-50 beam splitter coating in the central area and an AR coating towards the outer region, reduces the internal reflections by one before being reflected twice by an AR coating. A schematic including the sub-SQL interferometer’s beam splitter design parameters and the beam path for the split coating design can be seen in figure 4.6.

The split coating was deposited by Laseroptik GmbH in two separate coating runs. Metal sheets were installed close to the optic to cover areas that should not be coated during the respective coating run. An undefined transition area in between the two different coatings with a width of 1 mm was accounted for during the beam path design. A reflectivity scan highlighting the 50-50 coatings reflectivity can be seen in figure 4.7, while a reflectivity scan highlighting the AR coatings reflectivity

## CHAPTER 4. BEAM SPLITTER FOR THE SUB-SQL INTERFEROMETER

is shown in figure 4.8. The data of both scans are from the same measurement at an angle of incidence of 44.6 deg, only differing in the resolution of the color bar.

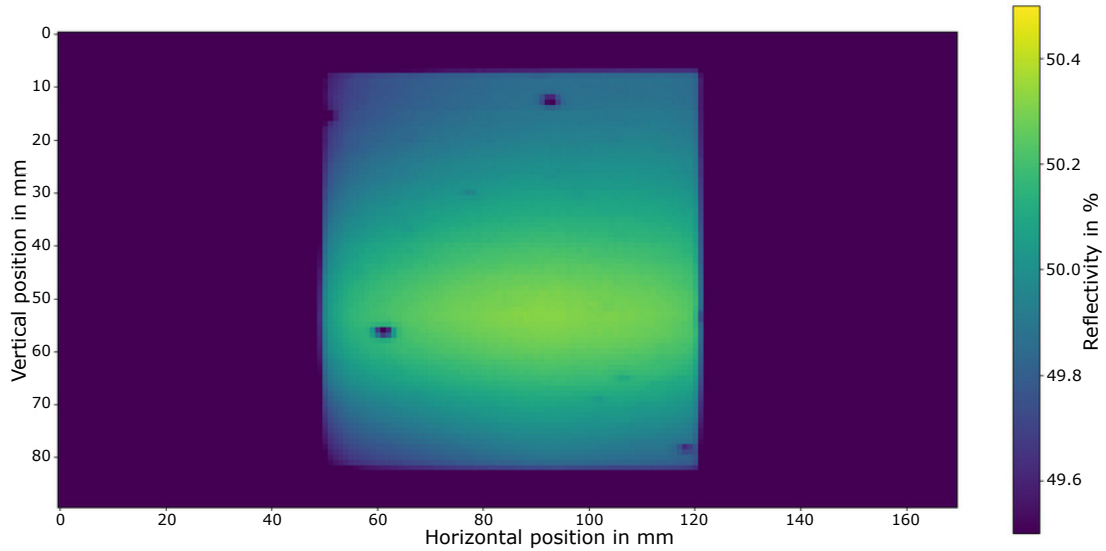


Figure 4.7: Reflectivity scan of the front surface of the BS for the sub-SQL interferometer. The scaling of the z-axis, focusing on the 50-50 coating.

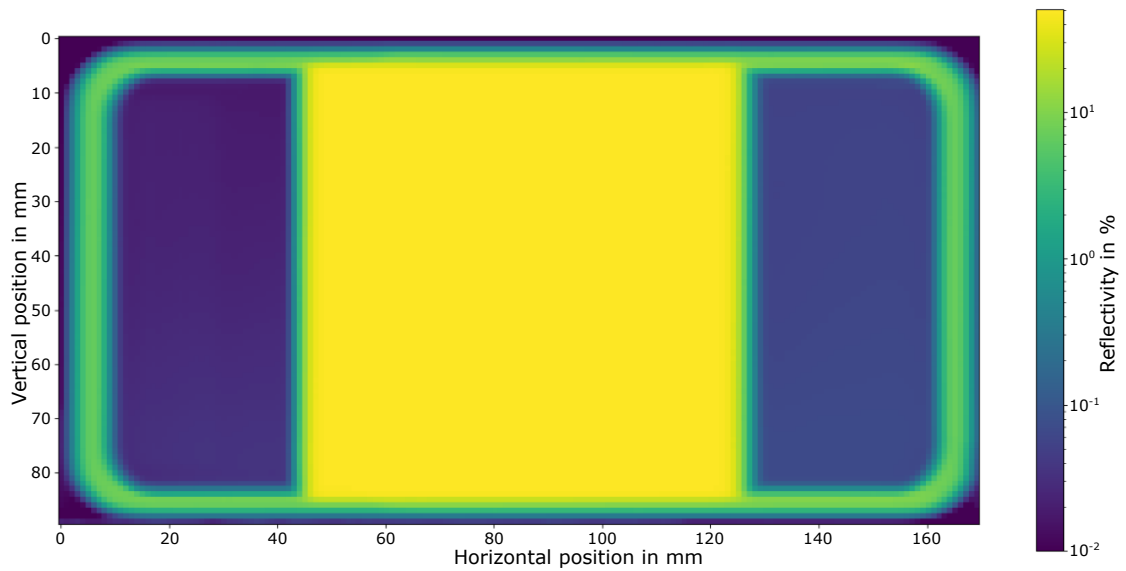


Figure 4.8: Reflectivity scan of the front surface of the BS for the sub-SQL interferometer. The scaling of the z-axis, focusing on both, the AR coating.

Figures 4.7 and 4.8 show well-separated coatings with a sharp reflectivity transition. This shows that such a split coating can be feasible to reduce the width of the substrate by reducing the power inside the secondary ghost beam.

## 4.2 Triple suspension design

In section 1.2.2 and 1.3.2, the necessity of seismic isolation is described. Further, the seismic pre-isolation via the seismic attenuation system (SAS) is described. While the SAS provides seismic isolation at frequencies above 0.2 Hz, further isolation is required to reduce the motion of the arm cavity optics down to an amplitude of  $10^{-19} \text{ m}/\sqrt{Hz}$  within the measurement band. To achieve such a low mirror motion, triple suspensions are used. These are three suspension stages cascaded together into one suspension.

The beam splitter's suspension requires slightly less seismic isolation compared to the interferometer's cavity mirrors. Their movement directly changes the length of the interferometer arms and is amplified by the cavity's finesse. This couples into the output port of the interferometer, as described in section 1.1.2. Though the motion of the beam splitter is changing the arm length difference as well, the arm length change is not amplified by a cavity. This results in a lesser influence on the beam splitter's motion compared to the cavity mirrors.

The motion requirements for the BS can be estimated to an amplitude of roughly  $10^{-17} \text{ m}/\sqrt{Hz}$  in the measurement band of the sub-SQL interferometer. This can be derived by using the suspension requirements for the cavity mirrors of  $10^{-19} \text{ m}/\sqrt{Hz}$  above 40 Hz as a basis. As an approximation, the motion requirement of the cavity mirrors can be multiplied with the amplification effect of the finesse in the arm cavities, as would be seen in the output port of the interferometer. The resulting requirement of a motion amplitude of  $10^{-17} \text{ m}/\sqrt{Hz}$  would barely allow the design of a two-stage suspension. Nonetheless, it was decided to design a three-stage suspension. This adds a safety margin in terms of the suspension performance. Further, an additional stage in between the position sensors and actuators at the first suspension stage (see section 4.2.4) will reduce the actuator and sensor noise coupling to the suspended BS.

In this section, a short introduction to the working principle of a suspension will

be given in 4.2.1. An overview of the different degrees of freedoms of the suspensions, including cross-coupling mechanisms, will be shown in 4.2.2. Section 4.2.3 describes the various suspension parameters, defining the suspension properties and allowing the creation of a state-space model to simulate the suspension performance. To control the suspension motion at low frequencies and to damp the suspension resonances, active control loops will be implemented (see 4.2.4). The final design of the beam splitter suspension can be seen in 4.2.5. Its performance is evaluated and discussed in section 4.2.6 and 4.2.7.

### 4.2.1 Suspensions as harmonic oscillators

The case of an external force actuating on a damped harmonic oscillator (HO) can be used to describe the seismic isolation effect of a suspension [Wes16]. Here, the term suspension relates to the basic principle of a pendulum, a mass suspended by a wire. It is commonly known that a pendulum with a small displacement compared to its length, as well as a massless wire, can be described as an HO. In the case of a suspension used for seismic isolation, the displacement of the suspended mass is far below the length of the suspension wires. Further, the mass of the suspension wire is small compared to the suspended mass. With the addition of more degrees of freedom (see section 4.2.2), the modeling of a suspension will become more complex, requiring computer models (see section 4.2.3) to solve them.

Moving the suspension point of a pendulum can be seen as the implementation of an external displacement to the HO equation. The response of the pendulum's mass to a varying displacement is dependent on the displacement's amplitude and frequency. Below the resonance frequency, which is defined by the pendulum length and the gravitational constant  $g$ , the amplitude of the response of the pendulum mass equals the amplitude of the external displacement. At the resonance frequency, the response's amplitude is enhanced compared to the external displacement. When the frequency of the external displacement surpasses the resonance frequency, the corresponding amplitude of the mass response decreases with  $1/f^2$ . This can be used to reduce the motion of a suspended mass relative to its suspension point above the resonance frequency.

For gravitational wave detectors, a single suspension stage, providing a motion

reduction with a  $1/f^2$  frequency dependence, is not sufficient. To suppress seismic noise within a gravitational wave detector's detection band, the ground motion needs to be suppressed by more than nine orders of magnitude above 10 Hz. This can be seen by comparing the ground motion with the seismic displacement noise of the detectors. [Abb+02; Bui+20]. Such a seismic noise suppression would require a single suspension with a resonance frequency of below 0.1 mHz, corresponding to a length of the suspension wires of more than 1600 km. As this is practically impossible, multistage suspensions are used to achieve the desired seismic noise suppression.

Multistage suspensions are two or more suspension stages (masses) suspended from each other, creating what could be described as cascaded HOs. Here, each additional suspension stage multiplies the motion of the final suspension stage with another  $1/f^2$  compared to the displacement of the suspension top above the resonance frequencies. The sub-SQL interferometer of the AEI 10 m prototype uses triple suspensions, reducing the motion of its core optics with a slope of  $1/f^6$  compared to the motion of the suspension cages.

Similar to suspended masses acting as a pendulum, vertical movement can be suppressed by the usage of cantilevers. These are blade springs deflected by a mass suspended at its tip. At the resting point, the gravitational force pulling onto the suspended mass is in equilibrium with the restoring force of the deflected blade spring. A vertical displacement in either direction from the resting point leads to a force acting in the opposite direction, forming a vertical HO.

### 4.2.2 Degrees of freedom and cross coupling

Up to now, only the case of a suspension moving along one degree of freedom (DOF), e.g., along the interferometer arm, was covered. In reality, the complete motion of a suspended object can be separated into motions in six different degrees of freedom (DOFs). These DOFs are longitudinal, side, vertical, pitch, yaw and roll. They are depicted in figure 4.9 and can be summarized as three transversal and three rotational DOFs.

To fully describe the seismic isolation of a suspension, the displacement of the suspension top and its effect on the motion of the suspended mass needs to be

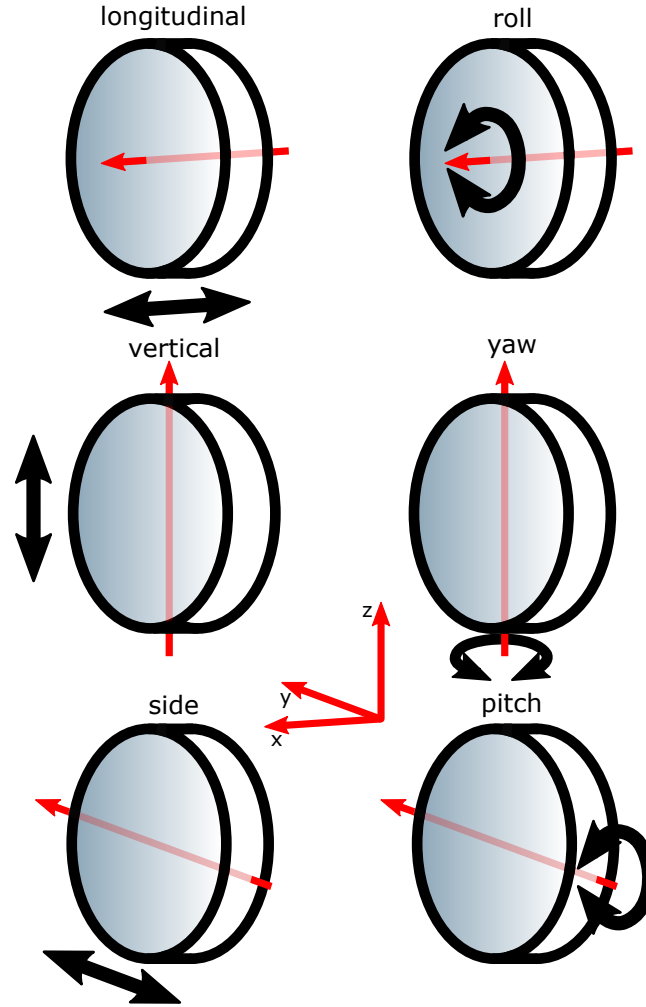


Figure 4.9: Depiction of all six DOFs. In red, the coordinate axes through the center of mass (CM) of the suspended masses are shown. On the left-hand side, the transversal DOFs along the coordinate axes can be seen. The rotational DOFs around the corresponding coordinate axes are shown on the right-hand side.

calculated for every DOF. Each DOF possesses its own motion response and thus set of resonance frequencies. Further, the motion in one DOF often leads to a motion in another. This is called cross-coupling.

Dependent on the suspension design and manufacturing, cross-coupling can arise in between any of the DOFs. Though every DOF may couple into another, there is a fundamental cross-coupling in between some of them. Firstly, a strong cross-coupling can be observed from the longitudinal DOF to the pitch DOF. This is caused by the suspended mass swinging along a circular path with the suspension's wire length as

a radius. A longitudinal motion will automatically induce a pitch angle and thus couple into the pitch DOF. The same process can be observed by the suspension swinging sideways, which rolls the suspended mass, leading to a strong cross-coupling from the side DOF to the roll DOF.

The especially strong cross-coupling from the longitudinal and the pitch DOF, as well as the side and the roll DOF, leads to a change in the motion response of the suspended mass in these DOFs. For example, the resonance frequencies of the pitch DOF are clearly visible in the longitudinal motion response of the suspended mass for a longitudinal displacement of the suspension top. This results in six resonances in the motion response of each of the four DOFs.

The resonance frequencies in each of the DOFs can be adjusted by the design choice of certain parameters, which are described in the following section.

### 4.2.3 Suspension simulations and parameters

State-space modeling was used to simulate the performance of the triple suspension. In the state-space model for a triple suspension, the HOs for each DOF and their cross-coupling are described by differential equations. These are noted down in matrix form, using state vectors. Each state vector contains state variables, describing the state of their corresponding system over time. Knowing the state-space matrices allows calculating output state variables from a set of input state variables at a certain time over a desired time span. To create the state-space model of a system, it needs to be linear and time-invariant [Wes16]. These requirements are fulfilled for suspensions with small displacements.

The state-space matrices depend on and are calculated with a variety of suspension design parameters. When designing a suspension, these parameters can be used to change resonance frequencies and the overall response of the suspension system. Here, the state-space models were calculated from the design parameters using the Matlab software. An already existing Matlab code by Bob Taylor was adjusted, and its Simulink model (block diagram environment in Matlab [Mat22]) was used to calculate the motion response of the different suspension stages in the frequency and time domain.

To create a working and stable suspension design, a set of design parameters had

## CHAPTER 4. BEAM SPLITTER FOR THE SUB-SQL INTERFEROMETER

to be found. During the design phase, the Simulink model helped to evaluate the stability and ring-down time of the damped and non-damped suspension. It provided information on which suspension resonances in any DOF required tuning. Here, certain parameters could be changed to only affect certain DOFs. As a triple-stage suspension is designed, each DOF possesses three resonance frequencies.

The resonance frequencies in the vertical DOFs were defined by the deflection of the blade springs. The design and simulation of the blade springs can be found in the appendix in A. Further, the thickness and length of the final wire, as well as the final suspended mass, define the third vertical resonance for a suspension system with two blade spring stages.

The longitudinal and side DOF resonance frequencies can be primarily tuned via the wire length in between the individual suspension stages. The total, summed wire length defines the first resonance frequency, while the second and third resonances depend on the wire lengths, separating the suspension stages.

Each rotational degree of freedom is strongly influenced by the moment of inertia around the corresponding rotation axis, as depicted in 4.9. Further, two of them can be tuned by the separation of their wire break-off points. The pitch DOF is influenced by the vertical separation and separation along the x-axis (see 4.9) of the wire break-off point towards the previous and subsequent suspension stage. The yaw DOF is influenced by the separation of the wire attachment points along the y-axis (see 4.9). Finally, the roll DOF is primarily dependent on the resonance frequencies of the spring blades, as well as their y-separation.

The Simulink model further allows for the implementation of feedback loops. Reading out the output state values of the uppermost suspension stage, they can be fed back and subtracted from the input state values. This simulates the use of force actuators, acting at the first suspension stage. This is called active damping.

### 4.2.4 Active damping and control

To actively damp a suspension, actuators and sensors are required. Active damping is the extraction of energy from the suspension system. This can be achieved by reading out the suspension motion of one or more suspension stages and using the gained information to apply a counteracting force onto the corresponding

## CHAPTER 4. BEAM SPLITTER FOR THE SUB-SQL INTERFEROMETER

suspension stage. As most of the energy of a free-swinging suspension is gathered at the resonance frequencies, active damping is primarily used to dampen these. Therefore, shadow sensors are used to contactlessly read out the motion of the first suspension stage. Then, coil actuators are used to apply a controlled, counteracting force.

In the AEI 10 m prototype, BOSEMs [Car+12] are used at the beam splitter suspension, combining shadow sensor and coil actuator in one device. A schematic cross-section of a BOSEM can be seen in figure 4.10. An aluminum flag, glued to a magnet, is attached to a suspended mass. The flag and a part of the magnet are surrounded by the BOSEM. Inside the BOSEM, a light-emitting diode (LED) is collimated towards a PD. The light is then partially blocked by the flag, reaching into the BOSEM. Depending on the amount of light blocked by the flag, a position depending current can be read out from the PD. By applying a current to the coil at the BOSEM tip, the strength of the resulting magnetic field can be controlled. The magnetic field pushes onto the magnet, which is partially surrounded by the coil.

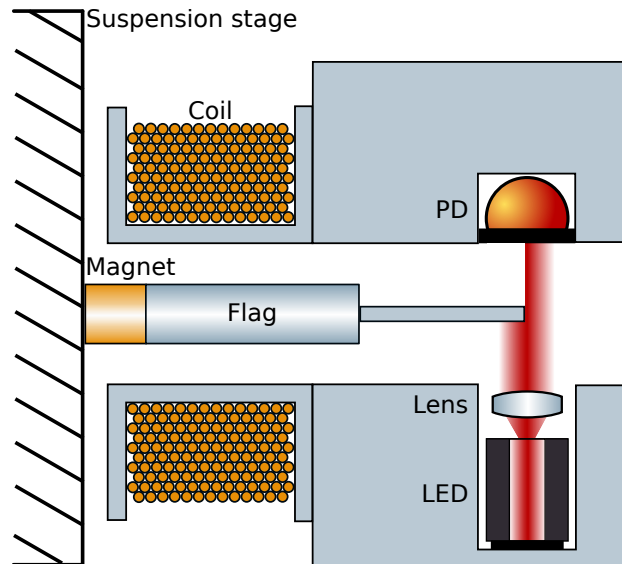


Figure 4.10: Schematic cross-section of a BOSEM acting as shadow sensor and coil actuator. An aluminum flag is glued to a magnet, which is attached to a suspended mass. The flag and a part of the magnet are surrounded by the BOSEM. An LED is collimated onto a PD by a lens. The flag position along the BOSEM axis can be read out by the amount of light it covers. The coil can be used to actuate on the magnet.

## CHAPTER 4. BEAM SPLITTER FOR THE SUB-SQL INTERFEROMETER

The BOSEMs used for the active damping at the first suspension stage of the BS suspension is a modified version compared to the design described in [Car+12]. As the BS optic has a higher mass compared to, e.g., the suspended optics of the frequency reference cavity (see chapter 1.3.3), a stronger actuator is required. The maximum current through the thin coil wires is limited by the arising heat in a thermally low conductive vacuum environment. This results in a higher coil winding number with an increased wire diameter to allow higher current at similar operating temperatures. Both the increased current and the increased coil windings increase the magnetic field strength. This allows a higher maximal actuation force.

Applying a DC voltage to the coil actuators of the BOSEMs allows aligning the BS optic at the end of the suspension chain. As BOSEMs are installed to cover all DOFs, they can be used to fine-tune and thus align the first suspension stage's position and orientation. For frequencies below the resonances, the position and orientation change of the third suspension stage is closely coupled to the changes of the first suspension stage. This leads to very fine alignment possibilities within a limited range.

### 4.2.5 Suspension design

The design goal of the BS suspension is a robust, easily accessible triple-stage suspension. Further, it requires active damping at its first suspension stage, as well as the possibility to implement additional coil actuators at the second stage. As a wide variety of suspension parameters could be chosen, some initial parameters are taken from existing suspensions. This reduces the possible parameters, giving a starting point for the design. It also provides the benefits of similar resonance frequencies in some DOFs, enabling the design of similar feedback loops.

Starting from the existing suspension design of the frequency reference cavity (RC) mirrors of the AEI 10 m prototype [Wes16] (see 1.3.3), the beam splitter's suspension design could be developed. One of the first design parameters to choose from is the wire length in between the suspension stages and thus the total suspension length. These were adapted from the RC suspension, leading to nearly identical resonance frequencies in the longitudinal and side DOF. Further, deductions from the handling of the existing suspensions could be made, improving, e.g., the alignment

possibilities of the BOSEM actuators.

The mechanical properties of the BS optic could be used to define further suspension parameters. Here, e.g., the mass and moments of inertia are already defined. From there on, the mechanical parameters could be taken after designing the individual stages from bottom to top. Final adjustments were made with the Simulink model described in section 4.2.3 by changing the wire separations along the different axes.

An overview of all suspension parameters for the BS triple suspension can be seen in table 4.3 at the end of this chapter. The positions of the various parameters are visualized in the following figure, showing a schematic of the BS triple suspension.

### Third suspension stage

The mechanical properties of the third suspension stage, such as mass, moments of inertia and the y-separation of the wire break-off points, could be taken from the BS optic's CAD model. Its design is described in section 4.1.2 and shown in figure 4.11.

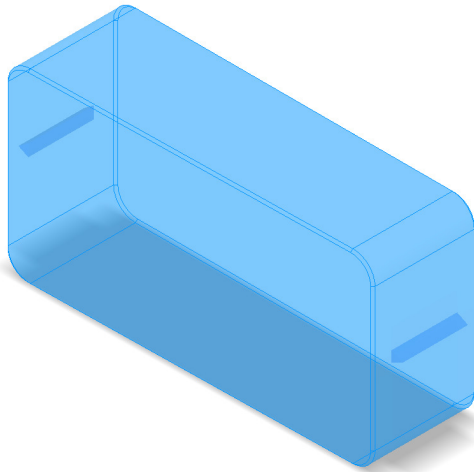


Figure 4.11: CAD picture of the BS optic made from high grade fused silica, including the triangular prisms for the wire slings. Mass of 1.48 kg, at a width of 165 mm, a height of 85 mm and a central thickness of 48.8 mm with a wedge angle of 1 deg.

Wire slings were used to attach the suspension wires to the BS optic to increase the Q-factors of the resonances and the violin modes in the lowest suspension stage.

## CHAPTER 4. BEAM SPLITTER FOR THE SUB-SQL INTERFEROMETER

This decreases the thermal suspension noise [BBM02] (see chapter 1.2.4). Here, two triangular fused silica prisms were glued to the optic's side surfaces. Each of them has a height of 5 mm and is used to guide the wires upwards. These prisms alongside the BS substrate define the y-axis wire separation. The x-separation of the wires at the BS optic can be used to tune the resonance frequencies in the pitch DOF. A smaller x-separation usually corresponds to lower pitch resonances. The z-separation is the distance from the wire break-off point to the center of mass (CM) of the BS optic. Its position is defined by the tip of the fused silica prisms. Changing the z-separation of the wire break-off point has a small influence on the frequency of the pitch resonances.

### Second suspension stage

The mechanical properties of the intermediate and second suspension stage are kept close to the mechanical properties of the third suspension stage. The second suspended mass is made from aluminum, with similar dimensions as the BS optic. This allows a purely vertical orientation of the lower suspension wires, leading from the second to the third suspension stage. The second stage of the suspension can be seen in figure 4.12.

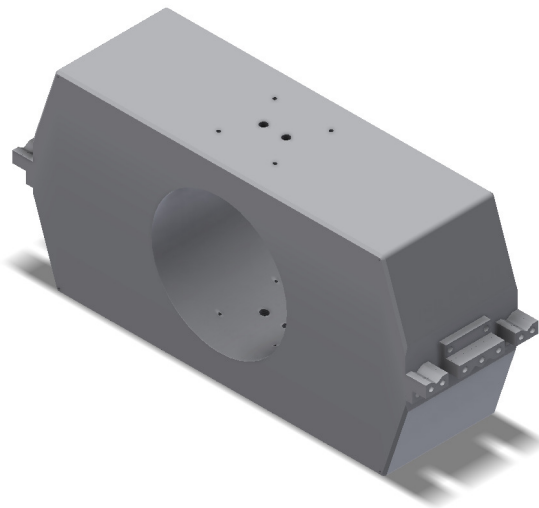


Figure 4.12: CAD picture of the intermediate, second suspension stage, including clamps for suspension wires towards the first and third suspension stage. Made from aluminum with a mass of 1.42 kg, a width of 165 mm, a height of 85 mm and a central thickness of 50 mm.

## CHAPTER 4. BEAM SPLITTER FOR THE SUB-SQL INTERFEROMETER

The wires at the second suspension stage were attached using aluminum clamps. This results in fixed wire positions, allowing an easier assembling process. The y-separation for both the lower and mid wire are defined by the width of the second suspension stage. The x-separation of the wires towards the first suspension stage is kept identical. The z-separation of the lower and mid wire from the CM of the second stage is used to tune the pitch resonances of the suspension.

### First suspension stage

The first suspension stage is equipped with four blade springs, acting as the second vertical isolation stage to achieve two vertical isolation stages for the BS suspension. The design of the blade springs can be seen in the appendix A. It defines the vertical resonance frequencies and has a strong influence on the pitch, as well as the first two roll resonance frequencies. Four blade springs were chosen over two to reduce the coupling from twisting blade springs into pitch motion. Thus, each suspension wire is attached at the central tip position of a blade spring.

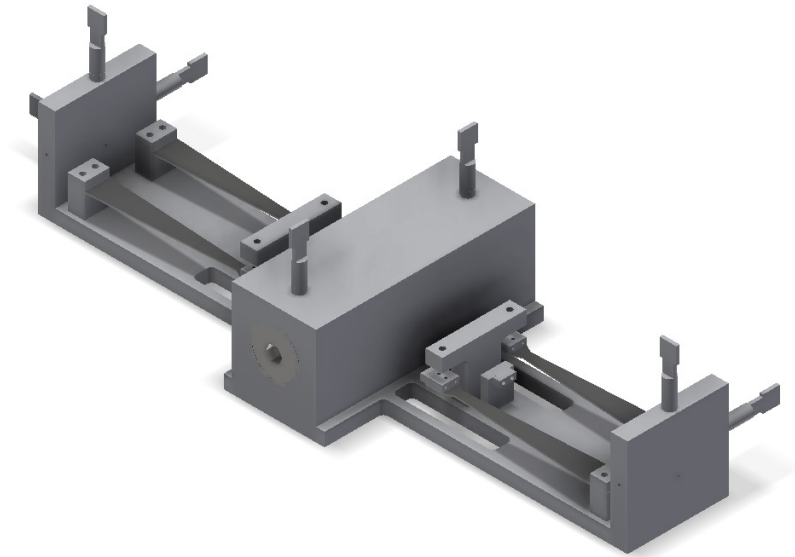


Figure 4.13: CAD picture of the top, first suspension stage, including clamps for suspension wires towards the suspension cage and the second suspension stage. Made from aluminum with a mass of 2 kg, a width of 350 mm, a height of 58 mm and a central thickness of 130 mm. A threaded stainless steel rod in the center allows shifting the CM alongside the x-axis (axis definition, see 4.9).

## CHAPTER 4. BEAM SPLITTER FOR THE SUB-SQL INTERFEROMETER

The first suspension stage required a wider design to carry a set of four blade springs while achieving the desired wire separations. Further, the sensitivity of the BOSEMs installed at the first suspension stage (see section 4.2.4) benefits from big lever arms. These two major points lead to a puppet-cross-like design. It is made from aluminum with a threaded stainless steel rod at its center. The threaded rod allows for shifting of the first suspension stage's CM along the x-axis to adjust the pitch angle of all suspension stages.

The y-separation of the upper and mid wires is used to tune the roll resonance frequencies. Only two wires alongside the y-axis are used towards the suspension top to reduce the coupling of the pitch motion of the ground to the suspension. Further, this reduces changes in the pitch DOF caused by differential drifts of the relatively soft upper blade springs. The z-separation of the upper and mid wire to the stage's CM is used to tune the pitch resonance frequencies.

### **Suspension cage**

The suspension cage, as shown in figure 4.14, needs to provide enough space to house the triple suspension, lifting the center of the BS optic to a height of 22 cm. The suspension stage top includes two blade springs to carry the mass of all three suspension stages. Partially hollow, 30 mm x 30 mm aluminum profiles were used for the suspension cage to reduce the overall weight. The movement of each suspension cage is limited by catchers, which can catch the respective suspension stage in case of a failing suspension wire.

To reduce the internal resonance frequencies of the suspension cage, additional cross-shaped stiffening structures are installed. These are omitted in figure 4.14 to provide better visibility of the individual suspension stages. The suspension cage has a total height of 1 m at a mass of 17 kg, including the three suspension stages.



Figure 4.14: CAD picture of BS triple suspension. Suspension cage made from 30 mm x 30 mm aluminum profiles. The top carries two blade springs, forming the first vertical suspension stage. The BOSEMs are attached to the suspension cage, measuring and actuating the motion of the first suspension stage.

### 4.2.6 Measured resonance frequencies

This section provides a comparison of the simulated (see section 4.2.3) and the measured resonance frequencies. The coil actuators were used to apply a random force to the first suspension stage to measure the resonance frequencies. The shadow sensors were used to measure its motion response, allowing identification of the resonance frequencies. Table 4.2.6 compares the simulated and measured values for all DOF. Some higher frequency resonances could not be measured, as the set-up's noise floor covered them. The measurement took place on a non-seismically isolated optical table outside the vacuum system.

DOF	Simulation in Hz	Measurement in Hz
long 1	0.64	0.64
long 2	1.39	1.42
long 3	2.52	2.61
side 1	0.64	0.64
side 2	1.38	1.37
side 3	2.52	2.57
vert 1	1.75	1.55
vert 2	5.34	5.20
vert 3	25.52	-
pitch 1	1.07	1.27
pitch 2	2.09	2.26
pitch 3	3.95	4.05
yaw 1	0.63	0.64
yaw 2	1.46	1.50
yaw 3	2.80	2.86
roll 1	2.36	2.21
roll 2	5.21	5.08
roll 3	39.14	-

Table 4.2: Comparison of simulated and measured resonance frequencies of the BS triple suspension. Each DOF is shown, including the respective three resonances. The longitudinal and vertical DOF are abbreviated with long and vert.

It can be seen that most resonances fit very well with the simulations, while

others deviate by up to 12 %. The strongest deviations between simulation and measurement can be observed for the first vertical and roll DOF. Both of them could be explained by slightly softer upper blade springs.

#### 4.2.7 Evaluation of the expected performance

The influence of seismic and BOSEM noise on the BS motion was simulated to predict the performance of the BS suspension. As the motion of the BS couldn't be measured without an interferometric set-up, its Simulink model (see section 4.2.3) was used. The suspension parameters in the model were adjusted to fit the resonance frequencies in table 4.2.6. To calculate the seismic noise contribution, the motion of the SAS (see chapter 1.3.2) has been projected to BS motion, using the transfer function (TF) through the suspension's state-space model. It was then multiplied by a coupling factor from the respective DOF to the differential arm motion of the sub-SQL interferometer. The BOSEM noise was calculated by projecting it through the feedback servo, followed by the suspension's TF from the first suspension stage to the suspended BS. The result was again multiplied with the coupling factor, converting motion in the respective DOF into differential arm motion.

The resulting noise contributions can be seen in figure 4.15 and 4.16. The side and roll DOFs were omitted, as their low motion combined with their low coupling factors reduce their noise to well below the noise of the other DOFs. The coupling factors for the pitch and yaw DOFs strongly depend on the spot centering of the laser beam onto the BS. For both DOFs, a spot centering offset of 1 cm was assumed. This provides more alignment options for the laser beam to the input mirrors of the arm cavities while sacrificing spot centering on the BS. The vertical coupling factor originates from a pitch offset of the interferometer arm and thus the beam splitter with respect to gravity. It is estimated to be 0.001, which agrees with the coupling factor in other subsystems of the AEI 10 m prototype, such as the frequency reference cavity (see chapter 1.3.3). The red box in figure 4.15 and 4.16 indicates the set requirement of  $10^{-17} \text{ m}/\sqrt{Hz}$  above 40 Hz. It can be seen that the noise in all DOFs is suppressed to below the set requirements. Nonetheless, the BOSEM noise in the vertical DOF nearly reaches  $10^{-17} \text{ m}/\sqrt{Hz}$  above 40 Hz and should be kept in mind for future noise investigations.

CHAPTER 4. BEAM SPLITTER FOR THE SUB-SQL INTERFEROMETER

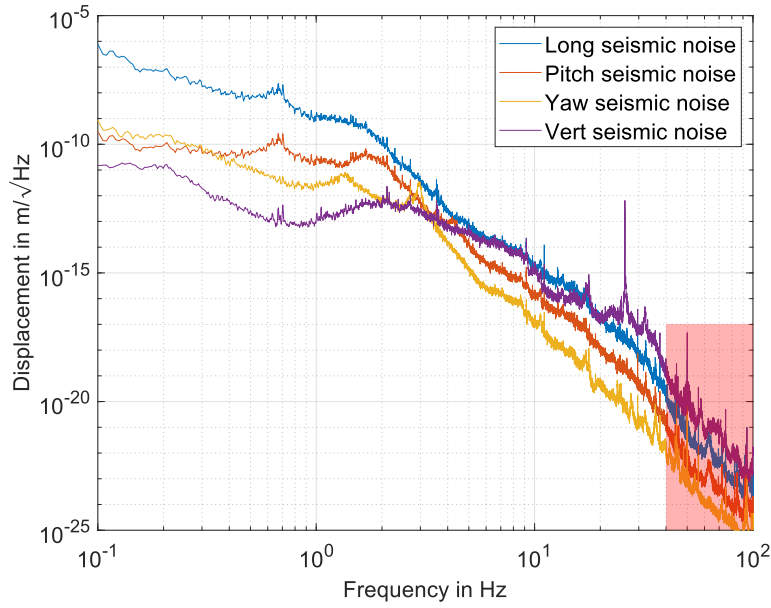


Figure 4.15: Seismic noise, coupling from SAS tabletop into the motion of the suspended BS in different DOFs. The red area indicates the requirements of  $10^{-17} \text{ m}/\sqrt{\text{Hz}}$  above 40 Hz.

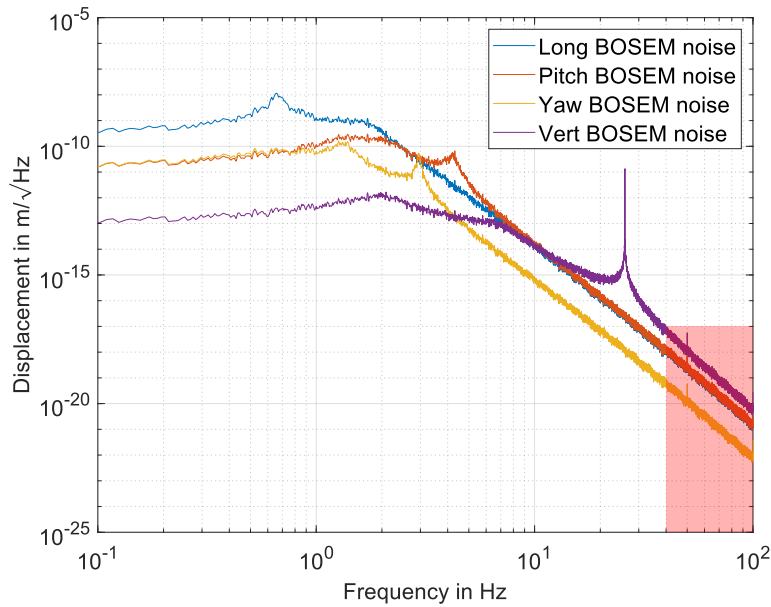


Figure 4.16: BOSEM noise, coupling into the motion of the suspended BS in different DOFs. The red area indicates the requirements of  $10^{-17} \text{ m}/\sqrt{\text{Hz}}$  above 40 Hz.

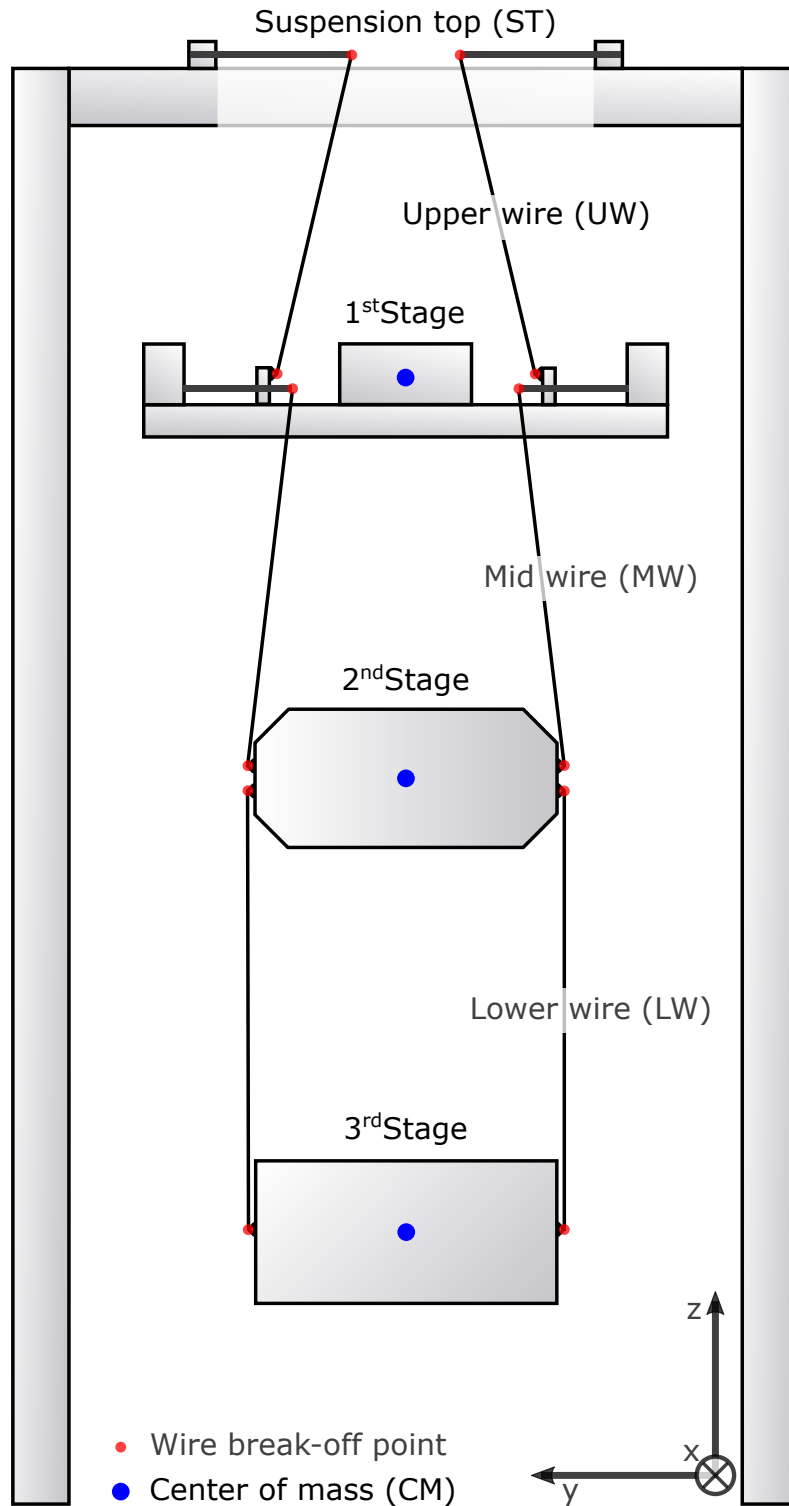


Figure 4.17: Schematic of the BS triple suspension for the visualization of the parameters shown in table 4.3. X-axis pointing away from the reader.

CHAPTER 4. BEAM SPLITTER FOR THE SUB-SQL INTERFEROMETER

Parameter	Value	Unit
ST		
UW y-separation	50	mm
UW length	222.8	mm
<i>1<sup>st</sup></i> Stage		
Mass	2	kg
x-dimension	130	mm
y-dimension	350	mm
z-dimension	58	mm
I <sub>x</sub>	0.0121	kg m <sup>2</sup>
I <sub>y</sub>	0.0025	kg m <sup>2</sup>
I <sub>z</sub>	0.0134	kg m <sup>2</sup>
UW y-separation	140	mm
UW to CM z-separation	1	mm
MW x-separation	40	mm
MW y-separation	100	mm
MW to CM z-separation	3	mm
<i>2<sup>nd</sup></i> Stage		
Mass	1.42	kg
x-dimension	50	mm
y-dimension	183	mm
z-dimension	85	mm
I <sub>x</sub>	0.0047	kg m <sup>2</sup>
I <sub>y</sub>	0.0012	kg m <sup>2</sup>
I <sub>z</sub>	0.0040	kg m <sup>2</sup>
MW x-separation	40	mm
MW y-separation	175	mm

CHAPTER 4. BEAM SPLITTER FOR THE SUB-SQL INTERFEROMETER

MW to CM z-separation	1	mm
LW x-separation	6	mm
LW y-separation	175	mm
LW to CM z-separation	1	mm
<i>3<sup>rd</sup> Stage</i>		
Mass	1.48	kg
x-dimension	49	mm
y-dimension	165	mm
z-dimension	85	mm
I <sub>x</sub>	0.0042	kg m <sup>2</sup>
I <sub>y</sub>	0.0012	kg m <sup>2</sup>
I <sub>z</sub>	0.0036	kg m <sup>2</sup>
LW x-separation	6	mm
LW y-separation	175	mm
LW to CM z-separation	1	mm

Table 4.3: Overview of the BS triple-suspension parameter. I<sub>x</sub>, I<sub>y</sub> and I<sub>z</sub> describe the moment of inertia around the corresponding axis. In figure 4.17, the location of the various parameters is shown.

## Chapter 5

# An output mode cleaner for the sub-SQL interferometer

---

In this chapter, the design and construction of a quasi monolithic output mode cleaner (OMC) for the sub-SQL interferometer of the AEI 10 m prototype is described. Its optical and mechanical parameters are chosen in a way to reduce optical losses to below 1 %, improving future quantum techniques tested in the sub-SQL interferometer. Further, the design reduces the amount of light retro-reflected into the interferometer while providing the required amount of mode and frequency filtering. The design performance can only be reached by carefully pairing the available optics after measuring their properties. This chapter includes a list of the important parameters and how to measure them, as well as a documentation of the assembly process.

The OMC has to be suspended by a double suspension to reduce the noise caused by pointing noise and retro reflected light. This chapter contains a suspension design providing the required seismic isolation for a quasi monolithic OMC.

A step-by-step guide to build a low loss OMC as well as experiences made during the design and assembly procedure can be found in the appendix B.

## 5.1 Mode filtering

This section provides a short introduction to laser modes and their behavior inside optical cavities. Basic knowledge and a set of formulas for Gaussian beams are required to design a cavity, as described in chapter 5.2. Starting with the definition of a Gaussian beam, the concept of laser modes inside a cavity will be covered. This is followed by an easy way to determine the properties of a resonant Gaussian beam inside a cavity using ABCD-matrices. With the knowledge about laser modes and how they couple into cavities, both the necessity and the working principle of a mode cleaner can be described.

### 5.1.1 Gaussian beam

A Gaussian beam is named for its transverse intensity distribution. When travelling in z-direction, its electromagnetic field ( $E$ ) for a defined laser frequency is described in [FS10] by

$$E(t, x, y, z) = \exp(i(\omega t - kz)) \sum_{n,m} a_{n,m} u_{n,m}(x, y, z), \quad (5.1)$$

where  $k$  is the wavenumber ( $k = \omega/c$ ), and  $\omega$  is the angular frequency of the laser.  $a_{n,m}$  are complex amplitude factors and  $u_{n,m}$  is a set of spatial modes. The spatial modes describe the transverse amplitude distribution in the x and y-direction, depending on the z position along the laser beam. One of the commonly used spatial mode sets is the set of Hermite-Gaussian modes. It fulfills the requirement of being a solution to the paraxial wave equation [SSP01; KL66] and a complete set of eigenmodes of a cavity with spherical mirrors. Another similar set of modes is the set of Laguerre-Gaussian modes [KL66]. The zeroth-order Hermite-Gaussian mode is defined by

$$u_{0,0}(x, y, z) = \sqrt{\frac{2}{\pi}} \frac{1}{\omega(z)} \exp(i\Psi(z)) \exp\left(-ik \frac{x^2 + y^2}{2R(z)} - \frac{x^2 + y^2}{\omega^2(z)}\right) [\text{FS10}] \quad (5.2)$$

## CHAPTER 5. AN OUTPUT MODE CLEANER FOR THE SUB-SQL INTERFEROMETER

Here,  $\omega$  is the radius of the laser beam (see below).  $\Psi$  is the Gouy-Phase, describing a phase lag of the Hermite-Gaussian mode compared to a planar wave[FS10].  $R$  is the radius of curvature of the wavefront. Using equations 5.1 and 5.2 the transverse intensity distribution ( $I$ ) can be calculated by multiplying the electromagnetic field  $E$  with its complex conjugate  $E^*$ .

$$I(x, y, z) = EE^* = \frac{2P_0}{\pi\omega^2(z)} \exp\left(-2\frac{x^2 + y^2}{\omega^2(z)}\right) \quad (5.3)$$

$P_0$  is the laser power of the described beam. The radius of the laser beam  $\omega$  is defined by the distance from the beam axis to the position, where the intensity reaches  $1/e^2$  of the maximum intensity.

The propagation of a Gaussian beam within a constant medium can fully be described by the size and position of its waist. If propagating inside a constant medium without beam shaping elements, such as lenses or curved mirrors, the beam waist ( $\omega_0$ ) is the minimum radius of the laser beam. The beam radius at any position ( $\omega(z)$ ) can be calculated with the waist position ( $z_0$ ) and the Rayleigh range ( $z_R$ ), as described in equation 5.5. The Rayleigh range describes the range of the near field of the laser beam and is defined for a laser wavelength ( $\lambda$ ) in equation 5.4. Further, the radius of curvature of the wavefront ( $R$ ) of the Gaussian beam can be calculated using equation 5.6.

$$z_R = \frac{\pi\omega_0^2}{\lambda} \quad (5.4)$$

$$\omega(z) = \omega_0 \sqrt{1 + \left(\frac{z - z_0}{z_R}\right)^2} \quad (5.5)$$

$$R(z) = z - z_0 + \frac{z_R^2}{z - z_0} \quad (5.6)$$

The properties of the Gaussian beam can be summarized in the Gaussian beam parameter  $q(z)$  [Ald03; FS10]. The Gaussian beam parameter is a complex function defined by

CHAPTER 5. AN OUTPUT MODE CLEANER FOR THE SUB-SQL  
INTERFEROMETER

$$q(z) = z - z_0 + iz_R \quad (5.7)$$

Usually, an optical set-up contains various optical elements, including those which change the beam parameters. It can be divided into several segments, each fully described by the propagation of the Gaussian parameter. Each time the laser beam is reflected by or transmitted through an optical component or travels inside a medium, a matrix can be used to describe the change applied to the Gaussian parameter. These matrices are called ABCD-matrices.

The different ABCD-matrices for each interaction of the laser beam with a medium, such as propagation, reflection or transmission, can be found in [FS10]. To describe the behavior of a laser beam inside a cavity (see chapter 5.1.2), only two ABCD-matrices are required. The first matrix  $M_P$  describes the propagation of the laser beam inside a medium with a refractive index  $n$  a length  $L$ . The second matrix  $M_R$  describes the reflection of the laser beam from a mirror with a radius of curvature  $R_C$ , a horizontal angle of incidence  $\alpha$ , and a refractive index  $n$  of the surrounding medium.

$$M_P = \begin{pmatrix} A & B \\ C & D \end{pmatrix} = \begin{pmatrix} 1 & \frac{L}{n} \\ 0 & 1 \end{pmatrix} \quad (5.8)$$

$$M_R = \begin{pmatrix} 1 & 0 \\ -\frac{2n}{R_C}(\cos \alpha)^{\pm 1} & 1 \end{pmatrix} \quad (5.9)$$

To distinguish between the reflection in the horizontal and the vertical plane, the C component of  $M_R$  is either multiplied with or divided by the cosine of the angle of incidence. Further, a reflection matrix  $M_{\pm}$  needs to be implemented just before every ABCD-matrix describing a reflection from a mirror.  $M_{\pm}$  describes the phase flip of the horizontal mode, which is reflected from a non-zero angle of incidence. Thus, plus signs are assigned for a vertical mode and minus signs for a horizontal mode [Ara13].

$$M_{\pm} = \begin{pmatrix} \pm 1 & 0 \\ 0 & \pm 1 \end{pmatrix} \quad (5.10)$$

The Gaussian beam parameter  $q_2$  at the end of propagation or after the reflection from a mirror can be calculated with the individual components of the corresponding ABCD-matrix and the Gaussian parameter of the incoming beam ( $q_1$ ).

$$q_2 = n_2 \left( \frac{Aq_1n_1^{-1} + B}{Cq_1n_1^{-1} + D} \right), \quad (5.11)$$

where  $n_1$  is the refractive index of the medium of the incoming beam, and  $n_2$  is the refractive index of the medium of the outgoing beam. To describe successive propagation and reflections, the corresponding ABCD-matrices can be multiplied to form a combined ABCD-matrix. The Gaussian beam parameter may be different for the horizontal and the vertical mode. This is called astigmatism.

### 5.1.2 Modes inside a cavity

A cavity is an optical resonator. If a specific set of requirements is fulfilled, a laser beam is resonant inside it. The cavity consists of two or more reflecting surfaces arranged to circulate a laser beam within a transmitting medium. Depending on the reflectivity of the individual reflecting surfaces, after circulation, the laser beam is partly reflected by the cavity's input surface and partly transmitted through one or more output surfaces. Usually, a cavity is designed to have one reflected or one reflected and one transmitted beam. Transmissions through other reflecting surfaces are assumed to be losses.

To fully resonate an incoming laser beam in a cavity, two resonance conditions need to be fulfilled. First, a laser beam can be resonant inside a cavity when the Gaussian beam parameter after a full round trip equals the Gaussian beam parameter of the laser beam entering the cavity. If the Gaussian beam parameter of an incoming beam equals the resonant Gaussian beam parameter, it can resonate

## CHAPTER 5. AN OUTPUT MODE CLEANER FOR THE SUB-SQL INTERFEROMETER

inside the cavity. The second resonance requirement is to match the cavity round trip length to a multiple of the wavelength of the incoming light. A deviation from the first requirement is called a mode mismatch, while a length deviation of below one wavelength is called a detuning.

In the scope of this thesis, the focus is on the special case of impedance-matched cavities. As mentioned above, the reflectivities of the surfaces, circulating the laser light determines the amount of reflected and transmitted light after resonating inside the cavity. Assuming no losses and an identical reflectivity of the input and output surface, the reflection of the input light field destructively interferes and cancels the light field, leaking from the cavity through the input surface [Sie86]. Without any detuning or mode mismatch, this leads to a purely transmitting cavity. Such a cavity is called an impedance-matched cavity.

A set of parameters can be used to quantify the performance of a cavity. These parameters are the free spectral range (FSR), the full-width half maximum (FWHM) and the finesse ( $F$ ). The FSR is the frequency shift of the incoming laser light required to equal a detuning of one wavelength. As can be seen in equation 5.12, it is dependent on the cavity round trip length ( $L_R$ ), the laser wavelength ( $\lambda$ ) and the speed of light ( $c$ ). The FWHM is the frequency shift or the corresponding detuning required to reduce the transmission of an impedance-matched cavity by half. The finesse of a cavity is the ratio of the FSR to the FWHM (see equation 5.13). In an impedance-matched cavity, the finesse is directly related to the reflectivity ( $R$ ) of the input and output surface (see equation 5.14 for a reflectivity close to 1), as shown in [FS10].

$$FSR = \frac{c}{L_R} \quad (5.12)$$

$$FWHM = \frac{FSR}{F} \quad (5.13)$$

$$F = \frac{\pi}{1 - R} \quad (5.14)$$

### Detuning

As can be seen in equation 5.12, detuning the cavity length corresponds to shifting the laser frequency. A frequency shift by one FSR equals a length change of one wavelength. The transmission change in dependence of the cavity length of an impedance matched, empty (i.e., refractive index of 1) cavity with a round trip length of 1 m can be seen in figure 5.1. The cavity length is displayed in units of the laser wavelength. Knowing the cavity length, and thus the FSR allows assigning a correlated frequency axis to the plot.

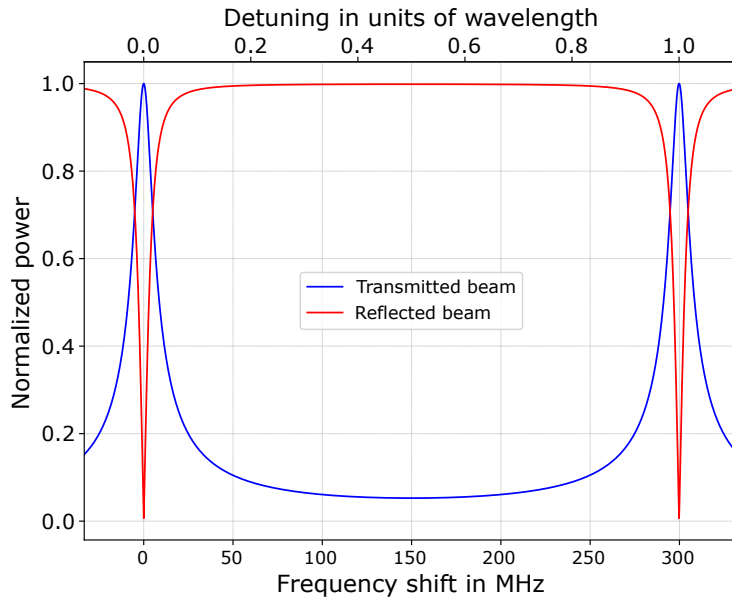


Figure 5.1: Transmission through and reflection from an impedance-matched cavity with a round trip length of 1 m. The power of the transmitted and the reflected beam is normalized to the power of the input beam. The upper x-axis shows the detuning in units of the laser wavelength. The bottom x-axis shows the corresponding frequency shift calculated from the FSR (equation 5.12). The cavity was simulated with Finesse 2. [gwo22]

### Mode mismatch

As mentioned in chapter 5.1.2, a mode mismatch arises if the input beam parameters do not match the beam parameters of the eigenmode of the cavity. Every transverse electromagnetic field distribution can be expressed by a superposition of spatial modes. One example is the set of Hermite-Gaussian modes, forming a complete, orthogonal set of modes from which any laser beam can be composed. If

## CHAPTER 5. AN OUTPUT MODE CLEANER FOR THE SUB-SQL INTERFEROMETER

an input beam is slightly misaligned with respect to the eigenmode of a cavity, most of the laser field will still fulfill the resonance condition, thus resonating inside the cavity. For an impedance matched cavity, the residual light is reflected, containing the input field without the field resonating inside and transmitted by the cavity. If the input axis of the incoming laser beam is misaligned towards the cavity axis, the resulting transverse electromagnetic fields can be easily described with the set of Hermite-Gaussian modes (see figure 5.2) [FS10]. If the wavefront curvature is misaligned, the resulting transverse field can be conveniently described with the set of Laguerre-Gaussian modes. The order of each mode is given by the sum of the horizontal and vertical modes of the respective spatial mode. All mode orders above the base (zeroth order) mode are called higher-order modes.

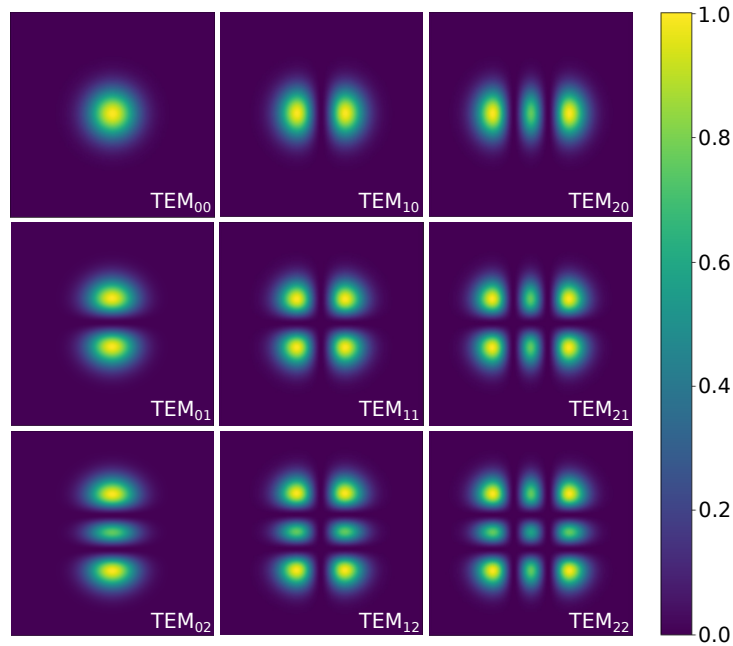


Figure 5.2: Normalized intensity profiles of Hermite-Gaussian modes up to the 4th order. They are also called transverse electromagnetic modes (TEM) and are numbered according to their horizontal and vertical order with  $TEM_{m,n}$ , with  $m$  and  $n$  reaching from 0 to 2. The order of the Hermite-Gaussian mode is the sum of  $m$  and  $n$ .

In chapter 5.1.1 the Gouy-phase ( $\Psi$ ) was introduced as a phase lag of a Gaussian beam compared to a planar wave. This phase lag is added for each individual higher-order mode, accumulating to a total phase lag of  $(n + m + 1)\Psi$  [FS10]. Inside

## CHAPTER 5. AN OUTPUT MODE CLEANER FOR THE SUB-SQL INTERFEROMETER

the cavity, the Gouy phase leads to a frequency shift called the transverse mode spacing (TMS). The TMS frequency ( $f_{TMS}$ ) can be calculated, using

$$f_{TMS} = \frac{\Psi}{2\pi} FSR \quad [\text{Ara13}], \quad (5.15)$$

where FSR is the free spectral range of the cavity and  $\Psi$  is the Gouy phase in radians. Further, the Gouy phase can be calculated using the round trip ABCD-matrix of the cavity and its components A, B and D.

$$\Psi = \text{sgn}(B) \cos^{-1} \left( \frac{A + D}{2} \right) \quad [\text{Ara13}] \quad (5.16)$$

By detuning the cavity, different modes can be resonant inside the cavity. As shown in figure 5.1, an impedance-matched cavity transmits a narrow frequency band depending on its finesse, FSR and FWHM. By a small misalignment of the beam axis or wavefront curvature of the input beam relative to the cavity, higher-order spatial modes arise. E.g., a tilt or shift of the beam axis can be described by adding a TEM<sub>01</sub> or TEM<sub>10</sub> mode. In order to let the higher-order modes resonate in the same cavity, their frequency would need to be shifted by their order number multiplied by the TMS of the cavity. Thus, most higher-order modes are not resonant inside the cavity. An exception arises when the order number multiplied with the TMS equals the FSR. In this case, additionally, to the zeroth-order, other higher-order modes can co-resonate inside the cavity. The transmission through an impedance-matched cavity is a superposition of these resonant modes. This effect can be utilized to filter specific modes, as described in the next subsection.

### 5.1.3 Mode cleaner

In most applications, a Gaussian beam, i.e., a beam consisting of a pure Hermite-Gaussian, zeroth-order mode (TEM<sub>00</sub>), is desired. The laser emits a more or less pure TEM<sub>00</sub> mode. Its quality is often described by the  $M^2$ -factor. An  $M^2$ -factor of 1 equals a perfect TEM<sub>00</sub> mode, whereas higher values deviate from

## CHAPTER 5. AN OUTPUT MODE CLEANER FOR THE SUB-SQL INTERFEROMETER

it [LCW09]. Each time the laser beam is reflected from a non-perfectly spherical mirror, it will accumulate higher-order modes. This effect is even enhanced inside cavities. Additionally, every misalignment between the incident beam and the cavity eigenmode, be it a misalignment of the beam axis or a misalignment of the wavefront curvature, changes the higher-order mode content of the laser beam (see chapter 5.1.2).

A Fabry-Perot-Michelson interferometer (MI), such as most gravitational wave detectors, benefits from a well-defined  $\text{TEM}_{00}$  mode. To reduce shot noise (see chapter 1.2.1), the laser power on the detection photodiodes is kept small. This is done by operating the MI close to the dark port, meaning close to destructive interference of the recombined laser beams returning from the arm cavities towards the output of the detector. The light in the output port is the signal caused by a differential arm length change, the sidebands imprinted onto the laser beam, and the light transmission arising from a detuning of the MI. The sidebands are required to control the length of the MI arms and the arm cavities at frequencies below and within the measurement band. For the read-out of the signal, a detuning of the MI leads to additional light in the output port, also known as a dark port offset (see chapter 1.2.3). Additionally, higher-order modes can leak into the output port, as they do not necessarily interfere destructively. Both the higher-order mode content and the sidebands represent a significant amount of laser power compared to the dark port offset and the signal. This would increase the shot noise on the photodiodes at the detector output and needs to be reduced.

An output mode cleaner can be used to filter out higher-order modes and sideband frequencies. As explained in chapter 5.1.2, a cavity can reject higher-order modes while resonating and transmitting the  $\text{TEM}_{00}$  mode. This effect is used in mode cleaners to filter out higher-order modes. The modulation sidebands mainly consist of a  $\text{TEM}_{00}$  mode. They are frequency shifted by the modulation frequency, which is typically at a few MHz in comparison to the main beam. Thus, by resonating the main beam inside the cavity, the sidebands can be rejected as well.

To achieve the right filter performance, an OMC needs to be carefully designed. It requires a sufficient suppression of present higher-order modes and sideband frequencies while transmitting the signal and main beam as loss-free as possible. The exact requirements, as well as the design of an output mode cleaner for a MI

with arm cavities, is the topic of the next section.

## 5.2 Designing the OMC

To design an output mode cleaner (OMC) for an optical system, first, a set of requirements need to be defined. These requirements are related to the mode filter performance, as well as the added loss of the OMC to the system. With the known requirements, individual cavity parameters can be chosen by simulating and optimizing its mode filter performance. Different design parameters need to be considered as trade-offs, improving an important property while worsening another one.

### 5.2.1 Requirements for the OMC

The probably important property of a mode cleaner is its filter performance. The OMC designed and built in the scope of this thesis is the OMC for the AEI 10 m prototype's sub-SQL interferometer (see chapter 1.3.4). Its mode filter requirements are similar to the requirements of a gravitational wave detector. The main purpose is to suppress the combined power of the higher-order modes and phase modulation sidebands hitting the detection photodiode (see chapter 5.1.3). To ensure that the shot noise resulting from the higher-order modes plus the sidebands does not influence the signal, it is commonly suppressed to a tenth of the shot noise of the leaking main beam carrying the signal. Chapter 1.2.1 shows a laser power ( $P$ ) dependency of  $\sqrt{P}$  for shot noise. Thus, the combined laser power of the higher-order modes and sideband frequencies needs to be suppressed to a hundredth of the transmitted  $\text{TEM}_{00}$  mode. The suppression factor of higher modes and sidebands is addressed in chapter 5.2.2 and 5.2.3. It is further influenced by astigmatism, arising from curved cavity mirrors hit under an angle of incidence differing from 0 deg. This is covered in chapter 5.2.4.

Another important aspect of OMCs for gravitational wave detectors is the loss of light in the  $\text{TEM}_{00}$  mode. The usage of most quantum noise reduction techniques, such as squeezing, requires low optical losses in the entire system [DKM19]. In [DMM22] it is shown that the lower the total optical loss of a system, the more important even low-loss contributions of individual subsystems become. Here, a

## CHAPTER 5. AN OUTPUT MODE CLEANER FOR THE SUB-SQL INTERFEROMETER

special focus is on reducing the optical losses of the OMC as far as possible while maintaining a sufficient mode filter performance. The goal is to provide a guide for future OMCs used in gravitational wave detectors with negligible losses. The loss of the OMC depends on the quality of the optics covered in chapter 5.3, as well as the OMC's finesse discussed in chapter 5.2.3.

### 5.2.2 Choosing FSR and RoC

The mode filtering performance for a set FSR and TMS can be simulated when the output beam profile of the optical system is known. First, a preliminary finesse, as well as a cavity form, need to be chosen. As described in chapter 5.1.1, the TMS is defined when the radii of curvatures and distances between the different cavity mirrors are known. With a known higher-order mode power distribution in the output beam determined from a decomposition of the interferometer output beam into an HG mode basis and the cavity's transmission function (see chapter 5.1.2), the transmission of each mode can be calculated. The sum of the powers of the transmitted higher-order modes and sidebands can be plotted against the cavity length and the radius of curvature of the cavity mirrors. Such a plot can be seen in figure 5.3. The phase modulation frequency of the sidebands in the sub-SQL interferometer is 21.34 MHz.

For the OMC of the AEI 10 m prototype's sub-SQL interferometer, the output beam profile of the aLIGO detectors was used. As the sub-SQL interferometer is currently under construction, no exact mode profile of the output beam is known. The aLIGO detectors have a similar basic set-up as the future sub-SQL interferometer and should give a rough overview of what output mode profile can be expected. To compensate for the unknown output mode profile and any inaccuracies during the manufacturing of the components, the OMC design is aimed at a ten times better mode filtering performance than required.

Similar to the aLIGO OMC designs, the basic design of a bow-tie cavity was chosen for the sub-SQL interferometer's OMC (see figure 5.8). The cavity consists of an identical pair of flat input and output mirrors. Further, two curved, highly reflective (HR) mirrors complete the cavity round trip path. The exact layout, including all chosen parameters, can be found in chapter 5.2.5.

## CHAPTER 5. AN OUTPUT MODE CLEANER FOR THE SUB-SQL INTERFEROMETER

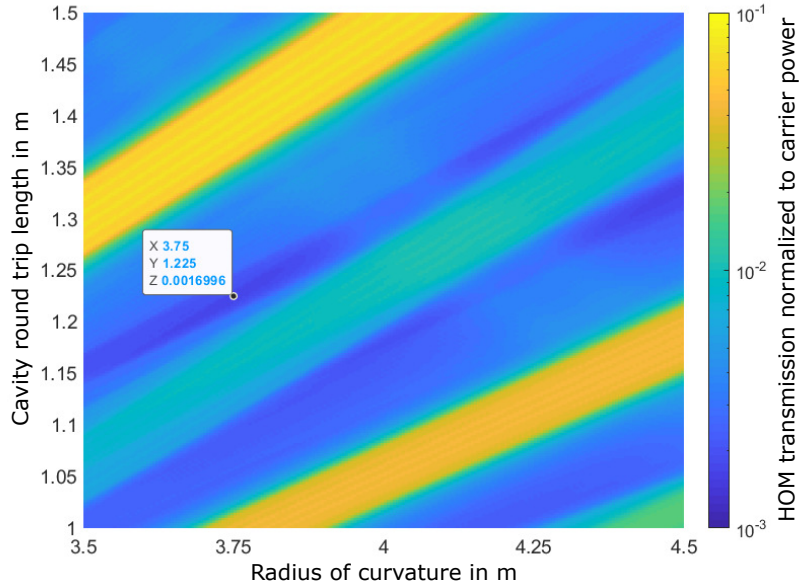


Figure 5.3: This figure shows the summed transmission of all higher-order modes normalized to the  $TEM_{00}$  mode in dependence of the cavity round trip length and the RoC of the HR mirrors. It allows finding a fitting pair of the FSR and the TMS. The simulation was done using the higher-order mode profile of the aLIGO detectors.

With the aLIGO output beam profile and the basic design of a bow-tie cavity, the mode filter performance could be simulated. It can be seen in figure 5.3 in dependence of the cavity round trip length and the radius of curvature of both HR mirrors. This simulation can be used to find an optimal set of parameters. For the sub-SQL interferometer’s OMC, a radius of curvature of 3.75 m and a round trip length of 1.225 m were chosen. This is not just a local minimum but rather provides room for errors in the final radius of curvature and round trip length. Even bigger errors in the radius of curvature would be compensatable by changing the round trip length by a few millimeters.

The resulting TMS could be visualized by plotting it for each mode order against the normalized FSR. The resulting plot can be seen in figure 5.4. The  $TEM_{00}$  mode is directly at the FSR indicated by the dashed line through the different mode orders. The distance of each mode to the FSR line visualizes how far each mode is from resonating inside the cavity. Further, astigmatism caused by the angle of incidence onto the curved mirrors can be seen. As the TMS differs for horizontal and vertical

## CHAPTER 5. AN OUTPUT MODE CLEANER FOR THE SUB-SQL INTERFEROMETER

modes, each mode order spreads the different modes of one order further from each other. In figure 5.4 the modes of each order are shown, which differ the most from each other. This forms the region in which different horizontal and vertical order mode combinations could be present.

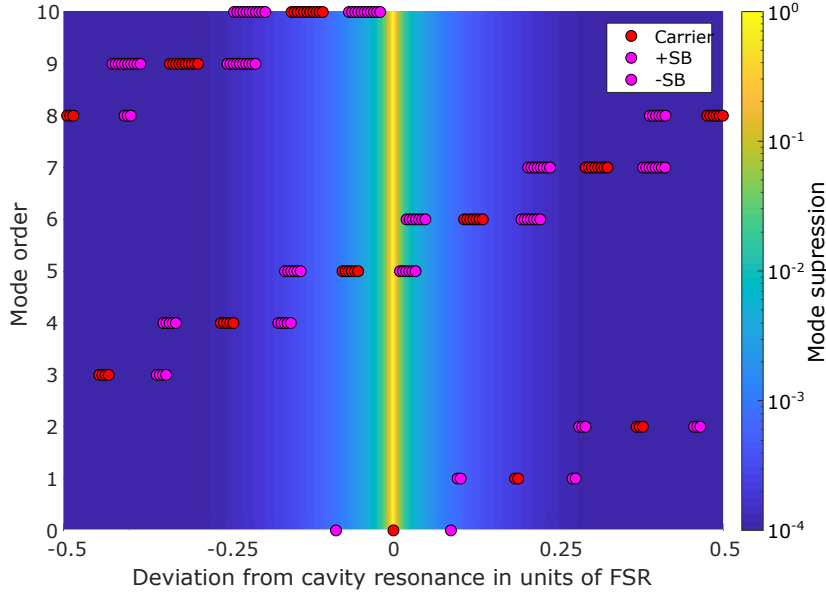


Figure 5.4: Here, the distance in units of the FSR for all higher-order modes of both the main beam and the phase modulation sidebands from the cavity resonance can be seen. The phase modulation frequency of the sidebands is 21.34 MHz. Due to astigmatism, the vertical and horizontal modes of the same order spread depending on the order number. The background shows the mode suppression for each HOM of the carrier and the sidebands.

### 5.2.3 Choosing a finesse

The finesse influences the cavity in two different aspects. First, an increased finesse reduces the FWHM at a given FSR and reduces the non-resonant light transmitted by the cavity. This can be seen exemplarily for different finesses in figure 5.5. Secondly, a higher finesse increases the overall losses of the cavity. The main contributors to the loss are scattering at each mirror surface, transmission through the curved HR mirrors and absorption within the reflective coatings. These losses can be summarized as a round trip loss, which describes the loss a laser beam suffers by circulating once within the cavity. The finesse is directly proportional to

## CHAPTER 5. AN OUTPUT MODE CLEANER FOR THE SUB-SQL INTERFEROMETER

the number of round trips of the circulating light. Each round trip experiences the round trip losses, resulting in higher losses at a higher finesse. Due to the increased losses, the finesse can not be increased arbitrarily but needs to be chosen carefully when losses are of interest. As shown in equation 5.14, the reflectivity of the input and output mirror can be used to tune the finesse to the desired value.

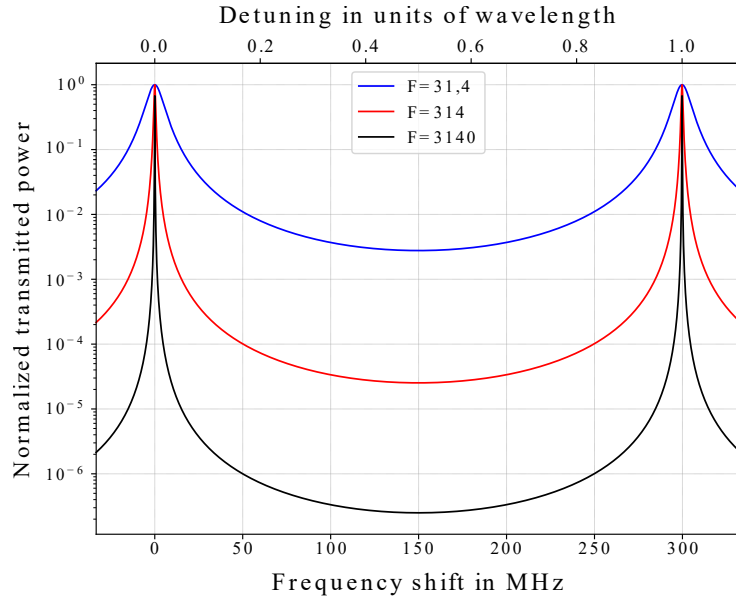


Figure 5.5: Transmission of an impedance-matched cavity with a round trip length of 1 m for different finesse values. It is shown in dependence of both, the frequency shift and the detuning from resonance.

To minimize the losses, the cavity finesse of the OMC for the sub-SQL interferometer was chosen to just fulfill the mode filter requirement, including the safety margin of factor 10. Using the cavity length and radius of curvature chosen in chapter 5.2.2, as well as the mentioned output mode profile of the aLIGO detectors, the required finesse could be calculated. The resulting finesse is  $F = 229$ , corresponding to a reflectivity of  $R = 0.9865$  of the cavity's input and output mirror.

### 5.2.4 Choosing the AoI

In a bow-tie cavity, a horizontal and vertical wavefront curvature mismatch arises by the curved mirrors not being hit under normal incidence. This mismatch between the two orthogonal wavefront curvatures is called astigmatism [FS10]. The laser beam circulating inside the cavity is designed to travel only in the horizontal plane;

## CHAPTER 5. AN OUTPUT MODE CLEANER FOR THE SUB-SQL INTERFEROMETER

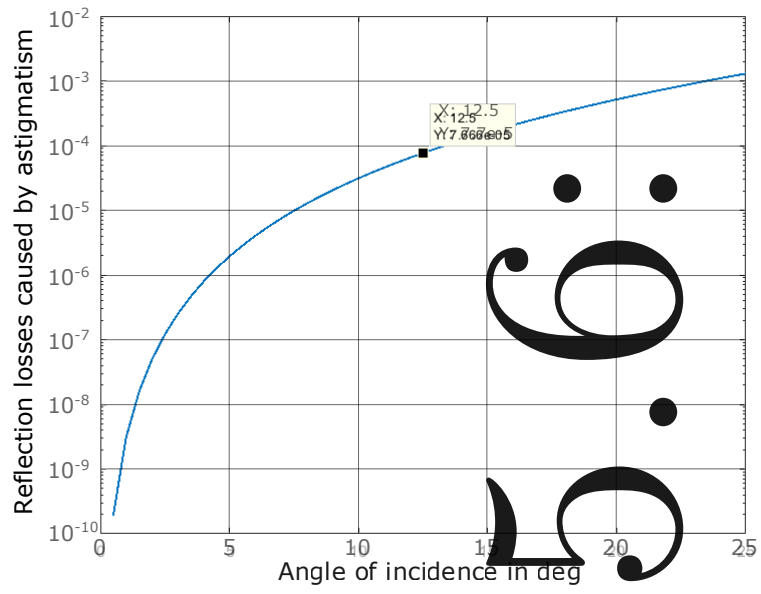
thus, the vertical AoI is zero. Due to space constraints, the cavity mirrors need to be spatially separated and hence, require a horizontal AoI bigger than zero. As the AoI changes the radius of curvature as seen by the laser beam, a wavefront curvature mismatch arises. Astigmatism increases with an increase of the horizontal AoI. Thus, to reduce astigmatism, a small angle of incidence would be beneficial.

Opposing the minimization of the horizontal AoI is the formation of a counter-propagating cavity mode. As each mirror surface scatters a laser beam depending on its surface uniformity and micro-roughness (see chapter 2.1), a part of the beam is always scattered back towards its incident direction. The amount of light scattered towards a certain angle is quantified by the mirrors BRDF, which is explained in chapter 3.1.4. A portion of the light scattered towards the direction of the incident beam will match the cavity mode and thus resonate inside the cavity. This resonant light field is called counter-propagating mode, as its direction of propagation is opposed to the original cavity mode. The counter-propagating mode exits the cavity towards the input mirror and propagates directly back into the preceding experiment. There it interferes with the present light field, influencing the experiment's output signal. As typically, the BRDF reduces towards higher angles, an increased AoI is beneficial to reduce the power in the counter-propagating mode.

Astigmatism influences the OMC performance in two different ways. Firstly, it increases the separation of the horizontal and vertical TMS, mentioned in chapter 5.2.2 and visualized in figure 5.4. Secondly, astigmatism influences the mode-matching of the incoming beam to the cavity, thus rejecting a part of it. This rejected light is reflected and counts as loss. The reflection loss caused by astigmatism is shown in figure 5.6. It is simulated using the Finesse 2 software [gwo22], assuming the cavity parameters and design determined in chapter 5.2.2 and 5.2.3 for a lossless cavity. It can be seen that when aiming for reflection losses below 0.1 %, the angle of incidence onto the curved mirrors should be kept below 24 deg. Alternatively, an astigmatic mode-matching could prevent these losses.

Figure 5.7 directly compares the opposing effects of astigmatism and scattering for the OMC performance. On the left-hand blue y-axis, the mode filter performance as higher-order mode suppression normalized to the incoming  $TEM_{00}$  mode is plotted. It is shown in dependence of the AoI on the curved HR mirrors. The plot was simulated, using an RoC of 3.75 m for the curved HR mirrors and a cavity finesse of

CHAPTER 5. AN OUTPUT MODE CLEANER FOR THE SUB-SQL INTERFEROMETER



CHAPTER 5. AN OUTPUT MODE CLEANER FOR THE SUB-SQL INTERFEROMETER

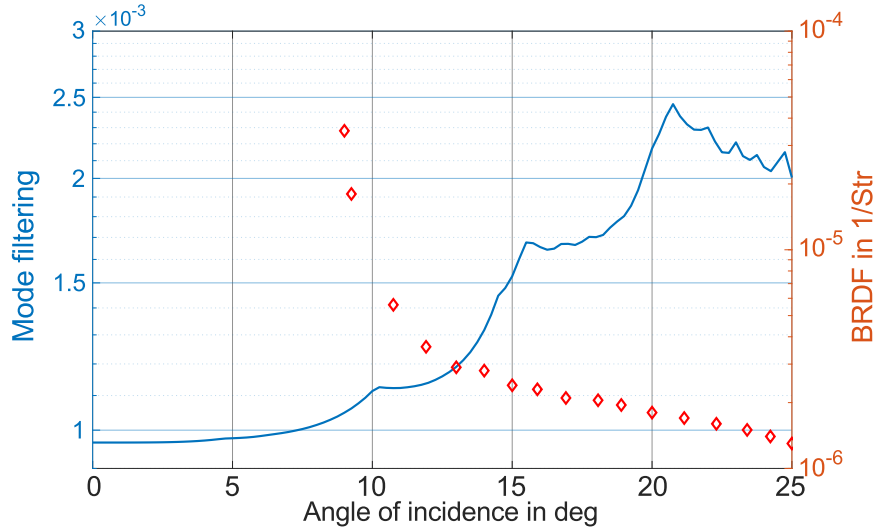


Figure 5.7: On the left y-axis, the mode filter performance of the OMC is shown higher-order mode suppression normalized to the  $TEM_{00}$  mode. It is plotted as a function of the AoI on the curved HR mirrors. As cavity parameters, an RoC of the HR mirrors of 3.75 m and a finesse of 229 were chosen. The right y-axis shows the BRDF function of an HR mirror in dependence on the scattering angle [Mag+12].

of UV curing glue, making it a quasi monolithic assembly. This reduces thermal noise within the OMC [Bon+17].

The incoming light is split into two parts; one is transmitted by beam splitter BS1 (splitting ratios see figure caption), split again by BS2, and steered ( $St_1$  and  $St_2$ ) towards two quadrant-photodiodes ( $QPD_1$  and  $QPD_2$ ). These help to align the OMC towards the output beam of the interferometer. The reflected beam is steered towards the OMC cavity. The cavity consists of the input mirror (Inm), the output mirror (Outm) and two curved mirrors ( $CM_1$  and  $CM_2$ ). After circulating inside the cavity, the resonant light is transmitted and steered ( $St_3$ ) onto BS3, splitting the laser beam towards the two detection PDs. The reflection of each QPD and PD is dumped at a V-shaped beam dump made from filter glass.

CHAPTER 5. AN OUTPUT MODE CLEANER FOR THE SUB-SQL INTERFEROMETER

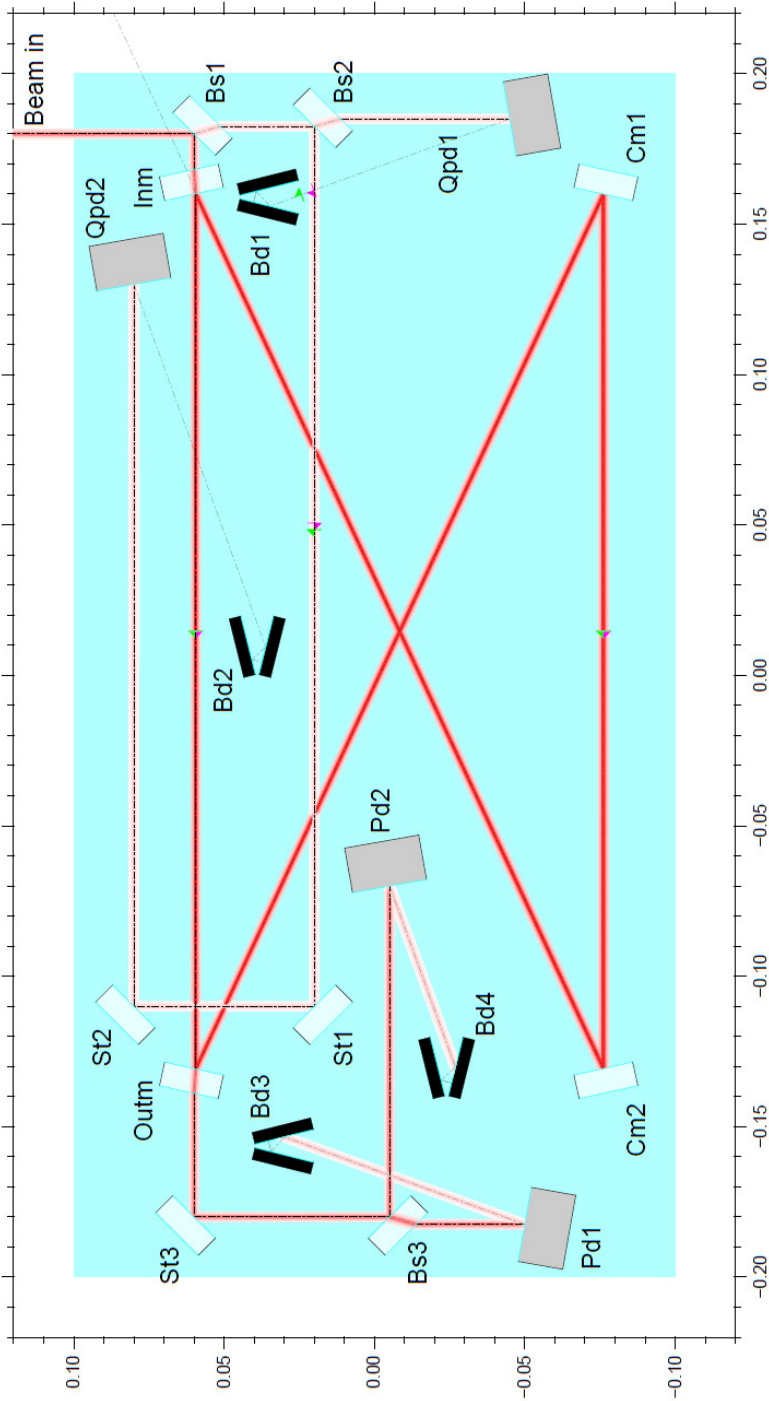


Figure 5.8: Optical layout for the OMC of the sub-SQL interferometer, visualized with the Optocad software.  $Bs_1$  is a beam splitter with a transmission of 250 ppm.  $Bs_2$  and  $Bs_3$  are beam splitter with a 50/50 splitting ratio.  $St_1$  to  $St_3$  are steering mirrors with a transmission of below 50 ppm.  $Qpd_1$  and  $Qpd_2$  are quadrant photodiodes,  $Pd_1$  and  $Pd_2$  are the detection photodiodes.  $Bd_1$  to  $Bd_4$  are filter glass beam dumps.

CHAPTER 5. AN OUTPUT MODE CLEANER FOR THE SUB-SQL  
INTERFEROMETER

Feature	Value	Unit
Round trip length	1.225	m
FSR	244.73	MHz
Finesse	229	—
Reflectivity Inm & Outm	98.65	%
Transmission CM <sub>1</sub> & CM <sub>2</sub>	5	ppm
RoC CM <sub>1</sub> & CM <sub>2</sub>	3.75	m
Angle of incidence	12.5	deg
Horizontal TMS	46.32	MHz
Vertical TMS	45.16	MHz

Table 5.1: Optical parameters for the OMC of the sub-SQL interferometer for the AEI 10 m prototype. CM<sub>1</sub> & CM<sub>2</sub> are the two HR curved mirrors. Inm and Outm are the flat input and output mirrors.

### 5.3 Requirements and testing of the optical components

In chapter 5.2.1 the optical properties of mirrors and positions defining the OMC cavity were discussed. For the manufacturing process, additional requirements, such as the quality of the optical surface and the components' geometries, need to be addressed. These additional requirements and the testing of the surface quality are the focus of this section. The test results are used to find low-scattering optics and to match the in and output mirrors for the cavity, as more than one set of optics was ordered. All optics are made from Suprasil 3 [Her22], a special low-loss fused silica material.

#### 5.3.1 Input and output mirror

The input and output mirrors are shaped similar to a tombstone, with a 20 mm by 30 mm squared front and rear surface and a thickness of 8 mm. The rear surface is AR coated to avoid reflection losses. It is wedged by 0.5 deg compared to the front surface to separate the arising ghost beams. The perpendicularity of the bottom surface relative to the front surface was defined as  $\pm 100 \mu\text{rad}$ . As the

## CHAPTER 5. AN OUTPUT MODE CLEANER FOR THE SUB-SQL INTERFEROMETER

beam axis of the input beam would require a pitch angle to compensate for the non-perpendicularity, this ensures a maximum vertical displacement of the beam on each mirror center by 1 mm. To reduce scattering as much as possible, the polishing specifications were set to the manufacturer's best effort, promising a micro-roughness RMS below 1 Å for the central surface pointing towards the cavity. The rear surface was polished to a micro-roughness RMS of below 5 Å, as the non-cavity side is not hit by the resonantly enhanced light field. The surface accuracy of the input and output mirrors was defined to be  $\lambda/10$  at 632.8 nm as proposed in [Arm22b] for the aLIGO OMCs.

### Scatter measurements

As the scattering of the light is resonantly enhanced inside a cavity together with its power, the scatter losses of the cavity components are a crucial contributor to the total OMC losses. Next to the surface properties, the cleanliness of the optical surfaces defines the scattering of an optic. Several repetitions of *first contact* [Tec22] and *drop and drag* cleaning were required in between scatter measurements to ensure that the scattering of any contamination was minimized. The scatter measurements were done using the previously built scatterometer described in chapter 3. The total integrated scattering (TIS) for all mirrors was calculated, assuming a radial symmetrical scatter behavior and a constant BRDF above 55 deg. The measurement of the ten coated and cleaned input and output mirrors can be seen in figure 5.9 and their corresponding TIS is shown in table 5.2.

As can be seen in figure 5.9 and the corresponding table 5.2, the results vary strongly. Due to a mix-up of mirrors at the coating company, several mirrors designed as steering mirrors with a micro-roughness RMS of below 5 Å were coated as input and output mirrors. After a closer inspection, it turned out that the optics with different polishing qualities originating from different polishing companies did not differ much in terms of their BRDF. Mirrors with a micro-roughness of both <1 ppm and <5 ppm RMS were found amongst the best performing samples. It is suspected that the scattering of the worse performing mirrors is dominated by contaminations, as the scattering of most mirrors improved after several cleaning attempts.

CHAPTER 5. AN OUTPUT MODE CLEANER FOR THE SUB-SQL INTERFEROMETER

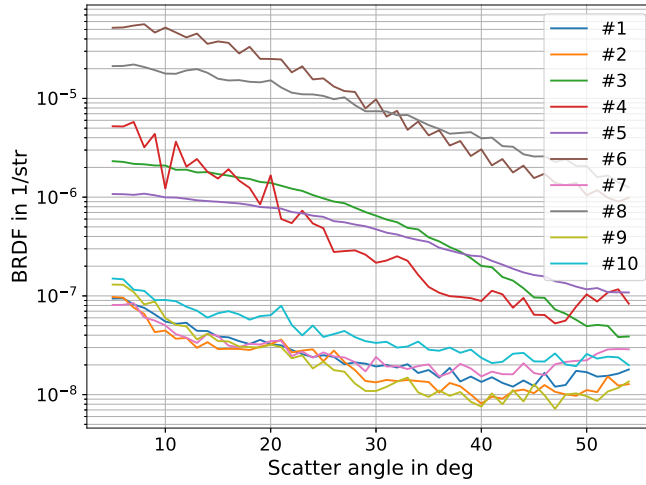


Figure 5.9: BRDF of ten possible input and output mirrors for the OMC cavity. All optics were cleaned at least once, using first contact and *drop and drag*.

Mirror	TIS in ppm
1	0.05
2	0.04
3	1.3
4	1.1
5	0.95
6	23.5
7	0.05
8	15.0
9	0.04
10	0.08

Table 5.2: TIS calculated from the BRDFs, shown in figure 5.9.

### Transmission and reflectivity measurements

The input and output mirrors' reflectivities contribute the most to the finesse of a low-loss cavity. Further, they ensure the impedance-matching of the cavity. As explained in chapter 5.1.2, an impedance-matched cavity requires identical reflectivities of the input and output mirror. A difference in reflectivity would lead to a partial reflection of the otherwise resonant and transmitted light field. This

CHAPTER 5. AN OUTPUT MODE CLEANER FOR THE SUB-SQL  
INTERFEROMETER

reflection would contribute to the OMC's total losses. Further, the reflectivity of both mirrors should match the design reflectivity to achieve the required finesse. The transmission (T) of the ten input and output mirrors was measured at an angle of incidence of 12.5 deg. The results are shown in table 5.3

Mirror	T in %
1	1.40
2	1.39
3	1.40
4	1.39
5	1.40
6	1.39
7	1.40
8	1.39
9	1.40
10	1.10

Table 5.3: Transmission of ten possible input and output mirrors for the OMC cavity. The absolute measurement error is  $\pm 0.01$  %, dominated by the power meters used for the measurement.

### 5.3.2 Curved mirrors

The OMC's curved mirrors are cylindrical optics with a diameter of 20 mm and a thickness of 8 mm. The radius of curvature is 3.75 m, as determined in chapter 5.2.2. Each of the two curved mirrors is attached to a ring-shaped PZT (see section 5.4.1), which can be used to control and lock the cavity length to the wavelength of the incoming laser light. The PZT is attached to a tombstone-like substrate. The front surface of the curved mirrors was polished to similar specifications as the input and output cavity mirrors, i.e., to a micro-roughness RMS of below 1 Å. The rear surface was AR coated and polished to an RMS below 5 Å. The HR coating's reflectivity was chosen to 5 ppm, nearly equalling the absorption losses of the coating of 1 ppm to 3 ppm as indicated by the manufacturer.

The surface accuracy of the curved mirror substrates was defined to be  $\lambda/10$  at a wavelength of 632.8 nm. Here, the polishing was chosen to be identical to the

## CHAPTER 5. AN OUTPUT MODE CLEANER FOR THE SUB-SQL INTERFEROMETER

input and output mirrors instead of reducing it as proposed in [Arm22a] to  $\lambda/4$ .

The tombstone-like substrate will be glued to the breadboard and thus requires a perpendicularity of  $\pm 100 \mu\text{rad}$  of the bottom and front surface. Further, the parallelism of the front and rear surfaces of the curved mirrors and the PZTs need to be equally accurate. The thickness uniformity of the PZTs has been measured using a micrometer gauge. Several of them showed thickness gradients of maximal  $1\text{-}2 \mu\text{m}$  over the full  $20 \text{ mm}$  diameter. This corresponds to a maximum tilt of  $50\text{-}100 \mu\text{rad}$ . Additionally, those causing only a horizontal yaw offset could be chosen. A yaw offset can be compensated later on by horizontally rotating the curved mirrors on the breadboard before the gluing process.

### Scatter measurements

The results of the scatter measurement can be seen as BRDF in figure 5.10 and as corresponding TIS in table 5.4. These measurements were taken after the curved mirror assembly described in section 5.4.1, as the assembly process might have been prone to adding contaminations to the mirror surfaces. Similar to the scatter measurements as seen in figure 5.9, the optics had to be repetitively cleaned, converging down towards a uniform scatter level. On average, the measured scattering is about a factor 5 worse than the scattering of the chosen flat mirrors. The increasing BRDF at  $27 \text{ deg}$ ,  $40 \text{ deg}$  and higher scattering angles can be explained by a part of the mounting structure overlapping with the scatter spot and adding additional noise during the measurement.

Mirror	TIS in ppm
1	0.24
2	0.69
4	0.55
6	0.48
10	0.73

Table 5.4: TIS calculated from the BRDFs, shown in figure 5.10.

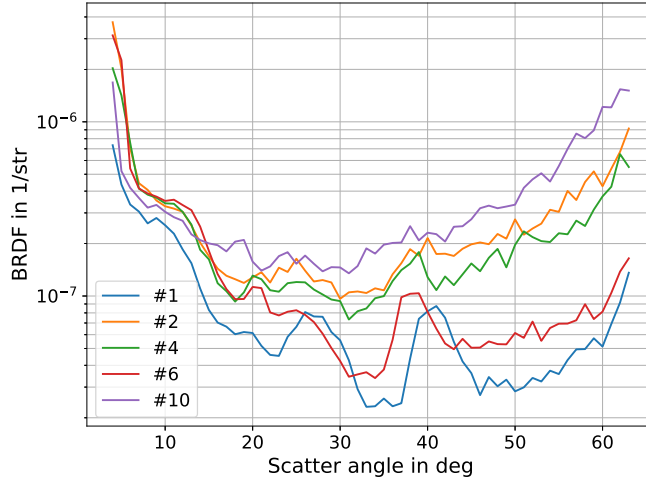


Figure 5.10: BRDF of ten possible curved mirrors for the OMC cavity. All optics were cleaned at least once, using first contact and *drop and drag*. Background scattering from the mounts dominates the measurements at scattering angles around 27 deg and 40 deg, as well as above 50 deg. Only five out of ten curved mirrors are shown, as these were already assembled.

### Transmission and reflectivity measurements

The curved mirrors are coated with an HR coating, with a specified transmission of below 5 ppm. The high reflectivity is required for all mirrors except the input and output mirrors to minimize the transmission losses of the cavity of the OMC. Table 5.5 shows the measured transmission (T) of all curved mirror samples at an angle of incidence of 12.5 deg.

### 5.3.3 Non-cavity components

In addition to the cavity mirrors, a set of beam splitter and steering mirrors is used. As they are not part of the cavity itself and do not reflect the resonantly enhanced light field, their scatter performance is much less crucial. The micro-roughness of all surfaces was polished to an RMS of below 5 Å. Each beam splitter and steering mirror has an AR coating at its rear, designed for an angle of incidence of 45 deg. Each of these optics has a wedge angle of 0.5 deg. The substrate's dimensions are the same as the input and output mirror, with a front and rear surface of 20 mm by 30 mm and a thickness of 8 mm.

CHAPTER 5. AN OUTPUT MODE CLEANER FOR THE SUB-SQL  
INTERFEROMETER

Mirror	T in ppm
1	3.6
2	4.5
3	4.9
4	4.6
5	4.7
6	5.0
7	4.9
8	4.8
9	6.7
10	5.2

Table 5.5: Measured transmission for the ten possible curved HR mirrors for the OMC cavity.

### Steering mirrors

As can be seen in figure 5.8, the optical layout includes three steering mirrors. Each steering mirror was coated with an HR coating, transmitting less than 50 ppm at an angle of 45 deg. The measured transmission of each of the steering mirror samples can be seen in table 5.6.

### Beam splitter

There are two different kinds of beam splitters installed on the OMC breadboard. The first is the input beam splitter, reflecting most of the light towards the cavity. A high reflectivity is important, as all transmitted light adds to the total losses of the OMC. The transmitted light is detected on two QPDs, providing a fixed alignment reference for the OMC breadboard to the input beam. Secondly, there are two 50-50 beam splitters installed. One to split the light towards the two QPDs and the other to split the light towards the detection PDs located behind the cavity. The transmission of the input beam splitter and the reflectivity of the 50-50 beam splitter can be seen in table 5.7 and 5.8.

CHAPTER 5. AN OUTPUT MODE CLEANER FOR THE SUB-SQL  
INTERFEROMETER

Mirror	T in ppm
1	25
2	26
3	24
4	22
5	21
6	27
7	20
8	22
9	20
10	20
11	18
12	23
13	28
14	21
15	20

Table 5.6: Measured transmission for the 15 possible steering mirrors for the OMC breadboard.

Mirror	T in ppm
1	216
2	216
3	223
4	220
5	229

Table 5.7: Measured transmission for the five possible input beam splitter for the OMC breadboard.

### Beam dumps

The beam dumps are V-shaped constructions of BG39 filter glass, trapping and absorbing the incoming light. They are bolted to an INVAR 36 plate, which is glued to the OMC breadboard. The bolted connection allows for a replacement of the beam dumps with mirrors. This might be required if the reflectivity of the

CHAPTER 5. AN OUTPUT MODE CLEANER FOR THE SUB-SQL  
INTERFEROMETER

Mirror	R in %
1	49.7
2	49.5
3	49.4
4	49.4
5	49.3
6	49.5
7	49.6
8	49.2
9	49.3
10	49.4

Table 5.8: Measured transmission for the ten possible 50-50 beam splitter for the OMC breadboard.

detection PDs is contributing significantly to the total optical losses of the sub-SQL interferometer. An additional mirror could be used to reflect the light back onto the PD, strongly reducing its reflection losses.

### Quadrant PDs

As QPDs, FCI-InGaAs-Q3000 from OSI Optoelectronics were chosen. They provide a 3 mm diameter active surface and will be placed in aluminum-peek mounts, which are bolted to INVAR plates and glued to the breadboard. The mounts allow for horizontal and vertical alignment.

### Detection PDs

The final detection PDs used for the sub-SQL interferometer of the AEI 10 m prototype will be the IGHQEX3000 InGaAs PDs with a quantum efficiency of more than 99 %. They are large area PDs with a diameter of 3 mm bought from *Laser Components*. To reduce reflection losses, they are coated with an AR coating for an angle of incidence of 10 deg. High quantum efficiency is important, as any loss inside the PD counts as the total loss of the experiment.

### 5.3.4 Pairing of components

With the results from chapter 5.3.1 to 5.3.3, the best sets of optics for the OMC can be chosen. In the end, up to three full sets are required. Two OMCs are needed for balanced homodyne detection [FEF14] and a third OMC as a backup. This thesis focuses on setting up the first of the three OMCs, providing a guideline for the following ones.

The most important components are the two curved HR mirrors and the input and output mirrors forming the cavity. As explained in chapter 5.2, they define the parameters of the cavity and contribute strongly to the total losses of the OMC. First, a pair of input and output mirrors had to be chosen. Focusing on the measured scattering and reflectivity (see chapter 5.3.1) the sample numbers 1 and 2 provide extremely low TIS of well below 0.1 ppm (see figure 5.9 and table 5.2). Their transmission and thus reflectivity match up to a difference of  $0.01\% \pm 0.01\%$  (see table 5.3).

The HR curved mirrors provide a similar scatter performance (see figure 5.10 and table 5.4) and close transmission values (see table 5.5). There are two exceptions, which are clearly visible when comparing the BRDF and TIS. Sample number 10 shows a high, while sample number 6 shows a low scatter performance compared to the other samples. Promising the lowest TIS at a transmission of 5 ppm and below, the samples with the numbers 4 and 6 were chosen for the OMC.

The less important components, such as the beam splitters and steering mirrors, showed very similar performance (see table 5.6 to 5.8). They could be chosen freely for the OMC assembly. The first three steering mirror samples were used, as well as the first input steering sample and the first two beam splitter samples.

After choosing the desired components out of the available samples, the OMC can be assembled. The basic assembly process of the optics onto the breadboard is described in the following section.

## 5.4 Assembly of the OMC

The OMC for the sub-SQL interferometer of the AEI 10 m prototype is a quasi monolithic set-up. To reduce cavity length changes due to thermal noise, all components are glued to a fused silica breadboard. Optocast [EMI22] (a UV-curing

## CHAPTER 5. AN OUTPUT MODE CLEANER FOR THE SUB-SQL INTERFEROMETER

glue) is used with a thickness down to a few micrometers, bringing properties, such as the Q-factor, close to a monolithic set-up. The thickness of the gluing layer could be controlled by the amount of glue applied to the contact area. Further, fused silica provides a very low thermal expansion coefficient, reducing length drifts of the cavity caused by temperature fluctuations. As no corrections can be done after the gluing process, the initial positioning has to be as accurate as possible. This requires the OMC properties to be measured during the placement of each cavity component.

First, the sub-assembly of the curved mirrors, the PZT-rings, and their mounts is described, followed by the assembly of the cavity components onto the fused silica breadboard. After the assembly of the cavity, the non-cavity components are placed onto the breadboard.

### 5.4.1 Assembling the curved mirrors

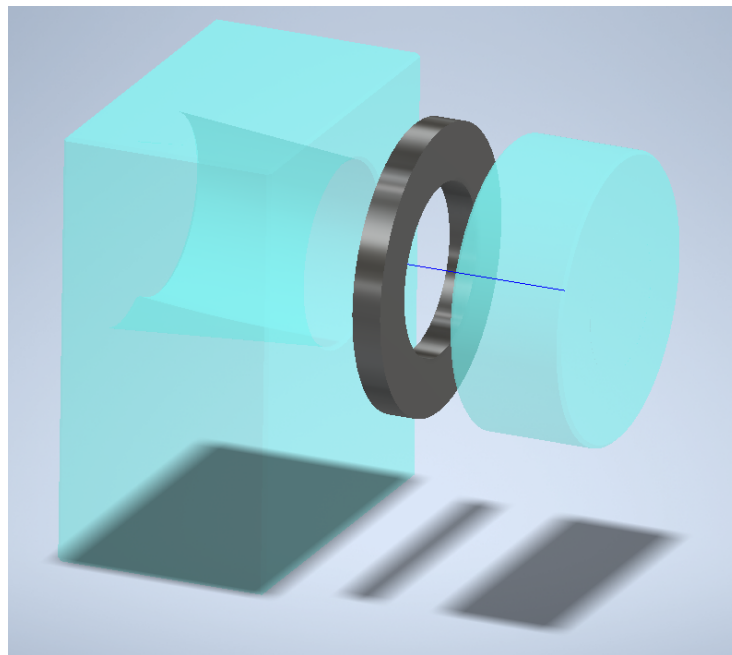


Figure 5.11: Curved mirror assembly for the OMC. The Curved mirror is glued to a ring-shaped PZT, which is glued to a fused silica substrate.

A 3-D model of the curved mirror assembly can be seen in figure 5.11. It consists of the curved mirror, which is a 20 mm diameter optic with a radius of curvature of

## CHAPTER 5. AN OUTPUT MODE CLEANER FOR THE SUB-SQL INTERFEROMETER

3.75 m. It is glued to a ring-shaped PZT (NAC2125 manufactured by CTS Ceramic Denmark) with an outer diameter of 20 mm and an inner diameter of 12 mm. The PZT has a height of 2 mm, providing a travel range of 2  $\mu\text{m}$ . Its maximum operation voltage is 200 V. The PZT is glued to a fused silica substrate, including a hole to cleanly transmit the laser beam leaking from the curved mirror. To glue the comparatively rough PZT surface to the fused silica components, EP30-2 epoxy was used. EP30-2 is a vacuum-compatible two-component epoxy provided by Master Bond Inc. To ensure a uniform thickness of the epoxy layer, bond line spheres with an 89  $\mu\text{m}$  diameter, made of fused silica, were used. Bond line spheres are well-defined spheres of identical size, acting as spacers within the epoxy layer.

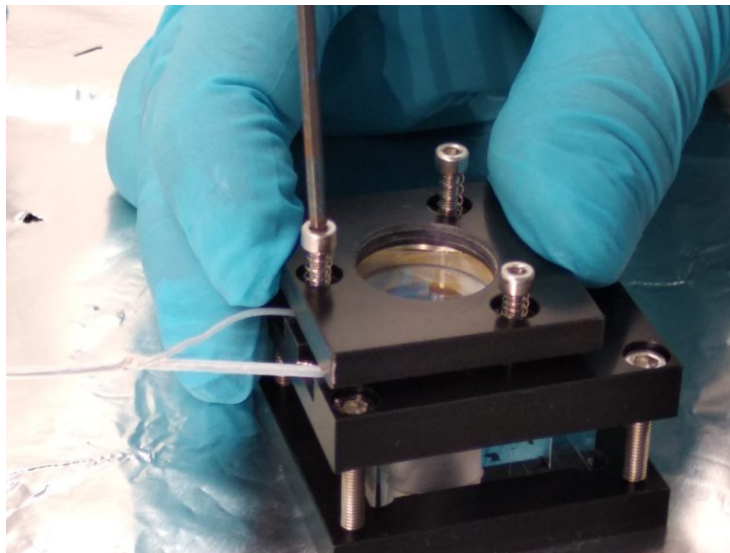


Figure 5.12: Photo of the gluing jig for the curved mirror assembly. Two POM parts hold the mounting substrate in place and provide contact points for both the PZT and the curved mirror. A third POM plate pushes onto the assembly during the curing process of the epoxy. Three spring-loaded pressure points are utilized to allow a homogeneous pressure distribution onto the assembly.

A polyoxymethylene (POM) gluing jig was used to assemble the three components. To ensure accurate placement of about 0.1 mm of the components relative to each other, they need to be constrained by a gluing jig. To avoid unequal pressure, ruining the parallel alignment of the three components towards each other, three spring-loaded pressure points were applied to the lid of the gluing jig. A picture of the gluing jig housing one of the curved mirror assemblies is shown in figure 5.12.

## CHAPTER 5. AN OUTPUT MODE CLEANER FOR THE SUB-SQL INTERFEROMETER

With the sub-assembly of the curved mirrors completed, the OMC cavity can be assembled on the fused silica breadboard, as described in the following section.

### 5.4.2 Assembling the OMC cavity

For accurate placement of the optic components onto the breadboard, a brass template was used. The breadboard covered by the template can be seen in figure 5.13. The position of each optic is defined by touching three steel spheres attached to the template. Additional micrometer screws are used as contact points for the curved mirror sub-assemblies. These can be used to tune the length of the cavity, as well as the angles of the curved mirrors.

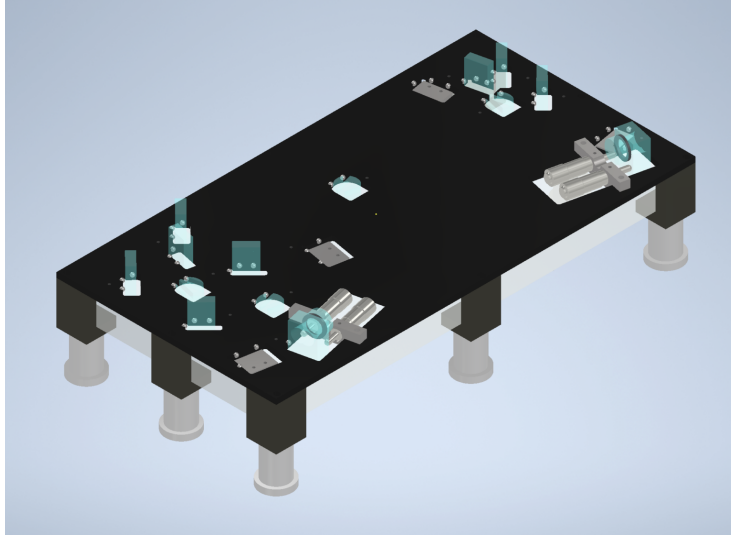


Figure 5.13: Fused silica breadboard covered by a template allowing a precise optic placement and defined positions. Micrometer screws are used as contact points for the curved mirror assemblies to tune their angle and the cavity length.

In the first step, all cavity mirrors and the input steering mirror are placed at their respective positions. This is followed by an alignment of the curved mirrors using the micrometer screws on the template. The alignment is done within a measurement set-up, which allows locking of the cavity to a laser. The set-up is used to measure the cavity parameters, such as the FSR, the TMS, the transmission function of the cavity and the cavity losses. It can be seen in figure 5.14.

Here, a laser beam with a wavelength of 1064 nm is sent through an FI, followed by a power adjustment stage consisting of a  $\lambda/2$ -plate and a PBS. A fiber is acting as

CHAPTER 5. AN OUTPUT MODE CLEANER FOR THE SUB-SQL INTERFEROMETER

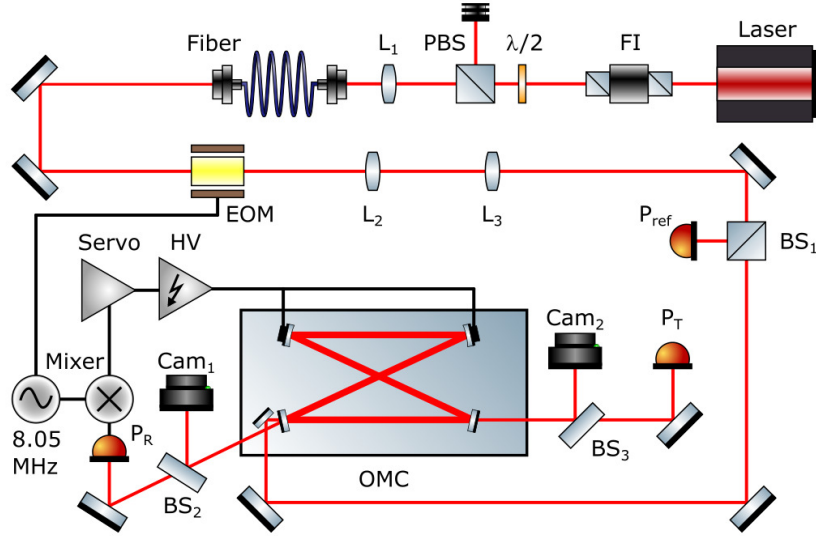


Figure 5.14: Measurement set-up to measure the OMC parameters during the assembling process. A laser beam is sent through an FI and a power adjustment stage, followed by a fiber. An EOM imprints phase modulation sidebands onto the beam. Two lenses ( $L_1$ ,  $L_2$ ) and two steering mirrors are used to mode-match and align the beam to the cavity. The beam enters the cavity after a power reference measurement at  $P_{ref}$ . The reflected beam is observed with a camera ( $Cam_1$ ) and measured with a PD ( $P_R$ ). A local oscillator signal of 8.05 MHz and the PD signal are mixed and sent through a servo into a high voltage amplifier. The output actuates onto the PZTs attached to the curved HR mirrors. The transmitted beam is observed at a second camera ( $Cam_2$ ) and measured by a PD ( $P_T$ ).

a pre-mode cleaner, improving the mode profile of the laser beam. After imprinting phase modulation sidebands onto the laser beam, a pair of lenses is used to match the laser beam to the OMC cavity. The input power is measured using a reference power meter ( $P_{ref}$ ) before two steering mirrors align the input beam towards the OMC cavity. The reflected beam is used to lock the cavity with the Pound-Drever-Hall technique [Dre+83] by either actuating onto the PZTs attached to the curved mirrors or at the laser frequency. The transmitted laser power is detected with a power meter ( $P_T$ ), allowing to measure the transmission in dependence on the laser frequency. Two cameras are used to observe the mode picture of the laser beam. One is located in the reflected and the other in the transmitted path.

The measurement set-up is crucial to ensure the correct placement of all components and to tune the cavity length and thus FSR of the cavity. Further, the

curvature and alignment can be checked, as well as the cavity losses can be measured, allowing to replace components if necessary. After all required components were placed and the cavity parameters and performance were confirmed, the components were glued to the breadboard. A UV curing epoxy was used. The epoxy is vacuum compatible and reaches a layer thickness below a few  $\mu\text{m}$ .

After a brief overview of the OMC suspension in the following section, the final OMC performance, including cavity parameters and losses, is presented in the sections 5.6.2 and 5.6.3.

## 5.5 OMC suspension design

As explained in chapter 1.2.2, the seismic isolation of several optical core components of the sub-SQL interferometer is crucial for its performance. The suspension and thus seismic isolation of the OMC is of importance for two reasons. Firstly, the excitation of internal modes of the breadboard and hence misalignment and length change of the OMC cavity should be reduced. Further, the counter-propagating mode (see chapter 5.2.4) of the OMC is directly steered and mode-matched back towards the sub-SQL interferometer. There it interferes with the light field of the MI, causing unwanted power fluctuations and thus noise at the output port.

In the case of the OMC, a two-stage suspension fulfills the requirements, as the counter-propagating light field is very weak. The internal modes of the OMC breadboard are above the measurement band, thus requiring even less than a two-stage suspension. Further, a two-stage suspension allows for sensing and actuation at the upper mass, damping the suspension movement at the resonance frequencies (see chapter 4.2.4), while noise caused by the sensors and actuators is reduced at the second suspension stage. The resonance frequencies of degrees of freedom coupling into the output port of the sub-SQL interferometer need to be well outside the measurement band.

This section provides an overview of the suspension design. The suspension parameters can be found in the appendix B.5.

### 5.5.1 Two-stage suspension design

Starting with the design of the second stage, which is defined by the breadboard shape and size and the distribution of optical components (5.2.5), the suspension can be designed from the bottom to the top. With the physical properties, such as weight and moments of inertia of the second stage, a first stage can be designed. The physical properties are kept similar, allowing a sufficient coupling between the stages for efficient extraction of motion at the upper stage (see chapter 4.1).

#### Second stage design

The second stage's physical properties are dominated by the breadboard design. The fused silica breadboard itself accounts for about 95 % of the second stage's mass. As the optical components are close to the breadboard surface, the total mass and moments of inertia are thus mostly defined by the breadboard. The horizontal size (x-y-plane) is dictated by the optical layout, with a width of 200 mm and a length of 400 mm. The thickness of the breadboard is chosen to increase the frequency of all internal resonances of the breadboard to above 1000 Hz and thus outside the measurement band of the sub-SQL interferometer. A finite element and modal analysis with Autodesk Inventor showed a required thickness of 30 mm.

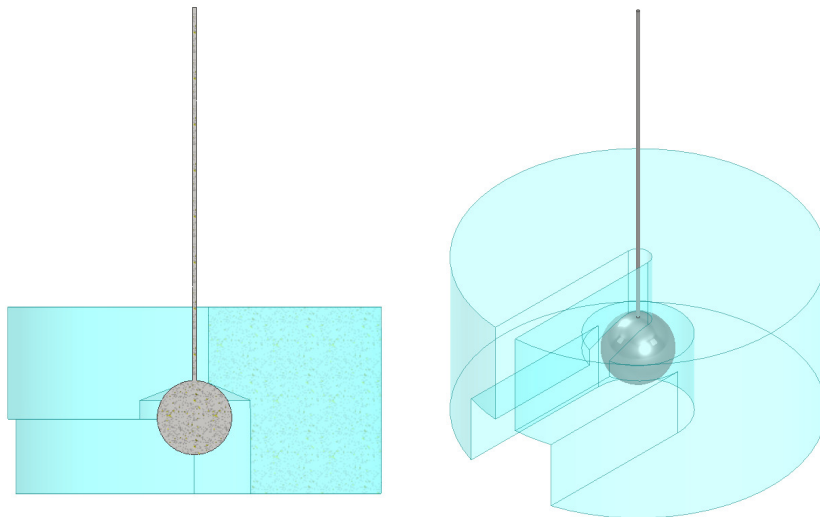


Figure 5.15: A 4 mm steel sphere is attached to the suspension wire and pushed into a fused silica mount. The sphere is held in place by a cone-shaped interior of the mounting structure. The cross-section is shown on the left and the 3 D model on the right.

## CHAPTER 5. AN OUTPUT MODE CLEANER FOR THE SUB-SQL INTERFEROMETER

To suspend the breadboard, additional wire mounts are required. As the optical layout does not allow the symmetric placement of these atop the breadboard, the breadboard is suspended upside-down. The wire mounts can be seen in figure 5.15. They are cylindrical fused silica parts with a cone-shaped 6 mm diameter hole at the bottom. A 1.5 mm hole for the suspension wire connects the top with the cone-shaped hole. The suspension wire with a radius of  $100\ \mu\text{m}$  is welded to a 4 mm diameter steel sphere, which can be slid into its resting position at the end of the cone-shaped hole. A symmetrical placement of the wire mounts around the center of mass (CM) is desired to reduce cross-coupling from different degrees of freedom. Further, it allows an even mass distribution onto each of the spring blades used for the vertical seismic isolation. As it is difficult to find a fitting position for the wire mounts next to the optical components, they are attached to the opposite side of the breadboard. This kind of set-up is also used at the aLIGO [Ara+13] and offers additional space to add strain reliefs for the PD wiring.

### First stage design

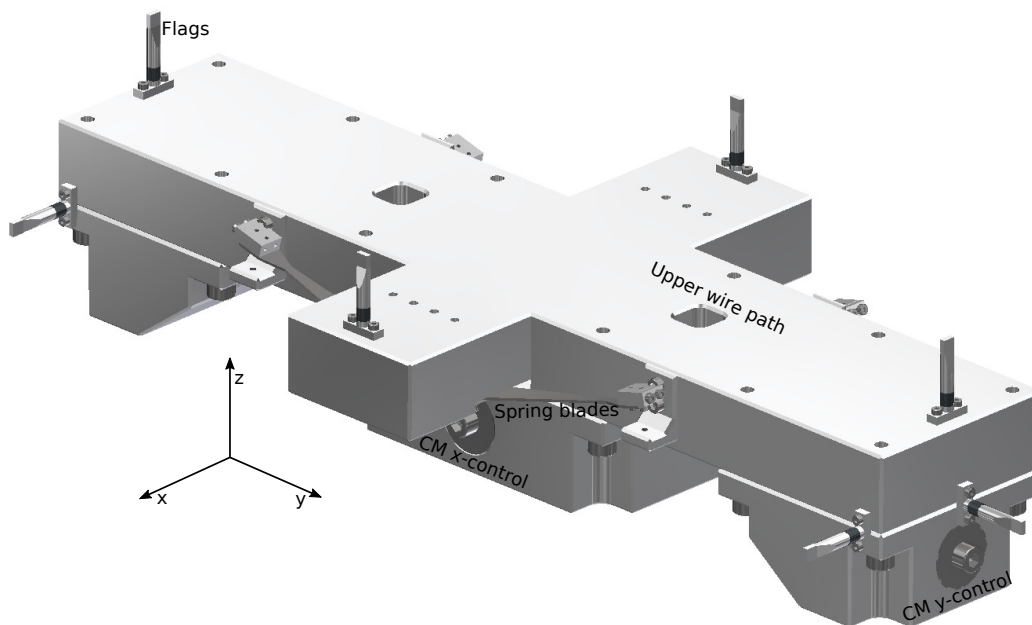


Figure 5.16: First stage design for the OMC suspension. Showing shape, location of flags for optical sensors and coil actuators, spring blade and wire positions, as well as threaded push rods for CM alignment.

## CHAPTER 5. AN OUTPUT MODE CLEANER FOR THE SUB-SQL INTERFEROMETER

The first suspension stage is designed to provide similar physical properties as the second stage. It is manufactured from aluminum with inserted threaded rods made from stainless steel. The rods can be used to tune the center of mass of the upper mass, allowing for some DC alignment of the pitch and roll degree of freedom (see chapter 4.2.2). Four spring blades made from stainless spring steel are used as a second vertical seismic isolation stage, connecting to the suspension wires leading to the second suspension stage. Aluminum flags and magnets are attached to the first suspension stage to allow the installation of BOSEM (see chapter 4.2.4) sensors and actuators. The CAD model of the first suspension stage can be seen in figure 5.16.

### Suspension cage and top design

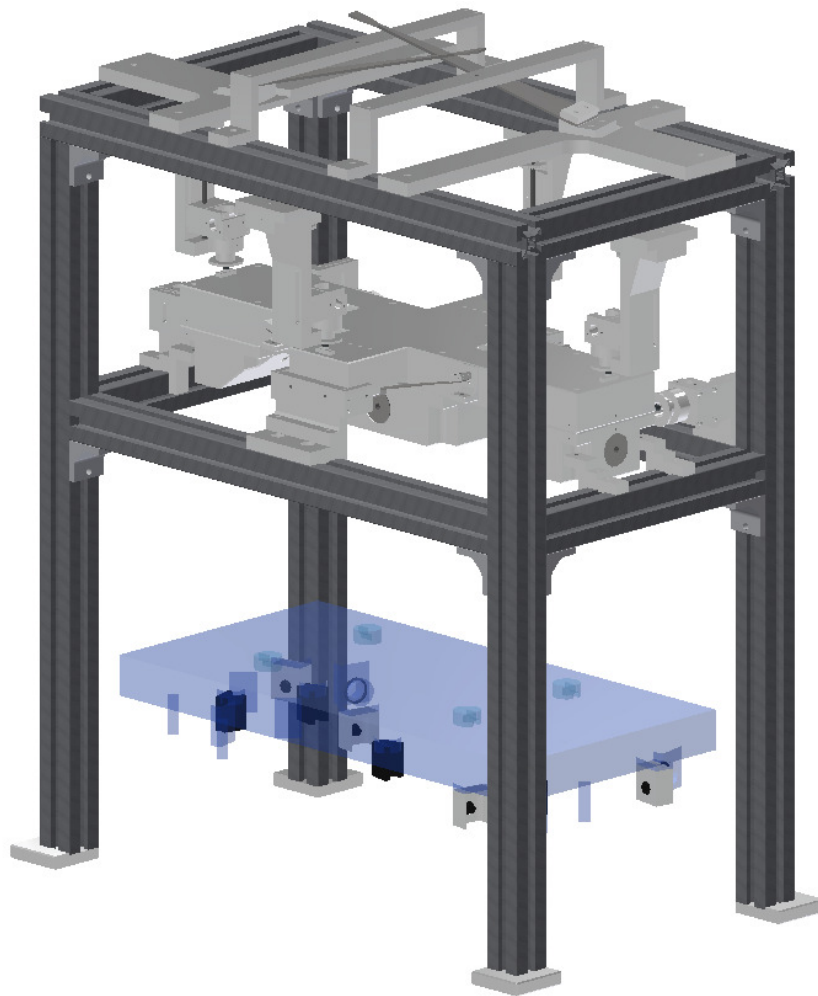


Figure 5.17: CAD model of the full OMC suspension.

## CHAPTER 5. AN OUTPUT MODE CLEANER FOR THE SUB-SQL INTERFEROMETER

The suspension cage is made from 30 mm by 30 mm aluminum profiles, providing a relatively lightweight, rigid frame. BOSEM sensor and actuators are attached to the suspension cage, allowing sensing and actuation of the first suspension stage. As described in chapter 4.2.4, this can be used to actively dampen the suspension resonances and control the DC position of the first and second suspension stage. A pair of spring blades are installed at the top of the suspension, acting as the first vertical seismic isolation stage. The CAD model of the full suspension can be seen in figure 5.17. In its final version, the bottom part will be covered by additional plates to avoid stray light entering the OMC set-up.

### 5.6 Final OMC performance

The evaluation of the final performance of the OMC for the sub-SQL interferometer of the AEI 10 m prototype includes the measured cavity parameters, the estimated mode filter performance and the measured losses.

#### 5.6.1 Measured cavity parameters

Using the set-up shown in figure 5.14 the cavity parameters can be measured. First, a measurement of the cavity length and FSR can be done by ramping either the cavity length or the laser frequency while measuring the transmitted power of the cavity. A cavity length change by more than one wavelength (1064 nm) or a frequency change of more than one FSR was displayed with an oscilloscope for each ramping cycle. The distance between two transmission maxima of the aligned cavity is the FSR. The well-defined sidebands created by the EOM can be used to calibrate the time axis of the ramp to a frequency axis. The resulting FSR can be converted directly into the cavity length. The error of this measurement was dominated by the non-linearity of the length and frequency actuators. To compensate for the non-linearity, the cavity was strongly misaligned, leading to several HOM being resonant inside the cavity. Each peak representing a HOM showed its own sidebands, allowing to measure a calibration function of the actuator voltage to the actual cavity length change. The stochastic error of several calibration measurements resulted in the final standard deviation of the measured FSR shown in table 5.9.

By a small horizontal and vertical misalignment of the input beam axis and

CHAPTER 5. AN OUTPUT MODE CLEANER FOR THE SUB-SQL  
INTERFEROMETER

the cavity, the horizontal and vertical TMS can be measured. A misalignment of the input beam towards the cavity causes the input beam to consist of the TEM<sub>00</sub> and higher HOMs in the basis of the cavity. When scanning the cavity length, the HOMs get excited by the incident laser beam. The TMS is the frequency deviation between the transmitted peaks of two successive orders of HOMs. Similar to the FSR measurement, the mode spacing can be measured by scanning the cavity length. The transmitted power can be measured with an oscilloscope while applying a voltage ramp to the cavity actuators. The time-dependent transmission can be converted to frequency using the sidebands or the now known FSR. A horizontal misalignment is used to measure the horizontal, and a vertical misalignment can be used to measure the vertical TMS. The measurement error is calculated in the same way as for the FSR measurement. The TMS can be used to calculate the curvature of the HR mirrors and astigmatism using the ABCD-matrices introduced in chapter 5.1.1.

The finesse of the cavity can be calculated by measuring the FWHM and FSR of the cavity and using equation 5.13. For this purpose, the calibrated cavity transmission of the FSR measurement can be used. The measurement error of the FSR measurement and its calibration can be used to determine the measurement error of the finesse.

Parameter	Value	Error	Unit
FSR	244.69	0.42	MHz
Length	1.225	0.002	m
TMS <sub>H</sub>	46.04	0.08	MHz
TMS <sub>V</sub>	44.96	0.09	MHz
RoC <sub>H</sub>	3.755	0.001	m
RoC <sub>V</sub>	3.758	0.001	m
Finesse	190	1	-

Table 5.9: Measured OMC cavity parameter.

The measured parameters are well within the expectations, except for the finesse being significantly lower. A finesse of 229 was planned for the OMC cavity, which is about 18 % above the measured finesse. The reduced finesse of the cavity will worsen the mode filter performance. It is partially caused by a higher transmission

through the in and output mirror than anticipated.

A transmission of 1.35 % was defined as the design value for the in and output mirrors of the OMC cavity to reach a finesse of 229. The actual transmission of these components was measured to be 1.41 % (see table 5.3), resulting in an expected finesse of 221. The measured finesse of 190, however, corresponds to a transmission of 1.64 %. The most plausible explanation for the discrepancy is an error in the reflectivity measurements of the in and output mirrors. Such an error might be caused by, e.g., measuring at a wrong angle of incidence or applying a wrong calibration to the measured reference power. Other factors influencing the finesse, such as high transmission and scatter losses, can be excluded, as they would require increasing the losses measured in section 5.6.3 by a factor of 300.

In the next section, the calculated mode filter performance can be seen, including the measured finesse value of 190.

### 5.6.2 Estimated mode filter performance

The output mode profile of the sub-SQL interferometer would be required to calculate the exact mode filter performance. As described in section 5.2.2, the output mode profile of the aLIGOs was used to provide an estimate of the mode filter performance. For the final calculation, the measured cavity parameters shown in table 5.9 were used. The mode filter performance as transmitted HOM power normalized to the transmitted TEM<sub>00</sub> power can be seen in figure 5.18 in dependence on the RoC and cavity length.

The final result shows a transmission of 0.17 %  $\pm$ 0.002 % HOM content relative to the TEM<sub>00</sub> mode. This needs to be compared to the value of 0.1 %, which was aimed for during the design phase, and the requirement of 1 %. A safety factor of 10 was previously (see chapter 5.2.3) implemented to compensate for inaccuracies of the optical components, non-perfect cavity assembling and a differing output mode profile of the sub-SQL interferometer. After the assembling process, a factor of 6 remains for a differing mode profile.

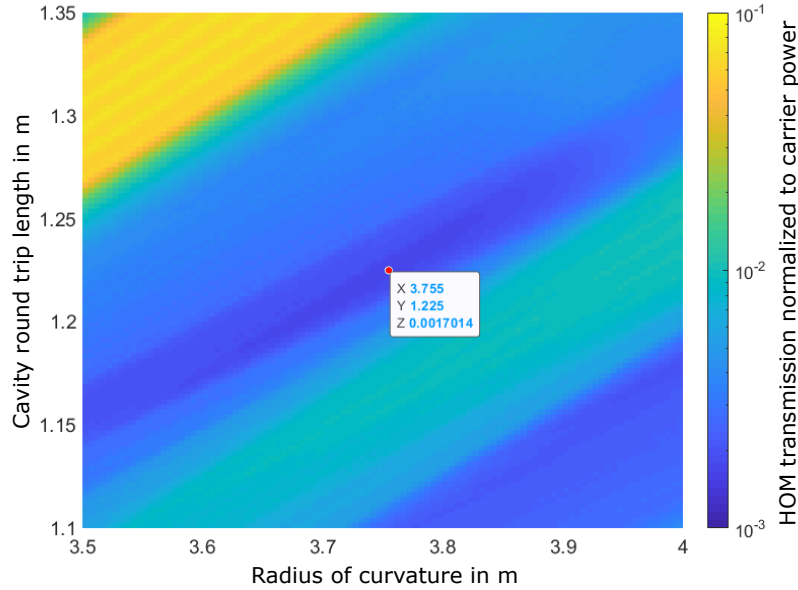


Figure 5.18: Calculated mode filter performance of the assembled OMC for the sub-SQL interferometer. The aLIGO output mode profile was used for the calculations. The red dot indicates the possible errors of the cavity length and the radius of curvature.

### 5.6.3 Loss measurement

A high focus was placed on the reduction of losses for the OMC design of the sub-SQL interferometer of the AEI 10m prototype. To reduce the losses of the OMC, a relatively low finesse was chosen, which turned out even lower than expected. Further, the BRDF and thus TIS was measured to find the best optics and ensure a well-cleaned surface. A simulation with the Finesse 2 software was made, predicting the cavity losses to be 0.09 % to 0.14 %. These are dominated by the 5 ppm transmission of the HR mirrors and the 1 ppm to 3 ppm absorption losses within the coatings. Additionally, the input steering mirror on the OMC breadboard adds another 0.022 % loss by transmitting a part of the light for alignment purposes. The calculated losses do not include losses caused by the photodiodes or a mode mismatch of the input beam, as these are individual loss sources for the total loss budget of the sub-SQL interferometer.

For a first loss measurement, a mode-matching of 94 % of the input beam towards the cavity was achieved. The high mode mismatch was caused by the poor quality

## CHAPTER 5. AN OUTPUT MODE CLEANER FOR THE SUB-SQL INTERFEROMETER

of the input beam and could be improved to a mode-matching of close to 97 % with the installation of a fiber, acting as input mode cleaner (as seen in figure 5.14). With the improved mode-matching, the second set of loss measurements could be taken. The measured transmission function of the cavity in dependence on the frequency deviation from the cavity resonance can be seen in figure 5.19. It is compared to a simulated cavity performance using the cavity parameters shown in 5.9. The missing 2 % of the mode-matching are still originating from imperfections of the input beam, caused or not filtered out by the optical fiber.

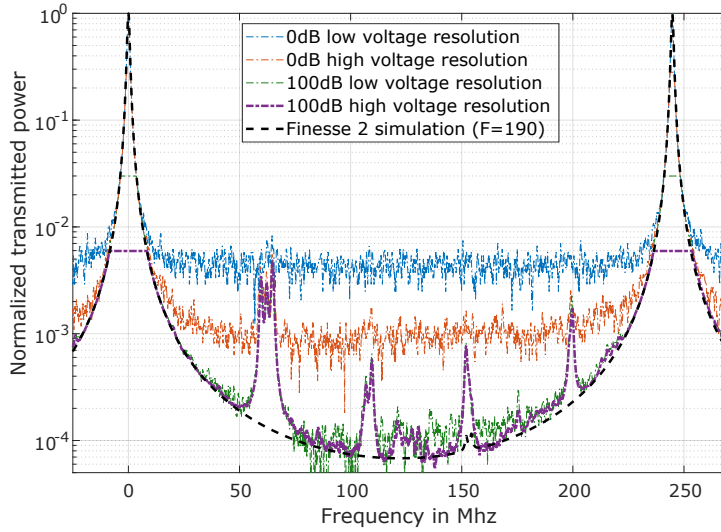


Figure 5.19: Measured cavity transmission in dependence of the frequency deviation from resonance. Different PD and oscilloscope gain settings were used to avoid saturation and display the full power range. The black dashed line shows the simulation of the expected cavity transmission function simulated with Finesse 2.

To calculate the optical losses caused by the OMC, the input power ( $P_{in}$ ), the reflected power ( $P_R$ ), and the transmitted power ( $P_T$ ) need to be measured. The reflected power includes the rejected HOMs of the non-perfect input beam, as well as the phase modulation sidebands. The transmitted power is strongly dominated by the  $TEM_{00}$  mode. When comparing the transmitted power to the input power excluding the HOMs and sidebands, only the losses of the  $TEM_{00}$  mode remain. These are the optical losses of interest for the sub-SQL interferometer. Equation 5.17 shows how the optical loss is calculated.

CHAPTER 5. AN OUTPUT MODE CLEANER FOR THE SUB-SQL INTERFEROMETER

$$Loss = 1 - \frac{P_T}{P_{in} - P_R} \quad (5.17)$$

Excluding the phase modulation sidebands, equation 5.17 does not account for any TEM<sub>00</sub> mode content, contributing to the reflected power. The TEM<sub>00</sub> mode could, e.g., be reflected from the cavity in case of an impedance mismatch, i.e., a mismatched reflectivity of the in and output mirror, adding not accounted optical losses. To show that the reflected power is purely composed of HOMs and phase modulation sidebands, the HOM and sideband content in the input beam can be deduced from the cavity transmission scan (see figure 5.19). The summed power of HOMs and sidebands can then be compared to the reflected power of the locked cavity. The combined HOM and sideband content was calculated to be 2.86 %. This compares well to a reflected power of 2.9 % measured after the measurement of the cavity transmission. Nonetheless, this approach can be prone to errors, as it is hard to account for all of the smaller peaks in the cavity transmission scan. Further, a small drift between the input beam axis and the cavity can change the power in the first-order HOMs. In the future, a PMC could be used to clean the input beam and provide a loss measurement that is less affected by the input beam quality.

Table 5.10 shows the measured losses of the OMC cavity. The first three measurements were done with a mode-matching of 94 %, while the second set of measurements was done with a mode-matching of 97 %. As the reflected power is taken into account, the mode-matching has no direct influence on the losses of the TEM<sub>00</sub> mode. For each of the input, reflection, and transmission power measurements, the same photodiode was used to avoid calibration errors. The dominant measurement error was caused by the placement accuracy of the photodiode for each power measurement. The measurement error increased for the fourth to sixth measurement due to an increased measurement error of the weaker reflected light power at an increased mode-matching.

The final average optical loss of the OMC can be calculated to be 0.10 % with an average error of  $\pm 0.40$  %. This compares well to the expected, simulated optical loss of 0.11 % to 0.16 %, though the measurement error surpasses the results by a

CHAPTER 5. AN OUTPUT MODE CLEANER FOR THE SUB-SQL  
INTERFEROMETER

Loss measurement	Value	Error	Unit
1	0.00	$\pm 0.33$	%
2	0.18	$\pm 0.33$	%
3	-0.11	$\pm 0.33$	%
4	0.13	$\pm 0.46$	%
5	0.39	$\pm 0.46$	%
6	0.01	$\pm 0.46$	%

Table 5.10: Measured TEM<sub>00</sub> losses of the OMC. The measurement error was dominated by the placement accuracy of the photodiode.

factor of four. The final result is even below the set goal of 1 % optical losses in the OMC. Compared to the OMC losses of the gravitational wave detectors like aLIGO and Geo600, which show optical losses above 2 % [Lou+21; Ara22], an improvement by more than an order of magnitude could be achieved.

## Chapter 6

# Summary and outlook

The first chapter of this thesis introduces the AEI 10 m prototype as a testbed for techniques to improve current and future gravitational wave detectors. Starting with an overview of the measurement principle of gravitational wave detectors, different limiting noise sources are presented. These noise sources will also limit the sensitivity of the sub-SQL interferometer of the AEI 10 m prototype. A general overview of the AEI 10 m prototype and its subsystems is given alongside their role in suppressing the presented noise sources.

In chapter two, the thickness uniformity of an AlGaAs coating is measured alongside a lower limit for its laser-induced damage threshold (LIDT). The initial set-up allows the measurement of an optic's reflectivity map. The reflectivity map is converted into a map displaying the thickness uniformity using a previously derived set of parameters. Here, the thickness uniformity of a crystalline AlGaAs coating could be measured down to an RMS of  $0.41 \pm 0.05$  nm. This is similar to that of the state-of-the-art, non-crystalline coatings used in gravitational wave detectors. In a second set-up, an 85 W laser was focused down to a spot size radius of  $9.2 \mu\text{m}$ , without damage to the coating. This resulted in an intensity of  $64 \pm 5$  MW/cm<sup>2</sup>, defining a lower limit for the LIDT of AlGaAs coatings.

In the third chapter, a device to measure the BRDF of optical surfaces is presented. The design of the set-up was based on a design by Joshua Smith at the California State University Fullerton. This thesis presents a modified version, increasing the measurement range towards lower scatter angles. A new readout scheme is introduced, combining measurements at different exposure times to increase the sensitivity. The scatter measurement device is later used to characterize components

## CHAPTER 6. SUMMARY AND OUTLOOK

for the OMC. It was able to measure the BRDF of high-quality optics with a total integrated scattering of below 0.1 ppm. A graphical user interface was later developed to decrease the computation time and simplify the execution of measurements. A possible future upgrade should include an increase to the laser power. A 100 mW laser could be attached to the set-up via a fiber, which would increase the sensitivity by about a factor ten. This would either allow more accurate measurements or a strongly reduced measurement time.

The fourth chapter presents the design of the beam splitter and its triple suspension for the sub-SQL interferometer of the AEI 10 m prototype. The optical requirements were first defined, followed by weight and space constraints to fit within the sub-SQL interferometer, defining the shape of the beam splitter's substrate. A special focus is placed on the separation of arising ghost beams. This includes the use of a split coating on the front surface of the beam splitter and the design of an anti-reflective coating, covering multiple angles of incidence. The design for a triple suspension for the seismic isolation of the beam splitter was then presented, focusing on the design process, followed by a comparison of the suspension's simulated and measured resonance frequencies. A further simulation showed that the BS suspension fulfilled the requirements for the sub-SQL interferometer. Both the optic and suspension will soon be implemented into the sub-SQL interferometer. An ongoing collaboration with the Vrije Universiteit Amsterdam foresees the installations of homodyne quadrature interferometers (HoQIs) onto the suspension, measuring the motion of its second stage. The hope is to demonstrate that HoQIs will provide sufficient performance to be applicable to gravitational wave detectors.

In the fifth chapter, the design, assembly and testing of an output mode cleaner for the sub-SQL interferometer is presented alongside the design of its suspension. The requirements and design of the sub-SQL interferometer's OMC were determined based on a desired cavity mode filtering specification. The design and assembly focused on the reduction of losses inside the OMC cavity while maintaining sufficient mode filter performance. A double suspension was designed to seismically isolate the breadboard of the OMC assembly. In the end, losses of  $0.1 \pm 0.4$  % could be achieved, which were more than an order of magnitude below the losses of OMCs installed in current gravitational wave detectors. Sufficient filtering performance in the sub-SQL interferometer could be predicted using measurements of the OMC parameters and

## CHAPTER 6. SUMMARY AND OUTLOOK

the expected output mode profile. In the near future, the suspension assembly will be completed by suspending the OMC breadboard as its second suspension stage, and it can later be installed into the AEI 10 m prototype's vacuum chamber. At that point, the suspension's performance can be evaluated to implement active damping loops. Once the sub-SQL interferometer is operational, its output mode profile can be measured to fully determine the OMC's mode filter performance. A second OMC will then be built to facilitate balanced homodyne detection, unlocking access to a wider variety of sub-SQL techniques.

# Appendix A

## Suspension blade springs

The triple-suspension design for the BS (see chapter 4.2.5), as well as the double-suspension design for the OMC (see chapter 5.5) require blade springs for their vertical isolation stages. Throughout my PhD time, we chose two different design approaches for the blade springs. The design approach for the BS suspension was pre-bend blade springs made from maraging (aged martensite) steel. These blade springs bend upwards and flatten under the load of the suspended masses. For the OMC suspension, we decided to use stainless steel 420. Further, the blades are originally flat and bend downwards under the load of the suspended masses. The blade springs are attached to the suspension under an angle of 15 deg, i.e., pointing upward to compensate for the bending. In this appendix, I will write about the design choices, why we made them, what benefits they hold, and what the drawbacks are. Please note that the consideration of the following pros and cons include rough estimates and knowledge gained by discussions with, e.g., Prof. Kenneth Strain, and a relatively broad but not deep research into material science.

### A.1 Pre-bend vs flat

First of all, and to my knowledge, there is no strong scientific reason to combine the pre-bend blade design with a specific material. They rather are two different design choices, and it is possible to use, e.g., pre-bend stainless steel 420 blades, as well as flat maraging steel ones, and vice versa. Nonetheless, the bending process itself differs depending on the material.

Spring steel, e.g., stainless steel 420, is very brittle, and thus plastic deformation might lead to small fractures in the material, ruining the blade spring properties. Spring steel blades can be manufactured by bending the rolled alloy in a strongly

## APPENDIX A. SUSPENSION BLADE SPRINGS

heated state, as it receives its spring steel properties during the following cooling and quenching processes. As we did not use any pre-bend stainless steel 420 blade springs, I'm not sure about its availability and costs in small quantities.

Maraging steel provides a much higher ductility, allowing for plastic deformation without causing fractures. The material can be shaped and deformed to fit the requirements, followed by a careful heat treatment to distress the material. This makes the pre-bending process supposedly easier and less prone to errors. Ordering pre-bend maraging steel blades turned out to be expensive combined with a long lead time, despite providing the costly material ourselves.

The pre-bending leads to flat blade springs under the load of the suspended masses. This minimizes the coupling from vertical to horizontal motion of the blade spring tip, i.e., coupling from the vertical and roll to the side DOF (see 4.9 for the definition of the DOFs). Flat blade springs, on the other hand, are easier and cheaper to purchase. All blades should be tested under their final load to find matching blades with similar properties. More pre-bend blades are required to find matching pairs, as the pre-bending process does not seem to be perfectly accurate.

### **A.2 Maraging steel vs. stainless spring steel**

The most important property of the blade springs is the resulting vertical resonance frequency of the suspension. Usually, we want to achieve low suspension resonance frequencies to decrease all suspension motion above. The resonance frequency is inversely proportional to the vertical deflection of the blade. Thus, we can lower the vertical suspension resonance frequency by lengthening or thinning the blade design.

Lengthening a blade spring strongly increases its weight and thus lowers the frequency of the resulting center of percussion plateau. Further, spatial constraints often limit the blade spring's length. Thinning a blade spring, on the other hand, decreases the weight and thus increases the frequency of the center of percussion plateau. It reduces the vertical resonance frequency of the suspension by increasing the deflection of the loaded blade spring.

By thinning the blade spring, we increase the stress on the blade material as we reduce the bending radius. Different materials provide differing yield strengths

## APPENDIX A. SUSPENSION BLADE SPRINGS

allowing for more or less stress before plastic deformation or fracture. Additionally, the closer the stress of material comes to its yield point, the higher the probability of dislocation avalanches becomes. Dislocation avalanches can arise when defects in a material's atomic lattice shift under stress. These shifts can cause other lattice defects to shift, causing an avalanche. The avalanche vertically dislocates a part of the blade spring lattice leading to a vertical impulse-like motion.

By using impurity atoms inside a material, the movement of the defects inside the atomic lattice can be restricted, allowing higher stress before the number of dislocation avalanches becomes crucial.

Maraging steel provides a yield strength of up to 2 GPa. We reduce the probability of defect avalanches by restricting the maximum stress to about 50-60 % of the yield strength, as the maraging steel is relatively prone to shifting lattice defects. Stainless spring steel 420 promises up to 1.8 GPa (depending on the manufacturer). Here, we restrict the maximum stress of the blade spring to 30 % of the yield strength. With these estimates, we can design maraging steel blades with about twice the stress compared to the stainless spring steel 420 blades.

Another important property of the blade spring is its thickness uniformity. A varying thickness can lead to an uneven bending of the blade under load. Here, maraging steel needs to be post-processed, and precision lapped to the desired thickness. Stainless spring steel 420 is often used as chiming material and thus easily available in different thicknesses with a sufficient thickness uniformity.

### A.3 BS suspension blade springs

When designing the BS suspension during the first year of my PhD, the usage of pre-bend maraging steel blades was quite common in the gravitational wave detector community. Later flat blade springs made from stainless spring steel were chosen for several suspension designs. The BS suspension required two different blade spring designs. The blade springs for the first vertical isolation stage were chosen among old residual pre-bend maraging steel blade springs of the GEO600 detector. The blades springs for the second vertical isolation stage were designed with Ansys.

The length of the blade springs was restricted to 10 cm, as they were installed in the first suspension stage. We aimed for a second vertical suspension resonance

## APPENDIX A. SUSPENSION BLADE SPRINGS

frequency around 3 to 4 Hz. The resulting blade spring design had a thickness of  $0.83 \pm 0.01$  mm, requiring a pre-bending curvature of 195.18 mm to be flat under the load of the second and third suspension stage. The curvature and the stress under load were simulated with a finite element analysis in Ansys. The results of the deflection simulations can be seen in figure A.1 with a maximum stress of about 400 MPa and a resonance frequency of 3.18 Hz. The characterization of the blades springs was done with camera pictures calibrating their pixels to the length of the blade spring. The characterization can be seen in figure A.2 and table A.1. The drawing, including all dimensions and tolerances, is shown in figure A.3. It was created in a joint effort with the School of Physics & Astronomy at the University of Glasgow.

I used table A.1 to pair the four blades installed in the BS suspension. The most important parameters (for parameter definition see figure A.2) are  $h$  and  $\Delta h$ . The vertical offset under load is defined by  $h$ . It eventually results in offsets in the roll or pitch DOFs, and if chosen very poorly in differing stresses applied to the individual blades resulting in varying blade deflections and thus vertical suspension resonance frequencies.  $\Delta h$  is the blade deflection at the tip defining the resonance frequency of the vertical suspension resonances. Here, blades 4, 10, 11 and 14 were chosen. Their blade deflection is within 2 % of each other, and the vertical offsets agree very well. The blades 4 and 14 and 10 and 11 were placed together, as a roll offset is of less interest than a pitch offset.

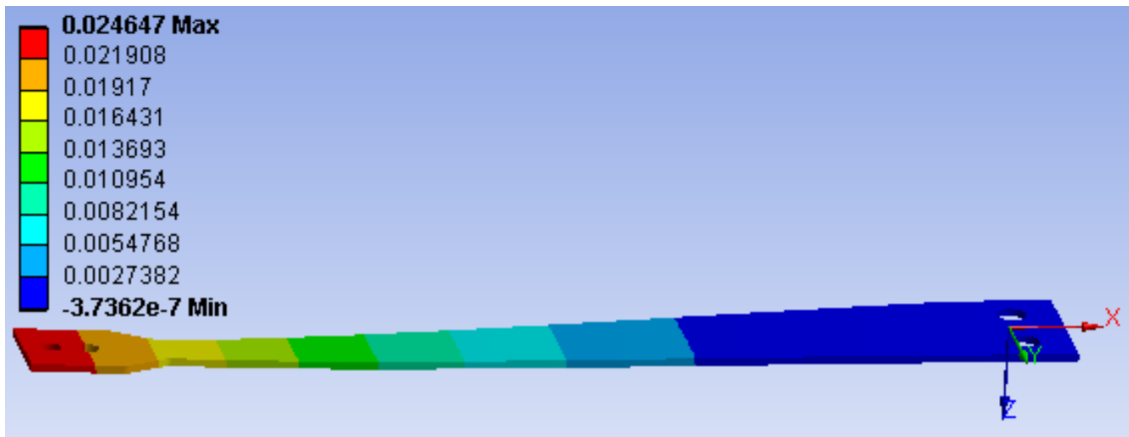


Figure A.1: Here, the vertical deflection of the BS blade spring under load in units of m can be seen.

## APPENDIX A. SUSPENSION BLADE SPRINGS



Figure A.2: Here, the BS suspension's blade spring characterization using a camera picture can be seen. Parameter values for the different blade springs are shown in table A.1

Blade	s in mm	h in mm	$\Delta h$ in mm	L in mm	r in mm
1	22.12	-0.09	22.35	100.02	91.10
2	22.22	-0.72	22.45	100.03	91.47
3	22.49	0.05	22.73	100.00	91.22
4	22.05	0.05	22.27	100.00	91.19
5	22.62	-0.74	22.85	100.03	91.39
6	22.43	-0.07	22.66	100.02	91.25
7	22.37	0.23	22.60	100.02	91.28
8	22.81	-1.35	23.06	100.02	91.02
9	22.05	-0.81	22.27	100.02	91.15
10	22.29	0.17	22.52	100.02	91.35
11	22.32	0.10	22.55	100.02	91.15
12	22.27	0.34	22.50	100.03	91.98
13	21.97	0.34	22.19	100.02	91.17
14	22.17	0.03	22.39	100.01	91.48

Table A.1: Characterization of the BS secondary blade springs. See figure A.2 for the parameter description. The blade springs 4, 10, 11 and 14 were chosen for the second vertical isolation stage of the BS suspension.

# APPENDIX A. SUSPENSION BLADE SPRINGS

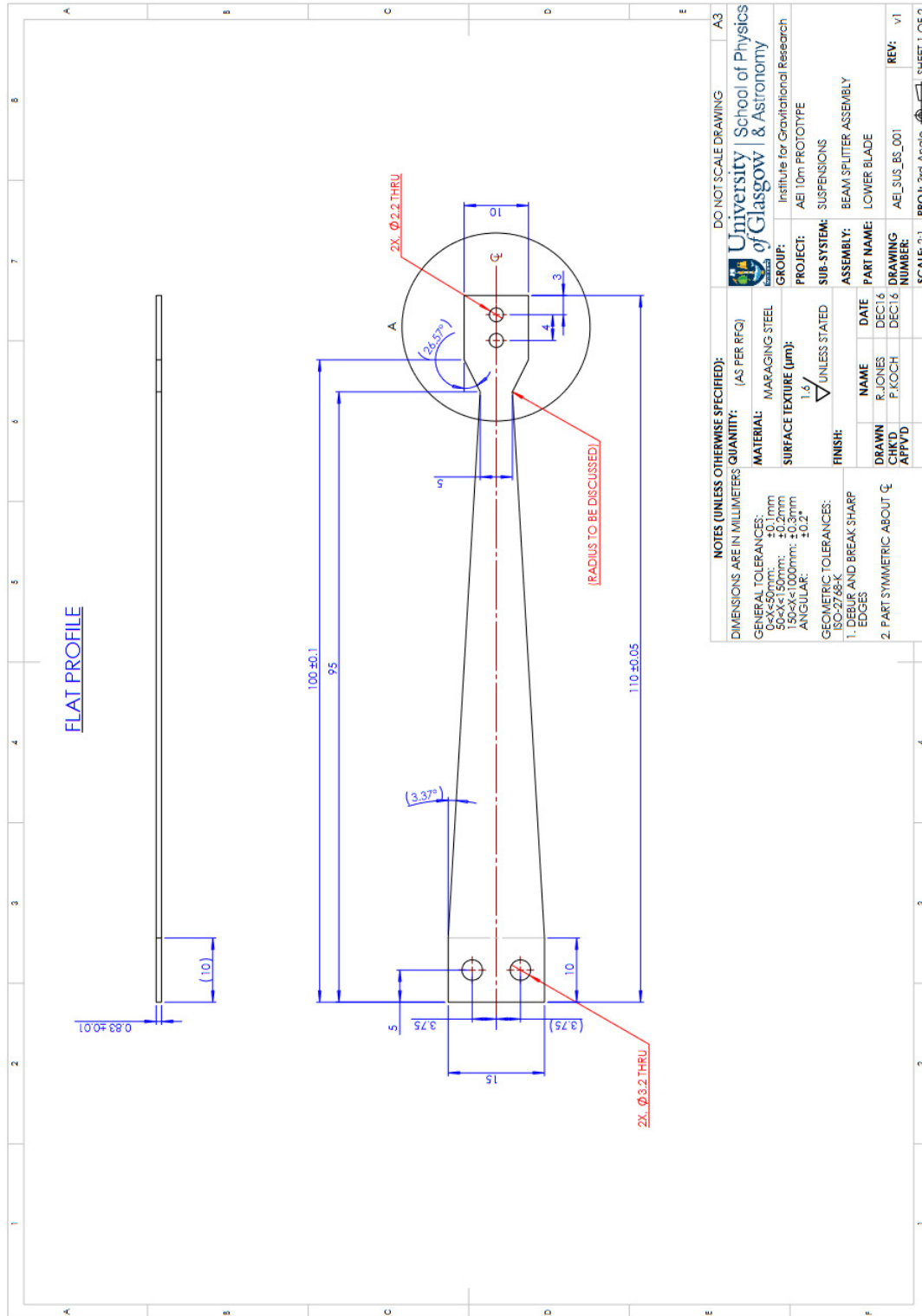


Figure A.3: Drawing for the BS suspension's secondary blade spring page 1.

# APPENDIX A. SUSPENSION BLADE SPRINGS

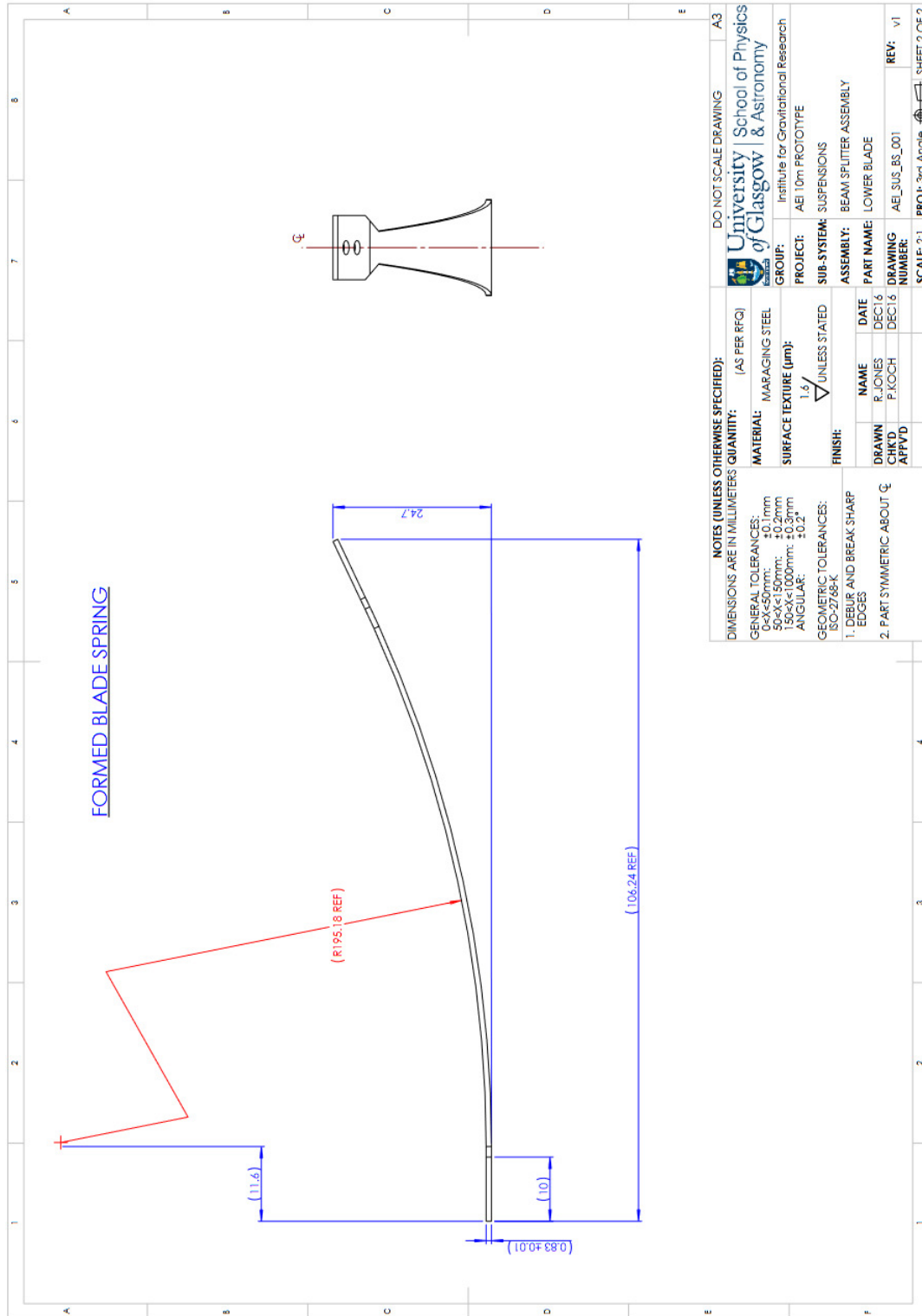


Figure A.4: Drawing for the BS suspension's secondary blade spring page 2.

## A.4 OMC suspension blade springs

The OMC blade springs were designed during the final period of my PhD thesis, and flat 420 stainless spring steel blades were already tested for some of the future aLIGO suspensions. Especially convinced by the low costs and lead times, we decided to choose the flat 420 stainless spring steel design approach for both the upper and lower blade springs of the OMC suspension.

As described above, 420 stainless spring steel is used as shimming material and is available in several standardized thicknesses. For the upper blades, a thickness of 2 mm, and for the lower blades, a thickness of 1 mm was chosen. Adjusting the width of the blade and its length allowed to tune the tip's deflection under load for the comparably heavy suspension. The stress under load and the blade's deflection was simulated with a finite element analysis in Autodesk Inventor (see figure A.5 and figure A.6 for the upper blades and figure A.7 and figure A.8 for the lower blades). The blades were characterized via camera pictures with the pixels calibrated to the blade spring's length. An exemplary picture can be seen in figure A.9 and the measured parameters are displayed in table A.2. The final drawings can be seen in figure A.10 for the upper blades and in figure A.11 for the lower blades.

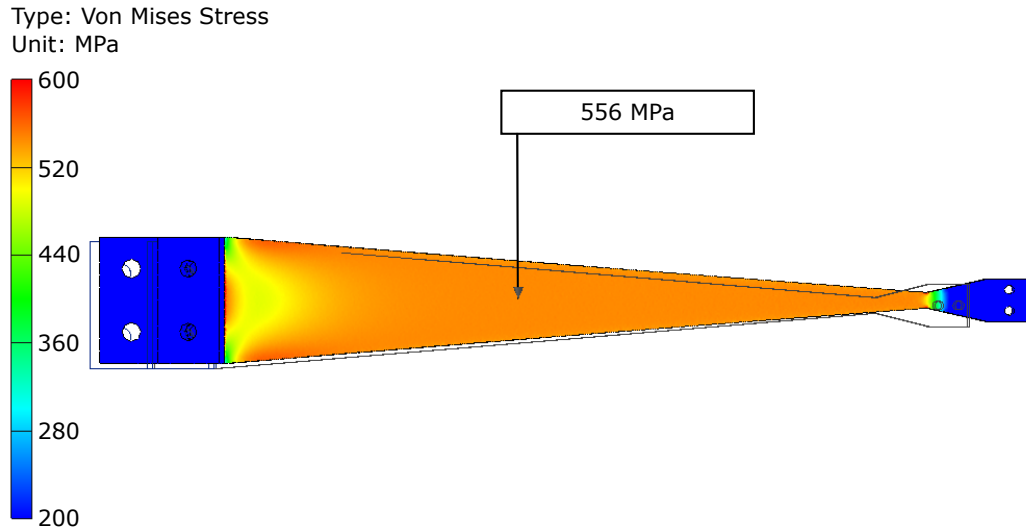


Figure A.5: Here, the stress on the upper OMC blade spring under load can be seen.

## APPENDIX A. SUSPENSION BLADE SPRINGS

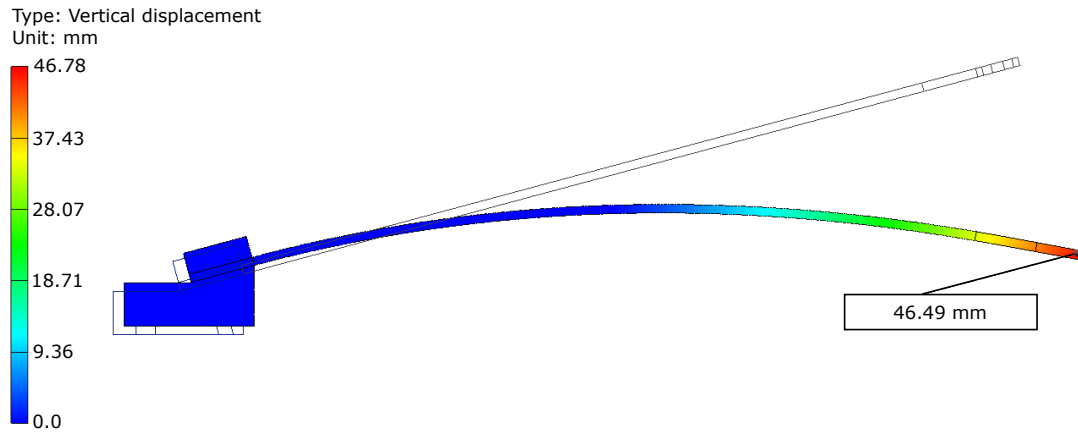


Figure A.6: Here, the vertical deflection of the upper OMC blade spring under load can be seen.

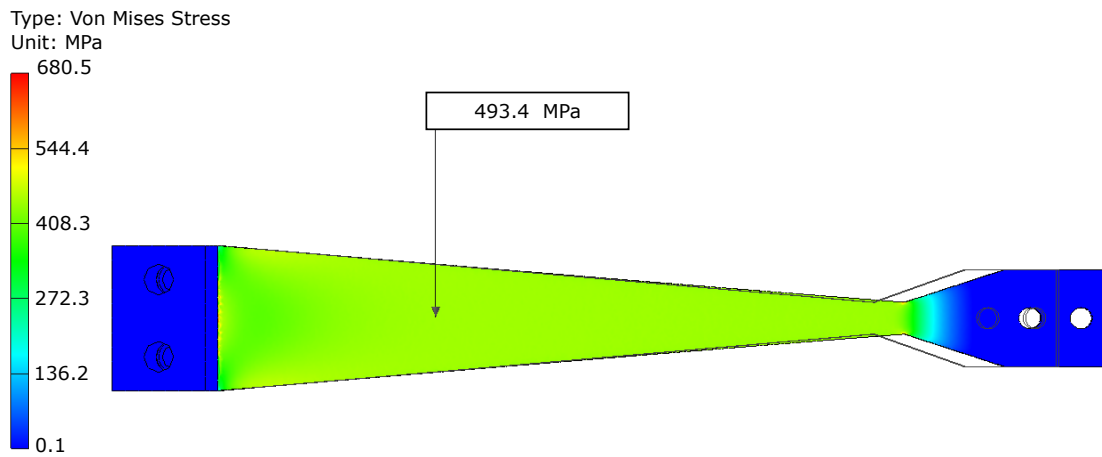


Figure A.7: Here, the stress on the lower OMC blade spring under load can be seen.

## APPENDIX A. SUSPENSION BLADE SPRINGS

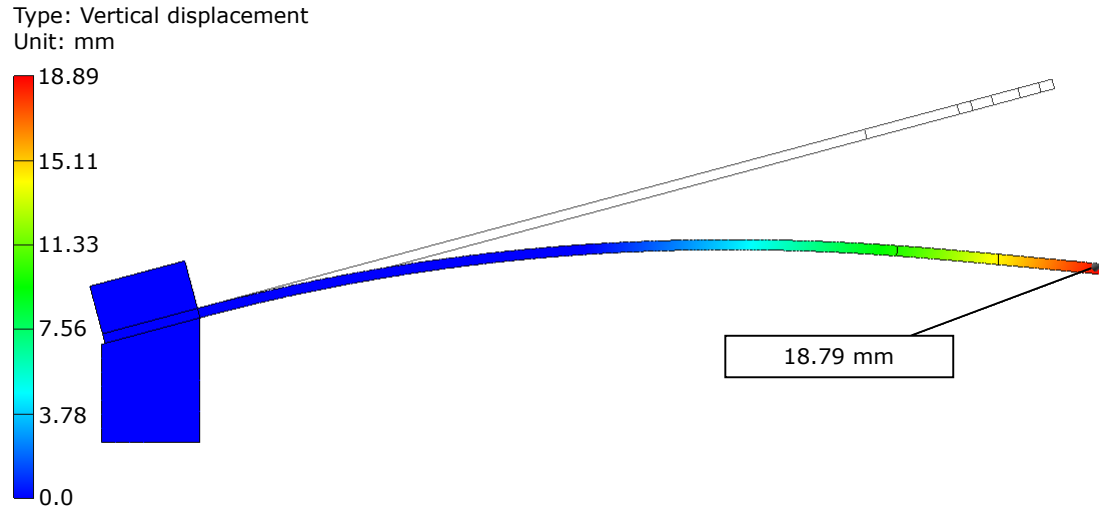


Figure A.8: Here, the vertical deflection of the lower OMC blade spring under load can be seen.

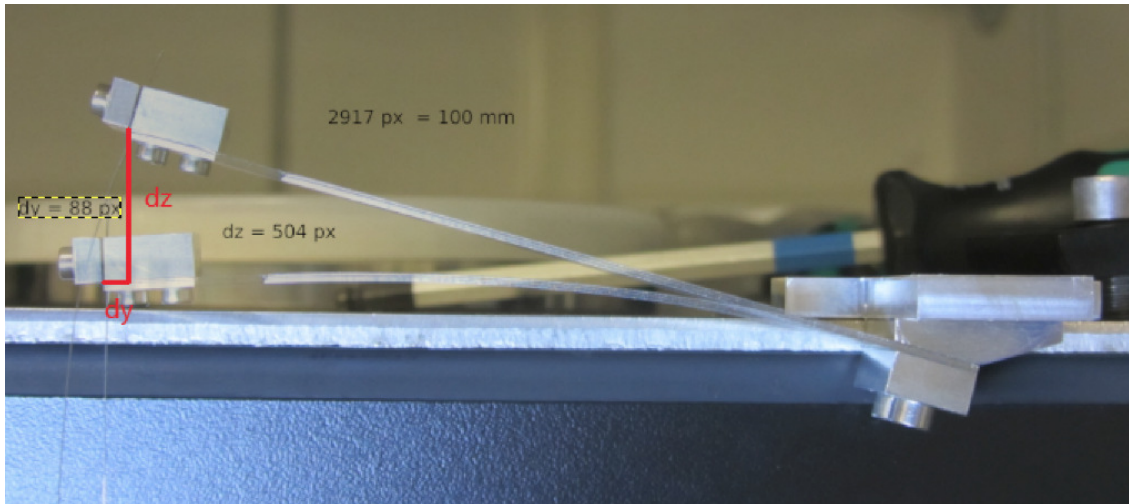


Figure A.9: Here, the OMC suspension's lower blade spring characterization using a camera picture can be seen. Parameter values for the different blade springs are shown in table A.2

## APPENDIX A. SUSPENSION BLADE SPRINGS

Blade	dy in mm	dz in mm
1	2.9	16.9
2	2.9	17.1
3	3.0	17.3
4	2.9	17.1
5	3.0	17.6
6	3.0	17.3
7	3.1	17.2
8	3.1	18.0
9	3.0	17.7
10	3.1	17.3
11	2.9	17.4
12	2.6	18.0
13	2.9	17.0
14	3.1	16.8
15	2.9	16.7
16	3.0	16.9
17	2.9	17.2
18	2.9	16.7
19	3.0	16.9
20	2.9	16.7
21	3.0	17.1
22	2.9	16.7
23	-	-
24	-	-
25	3.0	17.3

Table A.2: Characterization of the OMC's lower blade springs. See figure A.9 for the parameter description. Measured data for blade 23 and 24 went missing. The blade spring sets 3, 6, 10 and 25, and 15, 18, 20 and 22 were chosen for the second vertical isolation stages of the two future OMC suspension.

APPENDIX A. SUSPENSION BLADE SPRINGS

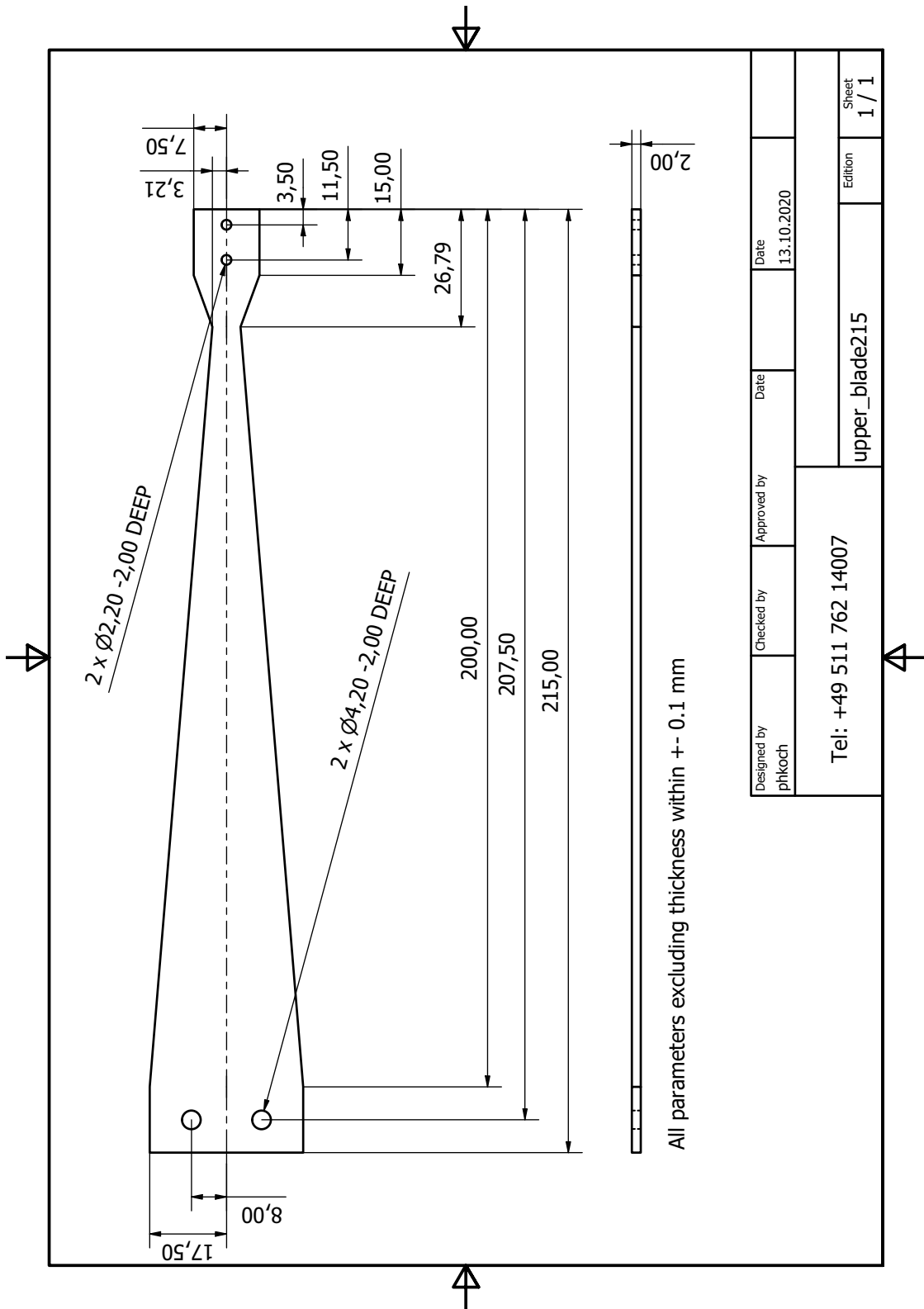


Figure A.10: Drawing for the OMC suspension's upper blade spring

APPENDIX A. SUSPENSION BLADE SPRINGS

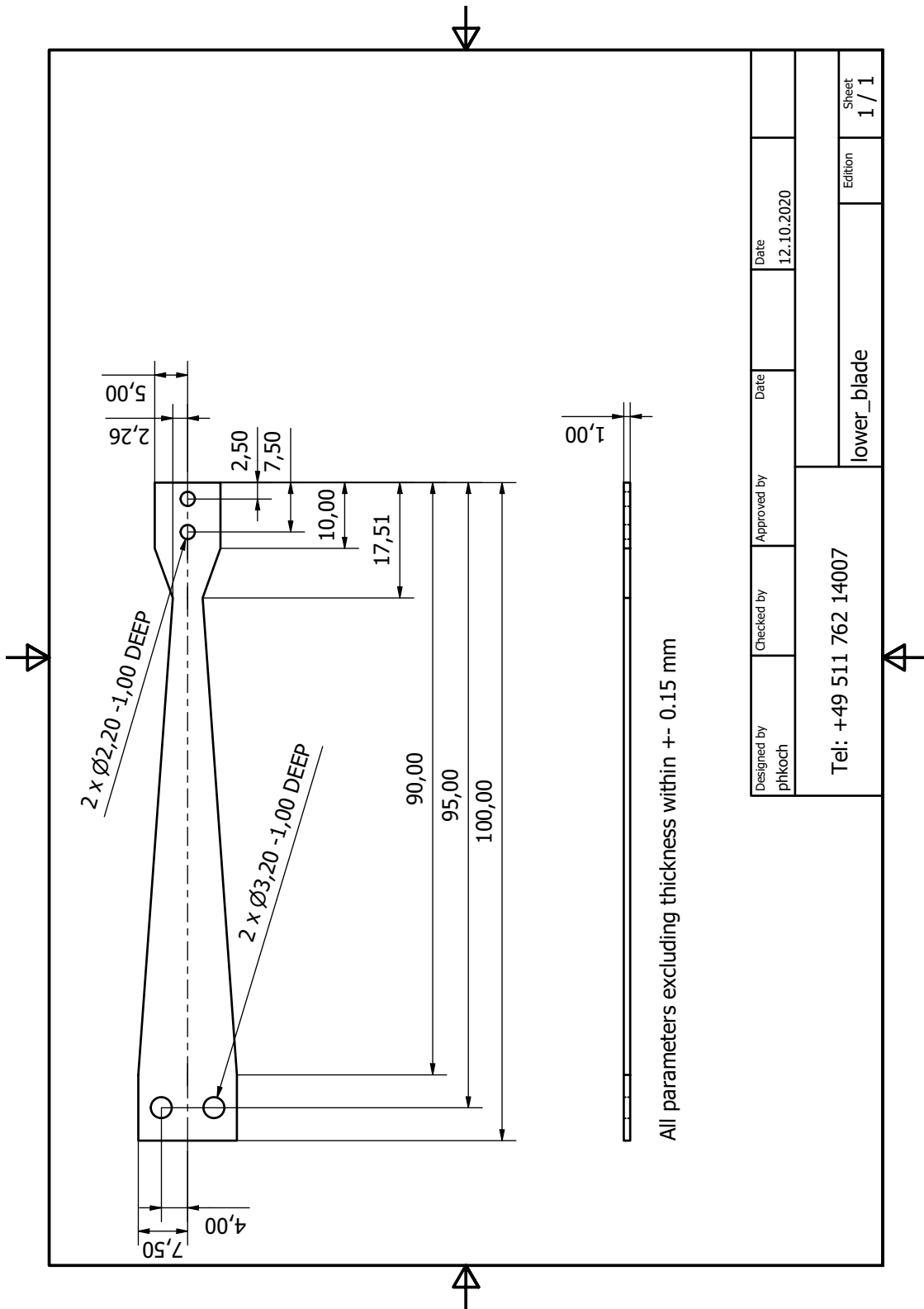


Figure A.11: Drawing for the OMC suspension's lower blade spring.

# Appendix B

## Low-loss OMC step-by-step

In chapter 5 I describe the designing and building procedure of the OMC for the sub-SQL interferometer. Its requirements are similar to the OMCs used in large-scale detectors. However, it is important to note that the OMC described in this thesis is designed for a single pair of phase modulation sidebands at a frequency of 21.34 Hz. The large scale detectors often use more than one pair of phase modulation sidebands, and if this OMC design is adapted, it needs to be ensured that none of them and none of their lower HOMs are resonant inside the OMC.

In this appendix, I like to provide a step-by-step guide to building a low loss OMC, reaching cavity losses of well below 1 %. A lot of information on the calculation and trade-offs during the design phase are explained in the corresponding thesis chapter (see 5). Here though, I like to focus on the experiences gained during and after setting up the OMC. I will link the thesis sections for more explanations and clarity within the guideline. A list of the drawings for the optical components and their requirements can be found in section B.2.

Many of the procedures used in this guideline are similar to the aLIGO OMC assembly procedure, which I learned from Koji Arai during my visit to Caltech. There we built a replacement for one of the aLIGO OMCs.

### B.1 Designing the OMC

Whether an existing design is adapted or a completely new design is implemented, the seemingly most important question is: "What are the requirements for the OMC?". Simply said, it needs to provide the right amount of filter performance for the experiment it is designed for. Once this question can be quantified, many other design aspects can be adapted.

### B.1.1 Cavity shape

The first design choice which should be made is the shape of the OMC cavity. Most of the pre-mode cleaners used at my institute are triangular cavities, while some are simple two-mirror Fabry-Perot cavities. The OMC designs used at aLIGO and GEO600 are four mirror cavities or, more accurately, bow-tie cavities.

The benefit of a low number of mirrors is the reduced loss by fewer optical surfaces which transmit or scatter a part of the incident laser beam. Nonetheless, a two-mirror cavity should be avoided, as the reflected beam is modulated with the motion of the OMC and steered back into the experiment. There it interferes with the light field of the detector and imprints noise onto the output beam. This effect might be reduced by the installation of one or more Faraday isolators, which would cause more losses than the loss reduction by the smaller number of mirrors. Now a decision between three and four mirrors needs to be made. The benefit of four mirrors is the ability to fold the cavity, increasing the round-trip length at a similar footprint. This needs to be weighed against the additional losses of the extra component. Further, an equal number of mirrors results in a degenerate cavity and thus a simpler mode distribution.

In my opinion, the increased length of a cavity at a defined footprint out-weights the smaller losses. It helps to separate the HOMs, making the cavity design less prone to errors.

### B.1.2 Quantifying the mode filter requirements

The output mode cleaner needs to reduce the HOM content in the detector's output beam to a hundredth of the desired mode (in most cases and in further explanations, the  $\text{TEM}_{00}$  mode) which is further explained in 5.2.1. Optimally we have access to the output beam profile of the experiment, including the power distribution of the  $\text{TEM}_{00}$  mode and phase modulation sidebands as well as their HOMs. If not, an output mode profile might be assumed when compared to a similar experiment.

Now that we have the output mode profile, we can proceed by calculating the FSR and TMS depending on the cavity round-trip length and radius of curvature of our cavity shape. This can be done, e.g., via the ABCD matrices as explained in the

sections 5.1.1 and 5.1.2. Combined with the cavity transfer function calculated for an arbitrary finesse (I used a finesse of 200), the transmission of all HOMs, sidebands, and HOMs of sidebands can be calculated and normalized to the transmitted power of the TEM<sub>00</sub> mode. The resulting plot shows the mode filter performance and can be displayed against the cavity's round-trip length and the mirror curvatures. Such a plot can be seen in figure 5.3.

Using the mode filter performance plot, a desired local minimum can be found, which provides some space for errors. It defines the round-trip length and curvature of the mirrors.

### B.1.3 Defining the finesse

The next step is to choose finesse. The finesse will directly change the mode filter performance, which can be plotted for the chosen round-trip length and mirror curvature. A low finesse results in lower optical cavity losses. For our OMC, I decided to implement a safety margin of factor 10. Thus, I chose a finesse that corresponds to a mode filter performance of one-thousandth instead of one-hundredth of the TEM<sub>00</sub> power in the detector output. In the end, about a factor of 1.5 was used up for a lower reflectivity of the in and output mirrors. A factor of six remains for eventual discrepancies between the assumed and real output mode profile of our interferometer.

### B.1.4 Defining an angle of incidence

As a next step, the angle of incidence needs to be defined. More information on the trade-off between astigmatism and back-scattering can be found in section 5.2.4. Similar to the finesse, the mode filter performance for a fixed round-trip length and mirror curvature can be calculated in dependence on the angle of incidence. Note that astigmatism leads to additional losses, which should be evaluated as well (e.g., with the finesse 2 software). For our OMC, these losses were around 0.01 % at an angle of incidence of 12.5 deg.

With the angle of incidence, all design parameters are defined, allowing to progress with the optical components and their requirements.

## B.2 Requirements for optical components

The major components are the four cavity mirrors, as these define the cavity performance and are expected to dominate the optical losses of the OMC assembly. The reflectivity can be easily determined. The in and output mirror's reflectivities are defined by the finesse. They should be coated in the same coating run to ensure close to identical coating parameters. The HR mirrors' reflectivities should be chosen around some single-digit ppm (we went with 5 ppm). Going beyond the 1 ppm mark seems unnecessary, as the absorption losses of the coatings are usually around 1 to 3 ppm. Further, it is said that thicker coating stacks can apply additional stress to the curved mirrors, changing their curvature. For our coatings, though, I haven't noticed any curvature change.

Another important property of the optics is the micro-roughness (see chapter 3.1.3). It contributes to the TIS of the optic and thus to the optical losses of the cavity. In the absence of point scatterers, the micro-roughness might even fully define the TIS. We chose a micro-roughness of below 1 Å for the central region of the optic with a diameter of 10 mm. Unfortunately, our cavity mirrors got mixed up during the coating run, and some mirrors with a micro-roughness of below 5 Å were coated as in and output mirrors. Later, scatter measurements showed no significant difference between the two kinds of optics which were polished at two different companies.

In our case, we chose a quasi-monolithic cavity design, i.e., gluing fused silica components to a fused silica breadboard. Here, we adapted the aLIGO approach, promising lower thermal noise compared to, e.g., an aluminum breadboard. The latter, though, promises a lower price tag and eventually more shape and alignment options. For the quasi-monolithic approach, the pitch angle of the mirrors is defined by the perpendicularity of the reflective surface to the gluing surface. It was defined to  $\pm 100 \mu\text{rad}$  to keep the laser spot within 1 mm of the optic's center position. Further, we chose a wedge angle of 0.5 deg and an AR coating to avoid any interferences with light reflected from the optics' rear surfaces.

We defined the surface figure to  $\lambda/10$  at 632 nm compared to  $\lambda/5$  for the aLIGO OMC optics. Later we noticed that, e.g., imprinting a specific HOM, matching the beam diameter with a PV value of 30 nm to the optic's surface can cause losses of

## APPENDIX B. LOW-LOSS OMC STEP-BY-STEP

above 1 %. This scenario seems unlikely but possible.

Reflectivity values for the individual optics can be found in chapter 5.3 and 5.6.

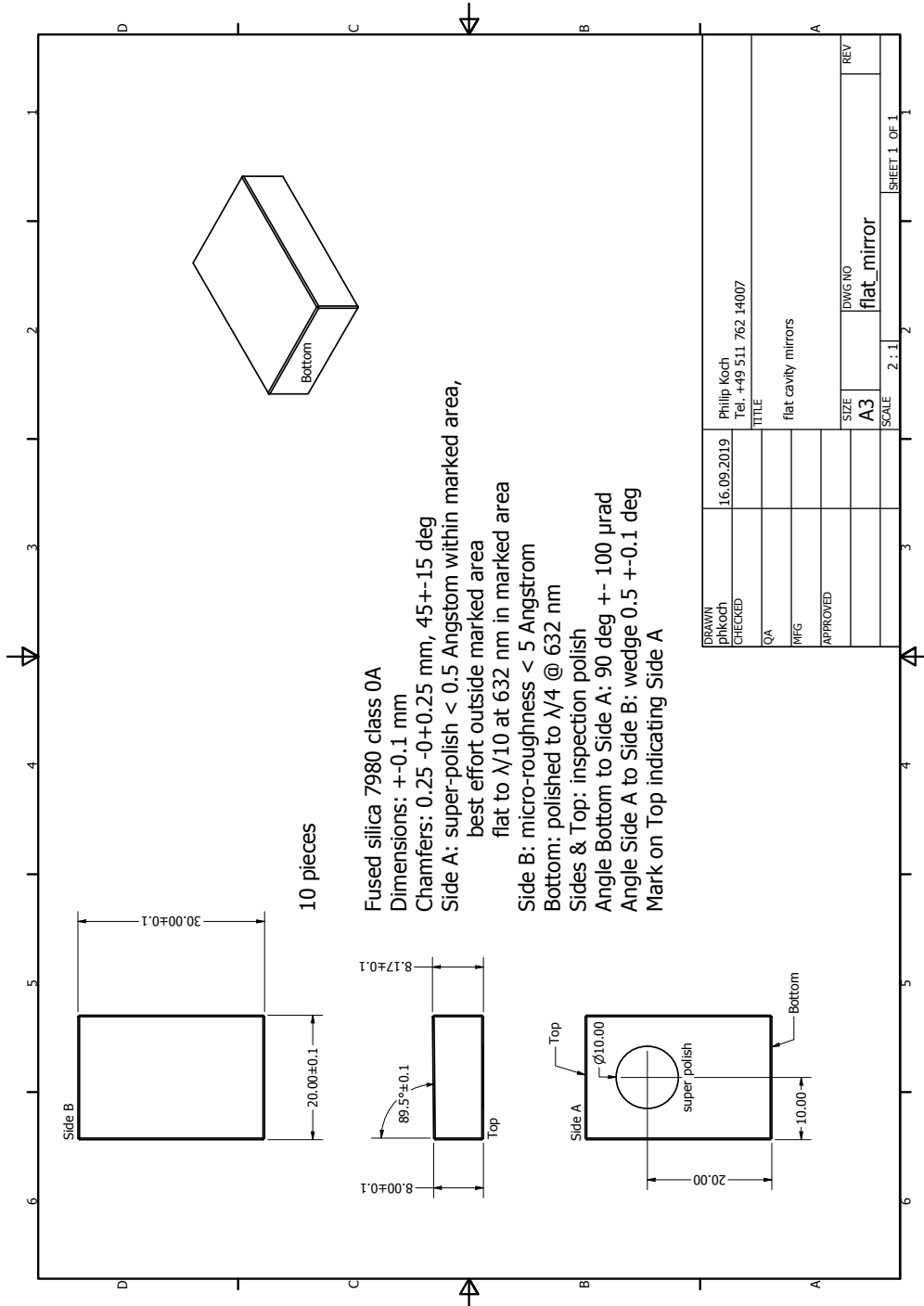


Figure B.1: Drawing for the OMC's in and output mirrors

APPENDIX B. LOW-LOSS OMC STEP-BY-STEP

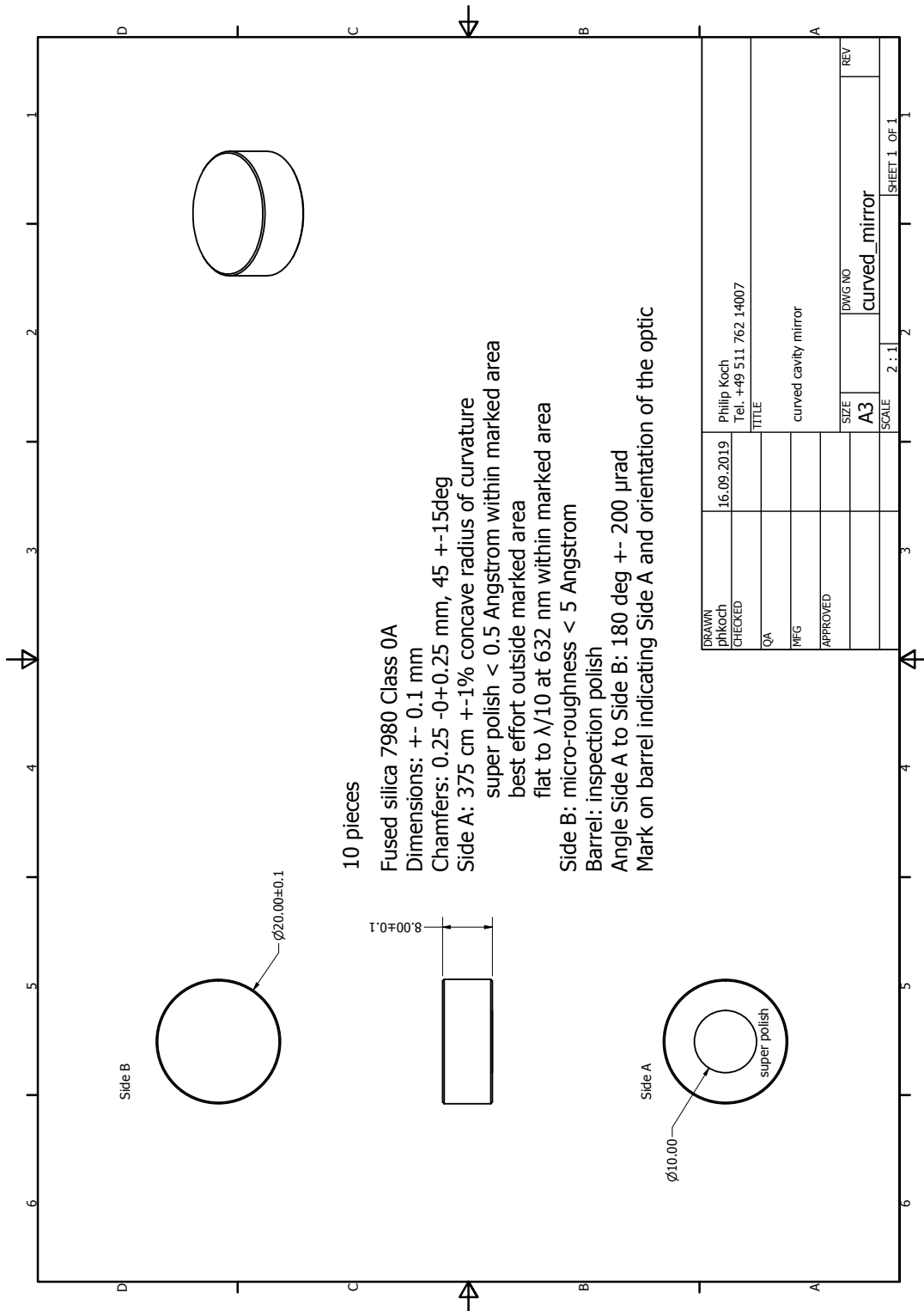


Figure B.2: Drawing for the OMC's curved mirrors

APPENDIX B. LOW-LOSS OMC STEP-BY-STEP

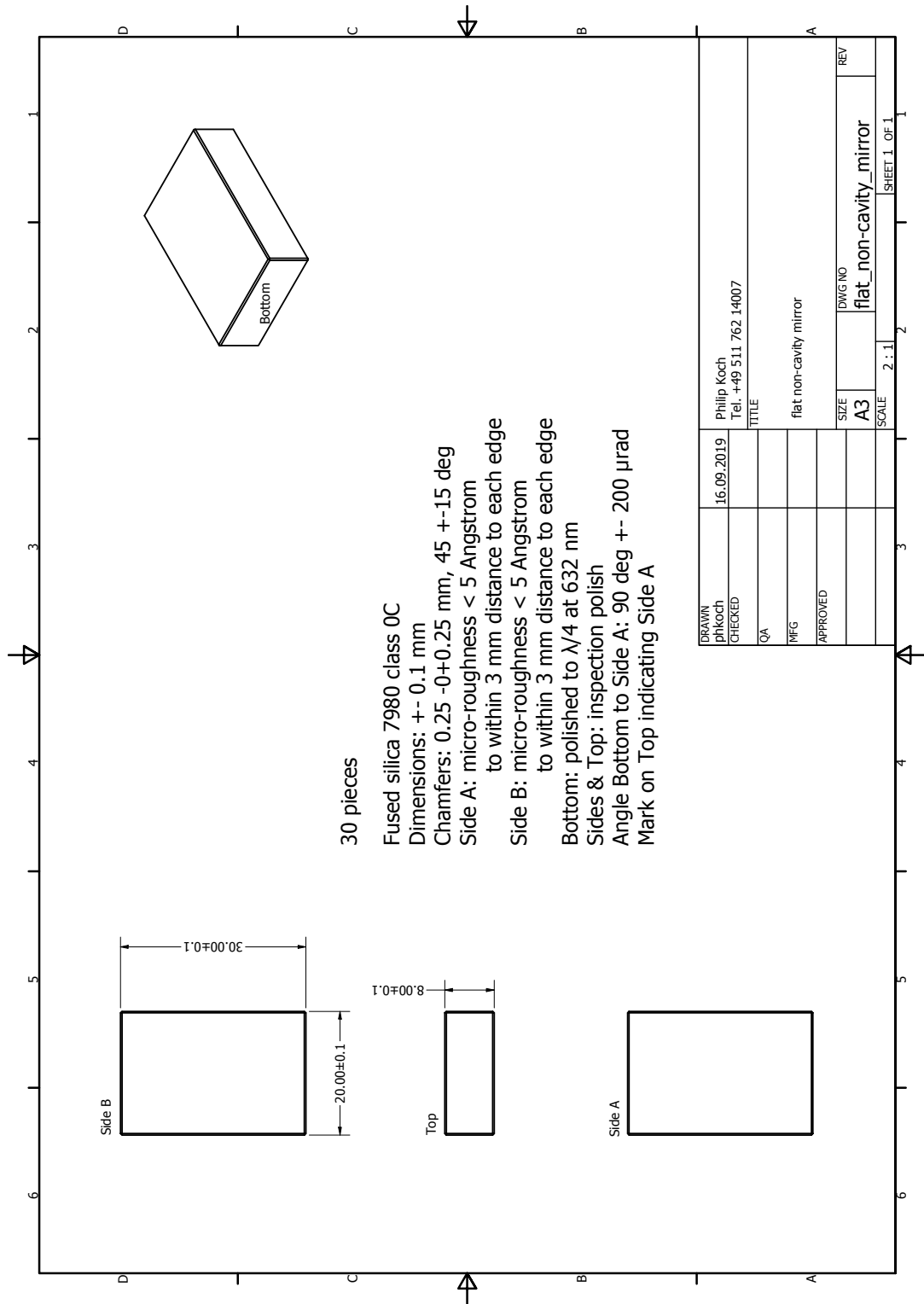


Figure B.3: Drawing for the OMC's non-cavity mirrors



APPENDIX B. LOW-LOSS OMC STEP-BY-STEP

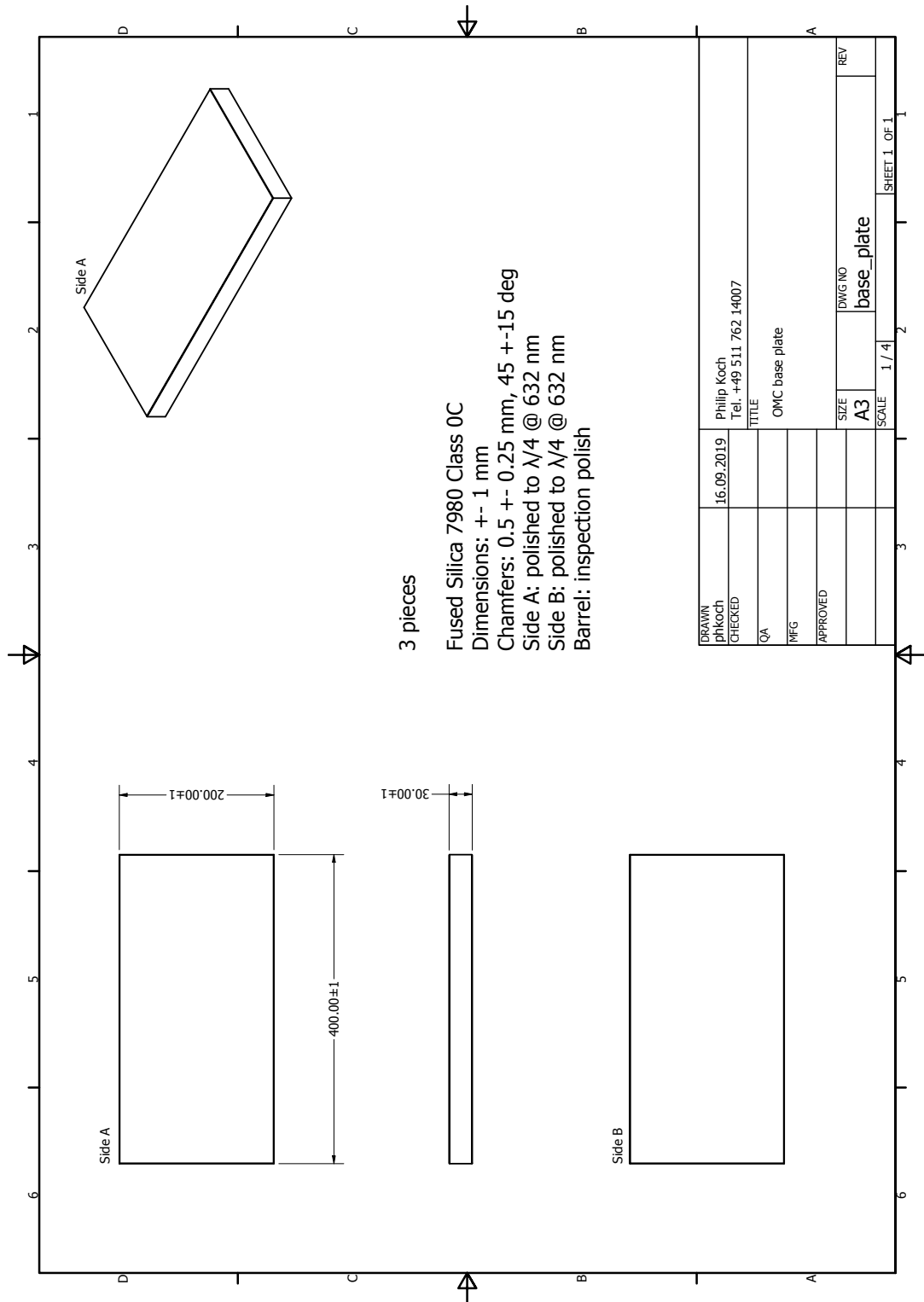


Figure B.5: Drawing for the OMC's bread board

### B.3 Optic characterization and preparation

Once delivered, it is important to characterize the components, finding the most promising components in terms of matching reflectivities and transmission and scatter losses. For this purpose, a set-up to measure the transmission of the mirrors as well as a device to measure scattering is essential. While measuring the transmission is comparably easy, not everyone might have access to scatter measurements. Chapter 3 describes a possible way to measure scattering. Alternatively, a decent camera could be placed at one scattering angle (probably around 15 deg) to image the scattering of an incident laser beam (10 mW should be fine). The resulting picture can be calibrated as described in chapter 3.2.3 and used to identify point scatterers and find the best performing mirrors.

Scattering images of high-quality optics (low micro-roughness) are often dominated by point scatterers. When our optics arrived, their scatter performance varied by several orders of magnitude (see figure 5.9). At a closer inspection, the number and amplitude of point scatterers varied, leading to different results. Once measured, I started to clean the optics with first contact and *drop and drag*. This significantly improved some of the optics' scattering by removing some of the point scatters. Additional cleaning seemed to change the number of point scatterers, sometimes improving, sometimes worsening the scattering. After a different number of cleaning processes, several optics seem to converge towards a similar BRDF. These seemed to have no or at least very weak point scatterers, thus being dominated by a well-distributed background scattering, most likely caused by the micro-roughness. Further, the BRDF of these optics seemed to be very flat (mirrors 1, 2, 7, 9 and 10 in figure 5.9). All of them showed a TIS of below 0.1 ppm (see table 5.2). Figures B.6 and B.7 show two in and output mirrors for the OMC cavity. The first showed a TIS of below 0.05 ppm and the second a TIS of 1.1 ppm.

It seemed crucial to ensure a low amount of point scatterers and recheck the scattering after each cleaning process. Thus, having some scatter measurement device at my disposal was essential for the preparation phase.

## APPENDIX B. LOW-LOSS OMC STEP-BY-STEP

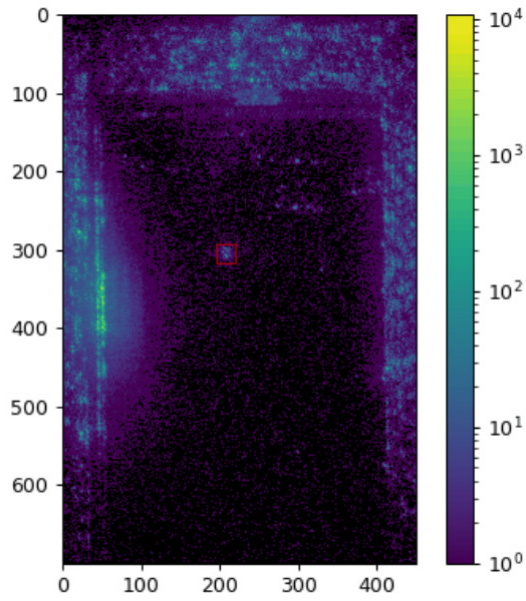


Figure B.6: Scatter image of an OMC's in and output mirror during BDRF measurement. It is dominated by background scattering with a TIS of 0.05 ppm.

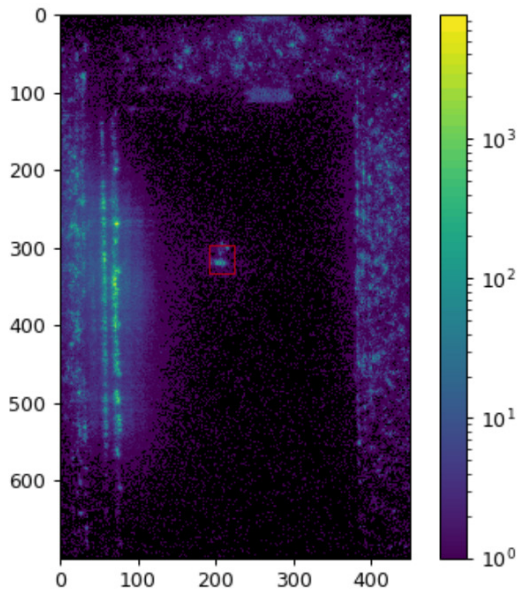


Figure B.7: Scatter image of an OMC's in and output mirror during BDRF measurement. It is dominated by point scatterers with a TIS of 1.1 ppm.

## B.4 Assembly

First, the sub-assembly of the curved mirrors, the PZTs, and the mirror mounts need to be prepared (see chapter 5.4.1). Next, a template should be used to accurately place the components (see chapter 5.4). The most crucial part here is to work with a set-up to measure the cavity parameters while placing the components (see figure 5.13). The UV-curing epoxy helps, as it stays liquid until a UV light source is used. Nonetheless, it should be applied to one mirror after another while cross-checking the cavity's alignment. For me, the curing process did not have any influence on the mirror position. I used a glue layer thickness of 2-3  $\mu\text{m}$ , controlled via the applied glue volume.

I recommend assembling the cavity in the cleanest possible environment, as dust flakes might gather under the template. Removing these can turn out to be complicated. If the losses turn out to be higher than expected, a CCD camera can be used to view the scattering of the individual mirrors and check for contaminations.

## B.5 OMC suspension

The design of the OMC suspension and its requirements is shown in chapter 5.5. Further information about designing a suspension can be found in chapter 4.2. The following table B.1 shows the suspension parameters for the OMC suspension. The longitudinal DOF is defined along the shorter and the side DOF along the longer side of the breadboard. For more information on DOFs, check figure 4.9.

Parameter	Value	Unit
Suspension top		
UW y-separation	140	mm
UW length	200	mm
1 <sup>st</sup> Stage		
Mass	5.7	kg
x-dimension	200	mm
y-dimension	400	mm

APPENDIX B. LOW-LOSS OMC STEP-BY-STEP

z-dimension	70	mm
I <sub>x</sub>	0.0735	kg m <sup>2</sup>
I <sub>y</sub>	0.0079	kg m <sup>2</sup>
I <sub>z</sub>	0.0771	kg m <sup>2</sup>
UW y-separation	140	mm
UW to CM z-separation	1	mm
LW x-separation	100	mm
LW y-separation	240	mm
LW to CM z-separation	2	mm
<i>2<sup>nd</sup> Stage</i>		
Mass	5.7	kg
x-dimension	200	mm
y-dimension	400	mm
z-dimension	60	mm
I <sub>x</sub>	0.0753	kg m <sup>2</sup>
I <sub>y</sub>	0.0186	kg m <sup>2</sup>
I <sub>z</sub>	0.0928	kg m <sup>2</sup>
LW x-separation	100	mm
LW y-separation	240	mm
LW to CM z-separation	26	mm

Table B.1: Overview of the OMC double-suspension parameters. I<sub>x</sub>, I<sub>y</sub> and I<sub>z</sub> describe the moment of inertia around the corresponding axis. The upper wire (UW) has a thickness of 400  $\mu\text{m}$ , and the lower wire (LW) has a thickness of 300  $\mu\text{m}$ . Both wires are attached to blade springs.

# Bibliography

- [Abb+16a] B. Abbott et al. “GW150914: The Advanced LIGO Detectors in the Era of First Discoveries”. In: *Physical Review Letters* 116.13 (Mar. 2016), p. 131103.
- [Abb+16b] B. Abbott et al. “Observation of Gravitational Waves from a Binary Black Hole Merger”. In: *Physical Review Letters* 116.6 (Feb. 2016), p. 061102.
- [Abb+02] R. Abbott et al. “Seismic isolation for Advanced LIGO”. In: *Classical and Quantum Gravity* 19.7 (Mar. 2002), pp. 1591–1597.
- [Ace+14] F. Acernese et al. “Advanced Virgo: a second-generation interferometric gravitational wave detector”. In: *Classical and Quantum Gravity* 32.2 (Dec. 2014), p. 024001.
- [Ace+20] F. Acernese et al. “Quantum Backaction on Kg-Scale Mirrors: Observation of Radiation Pressure Noise in the Advanced Virgo Detector”. In: *Physical Review Letters* 125.13 (Sept. 2020), p. 131101.
- [Ado19] J. I. Adorno. “Investigations of scattered light for beam dump design studies at the AEI 10m Prototype”. In: (2019).
- [Aku+20] T. Akutsu et al. “Overview of KAGRA: KAGRA science”. In: *Progress of Theoretical and Experimental Physics* 2021.5 (Aug. 2020).
- [Aku+21] T. Akutsu et al. “Vibration isolation systems for the beam splitter and signal recycling mirrors of the KAGRA gravitational wave detector”. In: *Classical and Quantum Gravity* 38.6 (Mar. 2021), p. 065011.
- [Ald03] J. Alda. “Laser and Gaussian beam propagation and transformation”. In: *Encyclopedia of optical engineering* 999 (2003).
- [Ara13] K. Arai. “On the accumulated round-trip Gouy phase shift for a general optical cavity”. In: *LIGO Technical Note* 1300189 (2013), pp. 1–11.

## BIBLIOGRAPHY

- [Ara22] K. Arai. “aLIGO OMC: Design, Fabrication, and Installation”. Apr. 2022. URL: <https://dcc.ligo.org/LIGO-G1301001>.
- [Ara+13] K. Arai et al. “Output mode cleaner design”. In: *LIGO working note, LIGO-T1000276-v5* (2013).
- [Arm22a] H. Armandula. “SPECIFICATION - Adv. LIGO - OMC - Curved Substrate Specifications”. Apr. 2022. URL: <https://dcc.ligo.org/LIGO-E070012>.
- [Arm22b] H. Armandula. “SPECIFICATIONS - Adv. LIGO - OMC - Flat Mirror Specifications”. Apr. 2022. URL: <https://dcc.ligo.org/LIGO-E070011>.
- [Art02] J. R. Arthur. “Molecular beam epitaxy”. In: *Surface Science* 500.1-3 (Mar. 2002), pp. 189–217.
- [BR86] H. E. Bennett et al. “Effects Of Surface And Bulk Defects In Transmitting Materials On Optical Resolution And Scattered Light”. In: *SPIE Proceedings*. Ed. by R. W. Schwartz. SPIE, Dec. 1986.
- [Ber+06] A. Bertolini et al. “Mechanical design of a single-axis monolithic accelerometer for advanced seismic attenuation systems”. In: *Nuclear Instruments and Methods in Physics Research Section A: Accelerators, Spectrometers, Detectors and Associated Equipment* 556.2 (Jan. 2006), pp. 616–623.
- [BBM02] I. A. Bilenko et al. “Thermal and excess noise in suspension fibres”. In: *Classical and Quantum Gravity* 19.7 (Mar. 2002), pp. 2035–2038.
- [BYZ17] G. Billingsley et al. “Characterization of Advanced LIGO core optics”. In: *American Society for Precision Engineering (ASPE)* 66 (2017), pp. 78–83.
- [Bon+17] R. Bonnand et al. “Upper-limit on the Advanced Virgo output mode cleaner cavity length noise”. In: *Classical and Quantum Gravity* 34.17 (July 2017), p. 175002.
- [Bui+20] A. Buikema et al. “Sensitivity and performance of the Advanced LIGO detectors in the third observing run”. In: *Physical Review D* 102.6 (Sept. 2020), p. 062003.

## BIBLIOGRAPHY

- [Car+12] L. Carbone et al. “Sensors and actuators for the Advanced LIGO mirror suspensions”. In: *Classical and Quantum Gravity* 29.11 (May 2012), p. 115005.
- [Col+13] G. D. Cole et al. “Tenfold reduction of Brownian noise in high-reflectivity optical coatings”. In: *Nature Photonics* 7.8 (July 2013), pp. 644–650.
- [Col+16] G. D. Cole et al. “High-performance near- and mid-infrared crystalline coatings”. In: *Optica* 3.6 (June 2016), p. 647.
- [CM04] T. Corbitt et al. “Review: Quantum noise in gravitational-wave interferometers”. In: *Journal of Optics B: Quantum and Semiclassical Optics* 6.8 (July 2004), S675–S683.
- [Dah+10] K. Dahl et al. “Towards a Suspension Platform Interferometer for the AEI 10 m Prototype Interferometer”. In: *Journal of Physics: Conference Series* 228 (May 2010), p. 012027.
- [DK12] S. L. Danilishin et al. “Quantum Measurement Theory in Gravitational-Wave Detectors”. In: *Living Reviews in Relativity* 15.1 (Apr. 2012).
- [DKM19] S. L. Danilishin et al. “Advanced quantum techniques for future gravitational-wave detectors”. In: *Living Reviews in Relativity* 22.1 (Apr. 2019).
- [DG85] R. M. Drake et al. “Mie scattering”. In: *American Journal of Physics* 53.10 (Oct. 1985), pp. 955–962.
- [Dre+83] R. W. P. Drever et al. “Laser phase and frequency stabilization using an optical resonator”. In: *Applied Physics B Photophysics and Laser Chemistry* 31.2 (June 1983), pp. 97–105.
- [DMM22] S. E. Dwyer et al. “Squeezing in Gravitational Wave Detectors”. In: *Galaxies* 10.2 (Mar. 2022), p. 46.
- [Edm22] Edmund. “Understanding Optical Specifications”. Apr. 2022. URL: <https://www.edmundoptics.com/knowledge-center/application-notes/optics/understanding-optical-specifications/>.
- [Ein16] A. Einstein. “Die Grundlage der allgemeinen Relativitätstheorie”. In: *Annalen der Physik* 354.7 (1916), pp. 769–822.

## BIBLIOGRAPHY

- [EMI22] EMIUV. “Optocast”. Apr. 2022. URL: <https://emiuv.com/optocast-2/>.
- [Fre+07] M. Frede et al. “Fundamental mode, single-frequency laser amplifier for gravitational wave detectors”. In: *Optics Express* 15.2 (Jan. 2007), p. 459.
- [FS10] A. Freise et al. “Interferometer techniques for gravitational-wave detection”. In: *Living Reviews in Relativity* 13.1 (2010), pp. 1–81.
- [FEF14] P. Fritschel et al. “Balanced homodyne readout for quantum limited gravitational wave detectors”. In: *Optics Express* 22.4 (Feb. 2014), p. 4224.
- [Gre07] D. A. Gregory. “Mie scattering of growing molecular contaminants”. In: *Optical Engineering* 46.3 (Mar. 2007), p. 033602.
- [gwo22] gwoptics. “Finesse 2”. Apr. 2022. URL: <http://www.gwoptics.org/finesse/>.
- [Har12] J. E. Harvey. “Total integrated scatter from surfaces with arbitrary roughness, correlation widths, and incident angles”. In: *Optical Engineering* 51.1 (Feb. 2012), p. 013402.
- [Her22] Heraeus. “Suprasil properties”. Apr. 2022. URL: [https://www.heraeus.com/media/media/hca/doc\\_hca/products\\_and\\_solutions\\_8/optics/Data\\_and\\_Properties\\_Optics\\_fused\\_silica\\_EN.pdf](https://www.heraeus.com/media/media/hca/doc_hca/products_and_solutions_8/optics/Data_and_Properties_Optics_fused_silica_EN.pdf).
- [HS96] M. A. Herman et al. “Molecular Beam Epitaxy”. Springer Berlin Heidelberg, 1996.
- [Heu18] M. Heurs. “Gravitational wave detection using laser interferometry beyond the standard quantum limit”. In: *Philosophical Transactions of the Royal Society A: Mathematical, Physical and Engineering Sciences* 376.2120 (Apr. 2018), p. 20170289.
- [Heu+06] M. Heurs et al. “Intensity and frequency noise reduction of a Nd:YAG NPRO via pump light stabilisation”. In: *Applied Physics B* 85.1 (July 2006), pp. 79–84.

## BIBLIOGRAPHY

- [HT75] R. A. Hulse et al. “Discovery of a pulsar in a binary system”. In: *The Astrophysical Journal* 195 (Jan. 1975), p. L51.
- [J A+15] and J Aasi et al. “Advanced LIGO”. In: *Classical and Quantum Gravity* 32.7 (Mar. 2015), p. 074001.
- [JOW17] J. Junker et al. “Shot-noise-limited laser power stabilization for the AEI 10 m Prototype interferometer”. In: *Optics Letters* 42.4 (Feb. 2017), p. 755.
- [KFM63] M. Kerker et al. “Applicability of Rayleigh-Gans Scattering to Spherical Particles”. In: *Journal of the Optical Society of America* 53.6 (June 1963), p. 758.
- [Kir22] R. Kirchhoff. “Implementation of an active seismic isolation system for the AEI 10 m prototype”. en. 2022.
- [Kni+98] J. Knight et al. “Large mode area photonic crystal fibre”. In: *Electronics Letters* 34.13 (1998), pp. 1347–1348.
- [Koc+19] P. Koch et al. “Thickness uniformity measurements and damage threshold tests of large-area GaAs/AlGaAs crystalline coatings for precision interferometry”. In: *Optics Express* 27.25 (Dec. 2019), p. 36731.
- [KL66] H. Kogelnik et al. “Laser Beams and Resonators”. In: *Applied Optics* 5.10 (Oct. 1966), p. 1550.
- [Kop14] S. J. Koppal. “Lambertian Reflectance”. In: *Computer Vision*. Springer US, 2014, pp. 441–443.
- [LF11] V. Lakshminarayanan et al. “Zernike polynomials: a guide”. In: *Journal of Modern Optics* 58.7 (Apr. 2011), pp. 545–561.
- [Lou+21] J. Lough et al. “First Demonstration of 6 dB Quantum Noise Reduction in a Kilometer Scale Gravitational Wave Observatory”. In: *Physical Review Letters* 126.4 (Jan. 2021), p. 041102.
- [LCW09] X. Luo et al. “Power content M 2-values smaller than one”. In: *Applied Physics B* 98.1 (June 2009), pp. 181–185.

## BIBLIOGRAPHY

- [Mag+12] F. Magaña-Sandoval et al. “Large-angle scattered light measurements for quantum-noise filter cavity design studies”. In: *Journal of the Optical Society of America A* 29.8 (July 2012), p. 1722.
- [Mat22] MathWorks. “MathWorks Simulink”. Apr. 2022. URL: <https://de.mathworks.com/products/simulink.html>.
- [MLF01] R. B. Miles et al. “Laser Rayleigh scattering”. In: *Measurement Science and Technology* 12.5 (Apr. 2001), R33–R51.
- [Orf22] S. Orfani. “Electromagnetic Waves and Antennas”. Apr. 2022. URL: <http://eceweb1.rutgers.edu/~orfanidi/ewa/>.
- [OFW12] D. J. Ottaway et al. “Impact of upconverted scattered light on advanced interferometric gravitational wave detectors”. In: *Optics Express* 20.8 (Mar. 2012), p. 8329.
- [Pen57] R. B. Penndorf. “New Tables of Total Mie Scattering Coefficients for Spherical Particles of Real Refractive Indexes ( $1.33 \leq n \leq 1.50$ )”. In: *Journal of the Optical Society of America* 47.11 (Nov. 1957), p. 1010.
- [Pin+16] L. Pinard et al. “Mirrors used in the LIGO interferometers for first detection of gravitational waves”. In: *Applied Optics* 56.4 (Oct. 2016), p. C11.
- [Pra+18] K. Prasad et al. “Highly reflective coatings”. In: *Int J Appl Eng Res* 13.22 (2018), pp. 15773–15782.
- [RJS09] D. Ristau et al. “Laser damage thresholds of optical coatings”. In: *Thin Solid Films* 518.5 (Dec. 2009), pp. 1607–1613.
- [RC91] E. Robinson et al. “Sampling and the Nyquist frequency”. In: *The Leading Edge* 10.3 (Mar. 1991), pp. 51–53.
- [RF73] A. Rubinshtein et al. “Theory of avalanche ionization in transparent dielectrics under the action of a strong electromagnetic field”. In: *Sov. Phys.-Solid State* 15.3 (1973), pp. 332–336.
- [SSP01] S. Saghafi et al. “Characterising elegant and standard Hermite-Gaussian beam modes”. In: *Optics Communications* 191.3-6 (May 2001), pp. 173–179.

## BIBLIOGRAPHY

- [Sch+11] S. Schröder et al. “Modeling of light scattering in different regimes of surface roughness”. In: *Optics Express* 19.10 (May 2011), p. 9820.
- [Sel83] S. A. Self. “Focusing of spherical Gaussian beams”. In: *Applied Optics* 22.5 (Mar. 1983), p. 658.
- [Sho+88] D. Shoemaker et al. “Noise behavior of the Garching 30-meter prototype gravitational-wave detector”. In: *Physical Review D* 38.2 (July 1988), pp. 423–432.
- [Sie86] A. E. Siegman. “Lasers”. University science books, 1986.
- [SGR83] J. R. Sites et al. “Ion Beam Sputter Deposition Of Optical Coatings”. In: *Optical Engineering* 22.4 (Aug. 1983).
- [Som12] K. Somiya. “Detector configuration of KAGRA—the Japanese cryogenic gravitational-wave detector”. In: *Classical and Quantum Gravity* 29.12 (June 2012), p. 124007.
- [Ste18] J. Steinlechner. “Development of mirror coatings for gravitational-wave detectors”. In: *Philosophical Transactions of the Royal Society A: Mathematical, Physical and Engineering Sciences* 376.2120 (Apr. 2018), p. 20170282.
- [Sto90] J. C. Stover. “Scatter From Optical Components: An Overview”. In: *Scatter from Optical Components*. Ed. by J. C. Stover. SPIE, Jan. 1990.
- [Tec22] P. C. Technologies. “First-Contact”. Apr. 2022. URL: <https://www.photoniccleaning.com/>.
- [Tho22a] Thorlabs. “Linear power density calculations”. Apr. 2022. URL: [https://www.thorlabs.com/NewGroupPage9\\_PF.cfm?Guide=10&Category\\_ID=220&ObjectGroup\\_ID=3793](https://www.thorlabs.com/NewGroupPage9_PF.cfm?Guide=10&Category_ID=220&ObjectGroup_ID=3793).
- [Tho22b] Thorlabs. “Protected Gold mirrors”. Apr. 2022. URL: [https://www.thorlabs.com/newgrouppage9.cfm?objectgroup\\_id=744](https://www.thorlabs.com/newgrouppage9.cfm?objectgroup_id=744).
- [Wan+12] A. Wanner et al. “Seismic attenuation system for the AEI 10 meter Prototype”. In: *Classical and Quantum Gravity* 29.24 (Nov. 2012), p. 245007.

## BIBLIOGRAPHY

- [Wei02] A. Weinstein. “Advanced LIGO optical configuration and prototyping effort”. In: *Classical and Quantum Gravity* 19.7 (Mar. 2002), pp. 1575–1584.
- [Wes16] T. Westphal. “A coating thermal noise interferometer for the AEI 10 m prototype facility”. In: *Ph. D. Thesis* (2016).
- [Wil+02] B. Willke et al. “The GEO 600 gravitational wave detector”. In: *Classical and Quantum Gravity* 19.7 (Mar. 2002), pp. 1377–1387.
- [Wil+08] B. Willke et al. “Stabilized lasers for advanced gravitational wave detectors”. In: *Classical and Quantum Gravity* 25.11 (May 2008), p. 114040.
- [Wit09] H. Wittel. “Compensation of the thermal lens in the GEO600 beam splitter”. PhD thesis. Laser Interferometry & Gravitational Wave Astronomy, AEI-Hannover, MPI for . . . , 2009.

## Publication list

- [Koc+19] P. Koch et al. “Thickness uniformity measurements and damage threshold tests of large-area GaAs/AlGaAs crystalline coatings for precision interferometry”. In: *Optics Express* 27.25 (Dec. 2019), p. 36731.
- [Kir+17] R. Kirchhoff et al. “Huddle test measurement of a near Johnson noise limited geophone”. In: *Review of Scientific Instruments* 88.11 (Nov. 2017), p. 115008.
- [Kir+20] R. Kirchhoff et al. “Local active isolation of the AEI-SAS for the AEI 10 m prototype facility”. In: *Classical and Quantum Gravity* 37.11 (May 2020), p. 115004.

## Collaboration publications

- [LSC16a] LSC. “All-sky search for short gravitational-wave bursts in the first Advanced LIGO run”. In: *Phys. Rev. D* 95, 042003 (2017) (Nov. 2016). arXiv: 1611.02972 [gr-qc].
- [LSC16b] LSC. “Effects of waveform model systematics on the interpretation of GW150914”. In: *Class. Quantum Grav.* 34 (2017) 104002 (Nov. 2016). arXiv: 1611.07531 [gr-qc].
- [LSC16c] LSC. “Search for Gravitational Waves Associated with Gamma-Ray Bursts During the First Advanced LIGO Observing Run and Implications for the Origin of GRB 150906B”. In: (Nov. 2016). arXiv: 1611.07947 [astro-ph.HE].
- [LSC16d] LSC. “Directional limits on persistent gravitational waves from Advanced LIGO’s first observing run”. In: *Phys. Rev. Lett.* 118, 121102 (2017) (Dec. 2016). arXiv: 1612.02030 [gr-qc].
- [LSC16e] LSC. “Upper Limits on the Stochastic Gravitational-Wave Background from Advanced LIGO’s First Observing Run”. In: *Phys. Rev. Lett.* 118, 121101 (2017) (Dec. 2016). eprint: 1612.02029 (gr-qc).
- [LSC17a] LSC. “First search for gravitational waves from known pulsars with Advanced LIGO”. In: *Astrophys. J.* 839 12 (2017) 19 (Jan. 2017). arXiv: 1701.07709 [astro-ph.HE].
- [LSC17b] LSC. “Search for High-energy Neutrinos from Gravitational Wave Event GW151226 and Candidate LVT151012 with ANTARES and IceCube”. In: *Phys. Rev. D* 96, 022005 (2017) (Mar. 2017). arXiv: 1703.06298 [astro-ph.HE].

- [LSC17c] LSC. “Search for gravitational waves from Scorpius X-1 in the first Advanced LIGO observing run with a hidden Markov model”. In: *Phys. Rev. D* *95*, 122003 (2017) (Apr. 2017). arXiv: **1704.03719** [gr-qc].
- [LSC17d] LSC. “Search for intermediate mass black hole binaries in the first observing run of Advanced LIGO”. In: *Phys. Rev. D* *96*, 022001 (2017) (Apr. 2017). eprint: **1704.04628** (gr-qc).
- [LSC17e] LSC. “GW170104: Observation of a 50-Solar-Mass Binary Black Hole Coalescence at Redshift 0.2”. In: *Phys. Rev. Lett.*, *118*(22):221101, 2017 (June 2017). arXiv: **1706.01812** [gr-qc].
- [LSC17f] LSC. “Upper Limits on Gravitational Waves from Scorpius X-1 from a Model-Based Cross-Correlation Search in Advanced LIGO Data”. In: *The Astrophysical Journal*, *847*:47 (14pp), 2017 September 20 (June 2017). arXiv: **1706.03119** [astro-ph.HE].
- [LSC17g] LSC. “First low-frequency Einstein@Home all-sky search for continuous gravitational waves in Advanced LIGO data”. In: *Phys. Rev. D* *96*, 122004 (2017) (July 2017). arXiv: **1707.02669** [gr-qc].
- [LSC17h] LSC. “All-sky Search for Periodic Gravitational Waves in the O1 LIGO Data”. In: *Phys. Rev. D* *96*, 062002 (2017) (July 2017). arXiv: **1707.02667** [gr-qc].
- [LSC13] LSC. “Prospects for Observing and Localizing Gravitational-Wave Transients with Advanced LIGO, Advanced Virgo and KAGRA”. In: *Living Rev Relativ* *23*, 3 (2020) (Apr. 2013). arXiv: **1304.0670** [gr-qc].
- [LSC17i] LSC. “GW170814: A Three-Detector Observation of Gravitational Waves from a Binary Black Hole Coalescence”. In: *Phys. Rev. Lett.* *119*, 141101 (2017) (Sept. 2017). arXiv: **1709.09660** [gr-qc].
- [LSC17j] LSC. “First search for nontensorial gravitational waves from known pulsars”. In: *Phys. Rev. Lett.* *120*, 031104 (2018) (Sept. 2017). arXiv: **1709.09203** [gr-qc].

- [LSC17k] LSC. “Effects of Data Quality Vetoes on a Search for Compact Binary Coalescences in Advanced LIGO’s First Observing Run”. In: *Class. Quantum Grav.* 35 065010 (2018) (Oct. 2017). arXiv: 1710.02185 [gr-qc].
- [LSC17l] LSC. “First narrow-band search for continuous gravitational waves from known pulsars in advanced detector data”. In: *Phys. Rev. D* 96, 122006 (2017) (Oct. 2017). arXiv: 1710.02327 [gr-qc].
- [LSC17m] LSC. “Search for High-energy Neutrinos from Binary Neutron Star Merger GW170817 with ANTARES, IceCube, and the Pierre Auger Observatory”. In: (Oct. 2017). eprint: 1710.05839 (astro-ph.HE).
- [LSC17n] LSC. “On the Progenitor of Binary Neutron Star Merger GW170817”. In: *ApJL*, 850, L40, 2017 (Oct. 2017). arXiv: 1710.05838 [astro-ph.HE].
- [LSC17o] LSC. “GW170817: Implications for the Stochastic Gravitational-Wave Background from Compact Binary Coalescences”. In: *Phys. Rev. Lett.* 120, 091101 (2018) (Oct. 2017). arXiv: 1710.05837 [gr-qc].
- [LSC17p] LSC. “Estimating the Contribution of Dynamical Ejecta in the Kilonova Associated with GW170817”. In: (Oct. 2017). arXiv: 1710.05836 [astro-ph.HE].
- [LSC17q] LSC. “A gravitational-wave standard siren measurement of the Hubble constant”. In: (Oct. 2017). arXiv: 1710.05835 [astro-ph.CO].
- [LSC17r] LSC. “Gravitational Waves and Gamma-rays from a Binary Neutron Star Merger: GW170817 and GRB 170817A”. In: *The Astrophysical Journal Letters*, 848:L13 (27pp), 2017 October 20 (Oct. 2017). arXiv: 1710.05834 [astro-ph.HE].
- [LSC17s] LSC. “Multi-messenger Observations of a Binary Neutron Star Merger”. In: *ApJL*, 848:L12, 2017 (Oct. 2017). arXiv: 1710.05833 [astro-ph.HE].
- [LSC17t] LSC. “GW170817: Observation of Gravitational Waves from a Binary Neutron Star Inspiral”. In: *Phys. Rev. Lett.* 119 161101 (2017) (Oct. 2017). arXiv: 1710.05832 [gr-qc].

- [LSC17u] LSC. “Search for post-merger gravitational waves from the remnant of the binary neutron star merger GW170817”. In: *ApJL*, 851:L16 (2017) (Oct. 2017). eprint: **1710.09320** (astro-ph.HE).
- [LSC17v] LSC. “GW170608: Observation of a 19-solar-mass Binary Black Hole Coalescence”. In: (Nov. 2017). arXiv: **1711.05578** [astro-ph.HE].
- [LSC17w] LSC. “All-sky search for long-duration gravitational wave transients in the first Advanced LIGO observing run”. In: (Nov. 2017). arXiv: **1711.06843** [gr-qc].
- [LSC17x] LSC. “Constraints on cosmic strings using data from the first Advanced LIGO observing run”. In: *Phys. Rev. D* 97, 102002 (2018) (Dec. 2017). arXiv: **1712.01168** [gr-qc].
- [LSC18a] LSC. “Full Band All-sky Search for Periodic Gravitational Waves in the O1 LIGO Data”. In: *Phys. Rev. D* 97, 102003 (2018) (Feb. 2018). arXiv: **1802.05241** [gr-qc].
- [LSC18b] LSC. “A Search for Tensor, Vector, and Scalar Polarizations in the Stochastic Gravitational-Wave Background”. In: *Phys. Rev. Lett.* 120, 201102 (2018) (Feb. 2018). arXiv: **1802.10194** [gr-qc].
- [LSC18c] LSC. “GW170817: Measurements of Neutron Star Radii and Equation of State”. In: *Phys. Rev. Lett.* 121, 161101 (2018) (May 2018). arXiv: **1805.11581** [gr-qc].
- [LSC18d] LSC. “Properties of the binary neutron star merger GW170817”. In: *Phys. Rev. X* 9, 011001 (2019) (May 2018). eprint: **1805.11579** (gr-qc).
- [LSC18e] LSC. “Search for sub-solar mass ultracompact binaries in Advanced LIGO’s first observing run”. In: *Phys. Rev. Lett.* 121, 231103 (2018) (Aug. 2018). arXiv: **1808.04771** [astro-ph.CO].
- [LSC18f] LSC. “Constraining the p-mode–g-mode tidal instability with GW170817”. In: *Phys. Rev. Lett.* 122, 061104 (2019) (Aug. 2018). arXiv: **1808.08676** [astro-ph.HE].

- [LSC18g] LSC. “A Fermi Gamma-ray Burst Monitor Search for Electromagnetic Signals Coincident with Gravitational-Wave Candidates in Advanced LIGO’s First Observing Run”. In: (Oct. 2018). arXiv: [1810.02764](#) [astro-ph.HE].
- [LSC18h] LSC. “Search for gravitational waves from a long-lived remnant of the binary neutron star merger GW170817”. In: *The Astrophysical Journal* *875:160 (2019)* (Oct. 2018). arXiv: [1810.02581](#) [gr-qc].
- [LSC18i] LSC. “Search for Multi-messenger Sources of Gravitational Waves and High-energy Neutrinos with Advanced LIGO during its first Observing Run, ANTARES and IceCube”. In: *Astrophys. J.* *870 (2019) 134* (Oct. 2018). arXiv: [1810.10693](#) [astro-ph.HE].
- [LSC18j] LSC. “Tests of General Relativity with GW170817”. In: *Phys. Rev. Lett.* *123, 011102 (2019)* (Nov. 2018). arXiv: [1811.00364](#) [gr-qc].
- [LSC18k] LSC. “Binary Black Hole Population Properties Inferred from the First and Second Observing Runs of Advanced LIGO and Advanced Virgo”. In: *Astrophys. J. Lett.* *882, L24 (2019)* (Nov. 2018). arXiv: [1811.12940](#) [astro-ph.HE].
- [LSC18l] LSC. “GWTC-1: A Gravitational-Wave Transient Catalog of Compact Binary Mergers Observed by LIGO and Virgo during the First and Second Observing Runs”. In: *Phys. Rev. X* *9, 031040 (2019)* (Nov. 2018). arXiv: [1811.12907](#) [astro-ph.HE].
- [LSC18m] LSC. “Searches for Continuous Gravitational Waves from Fifteen Supernova Remnants and Fomalhaut b with Advanced LIGO”. In: *Astrophysical Journal* *875, 122 (2019)* (Dec. 2018). arXiv: [1812.11656](#) [astro-ph.HE].
- [LSC19a] LSC. “First measurement of the Hubble constant from a dark standard siren using the Dark Energy Survey galaxies and the LIGO/Virgo binary-black-hole merger GW170814”. In: *The Astrophysical Journal Letters, Volume 876, 1, L7 (2019)* (Jan. 2019). arXiv: [1901.01540](#) [astro-ph.CO].

- [LSC19b] LSC. “Low-Latency Gravitational Wave Alerts for Multi-Messenger Astronomy During the Second Advanced LIGO and Virgo Observing Run”. In: (Jan. 2019). arXiv: [1901.03310](#) [astro-ph.HE].
- [LSC19c] LSC. “Search for transient gravitational wave signals associated with magnetar bursts during Advanced LIGO’s second observing run”. In: (Feb. 2019). arXiv: [1902.01557](#) [astro-ph.HE].
- [LSC19d] LSC. “Searches for Gravitational Waves from Known Pulsars at Two Harmonics in 2015-2017 LIGO Data”. In: *The Astrophysical Journal* *879* (2019) *10* (Feb. 2019). arXiv: [1902.08507](#) [astro-ph.HE].
- [LSC19e] LSC. “Narrow-band search for gravitational waves from known pulsars using the second LIGO observing run”. In: *Phys. Rev. D* *99*, *122002* (2019) (Feb. 2019). eprint: [1902.08442](#) (gr-qc).
- [LSC19f] LSC. “All-sky search for continuous gravitational waves from isolated neutron stars using Advanced LIGO O2 data”. In: *Phys. Rev. D* *100*, *024004* (2019) (Mar. 2019). arXiv: [1903.01901](#) [astro-ph.HE].
- [LSC19g] LSC. “Search for the isotropic stochastic background using data from Advanced LIGO’s second observing run”. In: *Phys. Rev. D* *100*, *061101* (2019) (Mar. 2019). eprint: [1903.02886](#) (gr-qc).
- [LSC19h] LSC. “Tests of General Relativity with the Binary Black Hole Signals from the LIGO-Virgo Catalog GWTC-1”. In: *Phys. Rev. D* *100*, *104036* (2019) (Mar. 2019). eprint: [1903.04467](#) (gr-qc).
- [LSC19i] LSC. “Directional limits on persistent gravitational waves using data from Advanced LIGO’s first two observing runs”. In: *Phys. Rev. D* *100*, *062001* (2019) (Mar. 2019). arXiv: [1903.08844](#) [gr-qc].
- [LSC19j] LSC. “All-sky search for long-duration gravitational-wave transients in the second Advanced LIGO observing run”. In: *Phys. Rev. D* *99*, *104033* (2019) (Mar. 2019). arXiv: [1903.12015](#) [gr-qc].
- [LSC19k] LSC. “Search for sub-solar mass ultracompact binaries in Advanced LIGO’s second observing run”. In: *Phys. Rev. Lett.* *123*, *161102* (2019) (Apr. 2019). arXiv: [1904.08976](#) [astro-ph.CO].

- [LSC19l] LSC. “All-sky search for short gravitational-wave bursts in the second Advanced LIGO and Advanced Virgo run”. In: *Phys. Rev. D* 100, 024017 (2019) (May 2019). arXiv: **1905.03457 [gr-qc]**.
- [LSC19m] LSC. “Search for intermediate mass black hole binaries in the first and second observing runs of the Advanced LIGO and Virgo network”. In: *Phys. Rev. D* 100, 064064 (2019) (June 2019). arXiv: **1906.08000 [gr-qc]**.
- [LSC19n] LSC. “Search for gravitational waves from Scorpius X-1 in the second Advanced LIGO observing run with an improved hidden Markov model”. In: *Phys. Rev. D* 100, 122002 (2019) (June 2019). arXiv: **1906.12040 [gr-qc]**.
- [LSC19o] LSC. “Search for gravitational-wave signals associated with gamma-ray bursts during the second observing run of Advanced LIGO and Advanced Virgo”. In: *Astrophys. J.* 886, 75 (2019) (July 2019). arXiv: **1907.01443 [astro-ph.HE]**.
- [LSC19p] LSC. “Search for Eccentric Binary Black Hole Mergers with Advanced LIGO and Advanced Virgo during their First and Second Observing Runs”. In: (July 2019). arXiv: **1907.09384 [astro-ph.HE]**.
- [LSC19q] LSC. “Model comparison from LIGO-Virgo data on GW170817’s binary components and consequences for the merger remnant”. In: *Classical and Quantum Gravity*, Vol. 37, No 4, p 045006 (2020) (Aug. 2019). arXiv: **1908.01012 [gr-qc]**.
- [LSC19r] LSC. “An Optically Targeted Search for Gravitational Waves emitted by Core-Collapse Supernovae during the First and Second Observing Runs of Advanced LIGO and Advanced Virgo”. In: *Phys. Rev. D* 101, 084002 (2020) (Aug. 2019). arXiv: **1908.03584 [astro-ph.HE]**.
- [LSC19s] LSC. “A gravitational-wave measurement of the Hubble constant following the second observing run of Advanced LIGO and Virgo”. In: *Astrophys J* 909 Number 2 218 (2021) (Aug. 2019). arXiv: **1908.06060 [astro-ph.CO]**.

- [LSC19t] LSC. “A guide to LIGO-Virgo detector noise and extraction of transient gravitational-wave signals”. In: *B P Abbott et al 2020 Class. Quantum Grav.* *37 055002* (Aug. 2019). arXiv: **1908.11170** [gr-qc].
- [LSC19u] LSC. “Open data from the first and second observing runs of Advanced LIGO and Advanced Virgo”. In: *SoftwareX* *13 (2021) 100658* (Dec. 2019). arXiv: **1912.11716** [gr-qc].
- [LSC20a] LSC. “A Joint Fermi-GBM and LIGO/Virgo Analysis of Compact Binary Mergers From the First and Second Gravitational-wave Observing Runs”. In: *The Astrophysical Journal*, *893:100 (14pp)*, *2020 April 20* (Jan. 2020). arXiv: **2001.00923** [astro-ph.HE].
- [LSC20b] LSC. “GW190425: Observation of a Compact Binary Coalescence with Total Mass  $\sim 3.4M_{\odot}$ ”. In: *Astrophysical Journal Letters* *892 (2020) L3* (Jan. 2020). arXiv: **2001.01761** [astro-ph.HE].
- [LSC19v] LSC. “GWTC-1: a gravitational-wave transient catalog of compact binary mergers observed by LIGO and Virgo during the first and second observing runs”. In: *Physical Review X* *9.3* (2019), p. 031040.
- [LSC20c] LSC. “GW190412: Observation of a Binary-Black-Hole Coalescence with Asymmetric Masses”. In: *Phys. Rev. D* *102, 043015 (2020)* (Apr. 2020). arXiv: **2004.08342** [astro-ph.HE].
- [LSC20d] LSC. “GW190814: Gravitational Waves from the Coalescence of a  $23 M_{\odot}$  Black Hole with a  $2.6 M_{\odot}$  Compact Object”. In: (June 2020). arXiv: **2006.12611** [astro-ph.HE].
- [LSC20e] LSC. “Gravitational-wave constraints on the equatorial ellipticity of millisecond pulsars”. In: *2020 ApJL* *902 L21* (July 2020). arXiv: **2007.14251** [astro-ph.HE].
- [LSC20f] LSC. “Properties and astrophysical implications of the 150 Msun binary black hole merger GW190521”. In: *Astrophys. J. Lett.* *900, L13 (2020)* (Sept. 2020). arXiv: **2009.01190** [astro-ph.HE].
- [LSC20g] LSC. “GW190521: A Binary Black Hole Merger with a Total Mass of  $150 M_{\odot}$ ”. In: *Phys. Rev. Lett.* *125, 101102 (2020)* (Sept. 2020). eprint: **2009.01075** (gr-qc).

- [LSC20h] LSC. “Search for Gravitational Waves Associated with Gamma-Ray Bursts Detected by Fermi and Swift During the LIGO-Virgo Run O3a”. In: *Astrophys. J.* 915, 86 (2021) (Oct. 2020). arXiv: 2010.14550 [astro-ph.HE].
- [LSC20i] LSC. “Population Properties of Compact Objects from the Second LIGO-Virgo Gravitational-Wave Transient Catalog”. In: (Oct. 2020). arXiv: 2010.14533 [astro-ph.HE].
- [LSC20j] LSC. “Tests of General Relativity with Binary Black Holes from the second LIGO-Virgo Gravitational-Wave Transient Catalog”. In: *Phys. Rev. D* 103, 122002 (2021) (Oct. 2020). eprint: 2010.14529 (gr-qc).
- [LSC20k] LSC. “GWTC-2: Compact Binary Coalescences Observed by LIGO and Virgo During the First Half of the Third Observing Run”. In: *Phys. Rev. X* 11, 021053 (2021) (Oct. 2020). arXiv: 2010.14527 [gr-qc].
- [LSC20l] LSC. “All-sky search in early O3 LIGO data for continuous gravitational-wave signals from unknown neutron stars in binary systems”. In: *Phys. Rev. D* 103, 064017 (2021) (Dec. 2020). arXiv: 2012.12128 [gr-qc].
- [LSC20m] LSC. “Diving below the spin-down limit: Constraints on gravitational waves from the energetic young pulsar PSR J0537-6910”. In: (Dec. 2020). arXiv: 2012.12926 [astro-ph.HE].
- [LSC21a] LSC. “Upper Limits on the Isotropic Gravitational-Wave Background from Advanced LIGO’s and Advanced Virgo’s Third Observing Run”. In: *Phys. Rev. D* 104, 022004 (2021) (Jan. 2021). arXiv: 2101.12130 [gr-qc].
- [LSC21b] LSC. “Constraints on cosmic strings using data from the third Advanced LIGO-Virgo observing run”. In: *Phys. Rev. Lett.* 126, 241102 (2021) (Jan. 2021). arXiv: 2101.12248 [gr-qc].
- [LSC21c] LSC. “Search for anisotropic gravitational-wave backgrounds using data from Advanced LIGO and Advanced Virgo’s first three observing runs”. In: *Phys. Rev. D* 104, 022005 (2021) (Mar. 2021). arXiv: 2103.08520 [gr-qc].

- [LSC21d] LSC. “Constraints from LIGO O3 data on gravitational-wave emission due to r-modes in the glitching pulsar PSR J0537-6910”. In: *ApJ* *922* *71* (2021) (Apr. 2021). arXiv: 2104.14417 [astro-ph.HE].
- [LSC21e] LSC. “Search for lensing signatures in the gravitational-wave observations from the first half of LIGO-Virgo’s third observing run”. In: (May 2021). arXiv: 2105.06384 [gr-qc].
- [LSC21f] LSC. “Searches for continuous gravitational waves from young supernova remnants in the early third observing run of Advanced LIGO and Virgo”. In: (May 2021). arXiv: 2105.11641 [astro-ph.HE].
- [LSC21g] LSC. “Constraints on dark photon dark matter using data from LIGO’s and Virgo’s third observing run”. In: *Phys. Rev. D* *105*, 063030, 2022 (May 2021). arXiv: 2105.13085 [astro-ph.CO].
- [LSC21h] LSC. “Search for intermediate mass black hole binaries in the third observing run of Advanced LIGO and Advanced Virgo”. In: *A & A* *659*, A84 (2022) (May 2021). arXiv: 2105.15120 [astro-ph.HE].
- [LSC21i] LSC. “Observation of gravitational waves from two neutron star-black hole coalescences”. In: *ApJL*, *915*, L5 (2021) (June 2021). arXiv: 2106.15163 [astro-ph.HE].
- [LSC21j] LSC. “All-sky Search for Continuous Gravitational Waves from Isolated Neutron Stars in the Early O3 LIGO Data”. In: *Phys. Rev. D* *104*, 082004 (2021) (July 2021). arXiv: 2107.00600 [gr-qc].
- [LSC21k] LSC. “All-sky search for short gravitational-wave bursts in the third Advanced LIGO and Advanced Virgo run”. In: (July 2021). arXiv: 2107.03701 [gr-qc].
- [LSC21l] LSC. “All-sky search for long-duration gravitational-wave bursts in the third Advanced LIGO and Advanced Virgo run”. In: (July 2021). arXiv: 2107.13796 [gr-qc].
- [LSC21m] LSC. “GWTC-2.1: Deep Extended Catalog of Compact Binary Coalescences Observed by LIGO and Virgo During the First Half of the Third Observing Run”. In: (Aug. 2021). eprint: 2108.01045 (gr-qc).

- [LSC21n] LSC. “Search for continuous gravitational waves from 20 accreting millisecond X-ray pulsars in O3 LIGO data”. In: *Phys. Rev. D* **105**, 022002 (2022) (Sept. 2021). arXiv: **2109.09255** [astro-ph.HE].
- [LSC21o] LSC. “Search for subsolar-mass binaries in the first half of Advanced LIGO and Virgo’s third observing run”. In: (Sept. 2021). arXiv: **2109.12197** [astro-ph.CO].
- [LSC21p] LSC. “All-sky, all-frequency directional search for persistent gravitational waves from Advanced LIGO’s and Advanced Virgo’s first three observing runs”. In: (Oct. 2021). arXiv: **2110.09834** [gr-qc].
- [LSC21q] LSC. “The population of merging compact binaries inferred using gravitational waves through GWTC-3”. In: (Nov. 2021). arXiv: **2111.03634** [astro-ph.HE].
- [LSC21r] LSC. “Search for Gravitational Waves Associated with Gamma-Ray Bursts Detected by Fermi and Swift During the LIGO-Virgo Run O3b”. In: (Nov. 2021). arXiv: **2111.03608** [astro-ph.HE].
- [LSC21s] LSC. “GWTC-3: Compact Binary Coalescences Observed by LIGO and Virgo During the Second Part of the Third Observing Run”. In: (Nov. 2021). arXiv: **2111.03606** [gr-qc].
- [LSC21t] LSC. “Constraints on the cosmic expansion history from GWTC-3”. In: (Nov. 2021). arXiv: **2111.03604** [astro-ph.CO].
- [LSC21u] LSC. “Searches for Gravitational Waves from Known Pulsars at Two Harmonics in the Second and Third LIGO-Virgo Observing Runs”. In: (Nov. 2021). arXiv: **2111.13106** [astro-ph.HE].
- [LSC21v] LSC. “All-sky search for gravitational wave emission from scalar boson clouds around spinning black holes in LIGO O3 data”. In: (Nov. 2021). arXiv: **2111.15507** [astro-ph.HE].
- [LSC21w] LSC. “Search of the Early O3 LIGO Data for Continuous Gravitational Waves from the Cassiopeia A and Vela Jr. Supernova Remnants”. In: (Nov. 2021). arXiv: **2111.15116** [gr-qc].
- [LSC21x] LSC. “Tests of General Relativity with GWTC-3”. In: (Dec. 2021). arXiv: **2112.06861** [gr-qc].

## COLLABORATION PUBLICATIONS

- [LSC21y] LSC. “Narrowband searches for continuous and long-duration transient gravitational waves from known pulsars in the LIGO-Virgo third observing run”. In: (Dec. 2021). arXiv: **2112.10990** [gr-qc].
- [LSC22a] LSC. “All-sky search for continuous gravitational waves from isolated neutron stars using Advanced LIGO and Advanced Virgo O3 data”. In: (Jan. 2022). arXiv: **2201.00697** [gr-qc].
- [LSC22b] LSC. “Search for gravitational waves from Scorpius X-1 with a hidden Markov model in O3 LIGO data”. In: (Jan. 2022). arXiv: **2201.10104** [gr-qc].
- [LSC22c] LSC. “First joint observation by the underground gravitational-wave detector, KAGRA, with GEO600”. In: (Mar. 2022). eprint: **2203.01270** (gr-qc).
- [LSC22d] LSC. “Search for Gravitational Waves Associated with Fast Radio Bursts Detected by CHIME/FRB During the LIGO–Virgo Observing Run O3a”. In: (Mar. 2022). arXiv: **2203.12038** [astro-ph.HE].
- [LSC22e] LSC. “Search for continuous gravitational wave emission from the Milky Way center in O3 LIGO–Virgo data”. In: (Apr. 2022). arXiv: **2204.04523** [astro-ph.HE].

## Acknowledgments

After five and a half years of working on a variety of different and interesting tasks, it is time to watch back and say thank you.

First of all, to Prof. Karsten Danzmann for the opportunity to work and graduate as a PhD student from the AEI in Hannover. The AEI was and is a great place, providing a perfect learning and research environment.

I would also like to thank Dr. Harald Lück and Prof. Kenneth Strain, the leaders of the AEI 10 m prototype group, for helping out with discussions and ideas in times of need.

I further like to thank the 10 m prototype group. Foremost, the postdocs David Wu and Sean Leavey, providing advice, help, and a working experimental environment. Also, the present and former PhD students Johannes Lehmann, Robin Kirchhoff, Janis Wöhler, Matteo Carlassara and Juliane von Wrangel for the friendly discussions and wonderful working atmosphere.

Many thanks to Prof. Joshua Smith for the discussions and hospitality during my visit to California and for being my third examiner.

I like to thank my parents for always supporting me in my choices and helping me to become who I am today.

Finally, I like to thank my wife, Ronja, for being a part of my life.

---

# CURRICULUM VITAE

---

## Personal Data

---

Name: Philip Koch  
Address: Wöhlerstr. 35  
30163 Hannover  
Place of birth: Hannover  
Date of birth: 31.12.1991

## Extra Curricular Activities

---

2016 Seminar *Structural mechanics simulation with ANSYS Mechanical*  
2018 Seminar *Scientific Writing*  
2018 Seminar *Public Writing*  
2019 Seminar *Oral Presentation Skills*  
2019 Seminar *Python Tutorial*

## Collaborations

---

2015 - present Member of *Ligo Scientific Collaboration (LSC)*  
12/2016 Research stay at IGR Glasgow *Institute for Gravitational Research*  
04/2019 Research stay at Caltech *California Institute of Technology*  
2019 - present Member of *QuantumFrontiers*

## Education and Academic Career

---

2011 Abitur at *Carl-Friedrich-Gauß-Schule Hemmingen*  
2011 - 2014 Bachelor at *Albert-Einstein-Institute for gravitational Physics Hannover*  
2014 - 2016 Master at *Albert-Einstein-Institute for gravitational Physics Hannover*  
2016 - 2022 PhD at *Albert-Einstein-Institute for gravitational Physics Hannover*